

**République Algérienne Démocratique et Populaire**  
**Ministère de l'Enseignement Supérieur et de la Recherche Scientifique**  
**Université de Batna**  
**Faculté des Sciences de l'Ingénieur**  
**Département d'Electronique**

**Thèse**  
**Contextual Enhancement**  
**Of Satellite Images**

En vue de l'obtention du diplôme de  
**Docteur d'état en électronique**  
Option: contrôle et traitement de signal

Par  
**SOUAD BENABDELKADER**

**Jury**

Président	N. Bouguechal	Professeur (Université de Batna)
Rapporteur	M. Boulemden	Professeur (Université de Batna)
Examineur	D. Benatia	Professeur (Université de Batna)
Examineur	M. Benyoucef	Maître de conférence (Université de Batna)
Examineur	F. Hachouf	Maître de conférence (Université de Constantine)
Examineur	S. Chikhi	Maître de conférence (Université de Constantine)

Année 2008



## *Acknowledgments*

*It has been a long time since the last acknowledgments.*

I would like to take this opportunity to express my thanks to Professor Mohammed Boulemden for his patience and encouragement that have been a true strength to complete this study.

I would like to thank Professor Nouredine Bouguechal from the Electronics Department at the University of Batna to preside at my maintaining thesis. Thank you very much to all the examining board members for their interest in my work namely, Dr. Fella Hachouf from the Electronics Department at the University of Constantine, Dr. Salim Chikhi from the Department of Computer Science of the University at Constantine, Prof. Djamel Benatia and Dr. Moussa Benyoucef from the Electronics Department at the University of Batna. I am deeply grateful for helping me to be finally in time before the dead line of December 31th.

I am very grateful to Dr. Farid Melgani with whom the essential of this work has been achieved. I would like to thank him for introducing me to the image restoration field and his constant supervision during the year I spent at the Dipartimento di Informatica at the University of Trento in Italy.

Thank you very much to my friends Lemia, and Samira for their constant support.

I am also very grateful for the assistance given to me by my friends and colleagues Dr. Djamel Benatia, Dr. Ramdane Mahammdi and Dr. Tarek Fortaki.

## *Dedications*

**W**ednesday, December 18, 2008, was the day of my doctorate thesis discussion. My parents could not be *physically* present because my father was ill with bronchitis since two weeks.

**A**t that day, I left early with the precious prayers of my mother and my youngest sister *Roukia*. I could not see my father before leaving. He was in pain and I did not want to worry him.

**W**hen coming home in the afternoon, my father was up out of bed for the first time since several days. He looked tired but so glad. We celebrated the event in family and took photos, the last we had with my father alive.

**T**hree weeks after, exactly in Tuesday, January 6, 2009, my father died. Now that I think of it, I thank *ALLAH* day and night to have allowed me finishing this thesis before my father departs this life for ever.

**T**his thesis is dedicated to the memory of my father, *Si Larbi El-Khroubi*. An adherent of the revolutionary agitation since his childhood. A great *Hero* of November, 1<sup>st</sup>, 1954. A man who had a partiality for his religion and nation; he went in Palestine in 1948, but the British army caught him with his four companions at the frontier between Libya and Egypt. The French authorities put them in prison for three months. A man who lived and died with honor and honesty. A model citizen. A model of all virtues. A father who taught us the love of Islam, family and country. A father who taught us how to read a newspaper at seven. A friend of his daughters. A Great Father, The Best.

**T**his thesis is dedicated to my mother with all my love and respect. She corrected my compositions in the primary school, stood awake with me in the secondary school and university, and was longing for me to get the doctorate degree.

**T**his thesis is dedicated to my sisters for their love and support.

# Abstract

**I**mages are the main sources of information in many applications. However, the images obtained from various imaging systems are subject to degradations and loss of information.

In the field of remote sensing, cloud obscuration presents a major impediment to the effective use of passive remotely sensed imagery. Cloud occurrence distorts or completely obscures the spectral response of land covers, which contributes to difficulties in understanding scene content. Therefore, a cloud removal task is needed as the primary important step to recover the missing measurements. Recently, cloud removal has been addressed as an image reconstruction/restoration issue, in which it is aimed at recovering an original scene from degraded or missing observation.

As a first application for remote sensing, we propose three general methods for post-restoration of cloud contaminated areas in multispectral multitemporal remote sensing images. Spatial, temporal and spectral information are incorporated in the post-restoration processes to analyze which is more suited to improve the restoration quality, depending on the contamination scenario. Experiments have shown that higher accuracies are obtained with the use of mutual spatio-spectral and temporal information.

Second, we address the problem of contrast enhancement for remote sensing application. At this purpose, two variational perspectives to bright preserving contrast enhancement scheme have been proposed. The methods can be viewed as refinements of histogram equalization, which use both local and global information to remap the image gray levels. The brightness preserving constraint is implicitly expressed with the use of a fuzzy 2-partition thresholding process to extract object regions from their background on the basis of the similarity of brightness of image objects.

The first method models the spatial relationships between neighboring pixels with a second order derivative metric which provides a local measure of spatial activity within the data. The second method uses a contextual spatial histogram to describe the gray level distribution in a predefined neighborhood system over a predefined area in the image.

Experiments have shown that the proposed methods increase the brightness preservation and yield a more natural enhancement. They are able to amplify edge contrast without explicitly detecting edge pixels.

# Résumé

L'être humain dépend à 99% de sa vision pour récolter des informations sur le monde qui l'entoure. Il est donc naturel que l'imagerie numérique ait pris une importance considérable. Néanmoins, historiquement parlant, les potentialités du traitement numérique des images pour le transfert et l'amélioration des images sont apparues avec le développement des grands ordinateurs et surtout avec les nécessités des programmes de recherche spatiale. Puis est venue l'ère de l'explosion des applications dans tous les domaines....

L'imagerie numérique est limitée par les dégradations, généralement désignées sous le terme de bruit d'image, dues aux bruits inhérents aux dispositifs d'acquisition (caméra, amplificateurs, quantification, ...). L'élimination du bruit et le recouvrement de l'information perdue ou cachée constituent donc une étape cruciale dans le traitement d'image.

D'un autre côté, les images acquises dans des conditions d'éclairage extrêmes; lumière trop faible ou trop puissante ainsi que les images issues de capteurs dont la dynamique est trop réduite sont peu contrastées, ce qui gêne sérieusement les opérations de reconnaissance, d'analyse et d'interprétation. Les méthodes de manipulation d'histogramme sont à l'origine des techniques d'amélioration du contraste, en particulier l'égalisation d'histogramme en raison de sa simplicité et des informations pertinentes à l'amélioration fournies par l'histogramme de l'image.

Il est important de noter que la restauration constitue une opération d'amélioration basée sur un modèle mathématique de la dégradation, alors que l'amélioration du contraste ne prend en considération aucun modèle de bruit, et est par conséquent laissée aux soins de l'observateur pour juger de la qualité de l'amélioration.

Le travail présenté dans cette thèse concerne à la fois restauration et amélioration du contraste appliquées au domaine de la télédétection satellitaire.

La thèse est composée de quatre chapitres.

Le premier chapitre introduit l'état de l'art des méthodes de restauration tout en présentant les critères quantitatifs standard de la qualité de restauration en plus d'un aperçu sur la littérature des méthodes de restauration.

Le deuxième chapitre aborde la restauration du point de vue d'une post-reconstruction de zones contaminées par les nuages dans une séquence d'images multispectrales multitemporelles. L'objectif visé dans ce chapitre est d'améliorer la qualité de restauration obtenue par deux méthodes générales de restauration développées récemment, en l'occurrence la technique dite Contextual Multiple Linear Prediction (CMLP) et celle appelée Contextual Nonlinear Prediction (CNP). Une post-reconstruction est alors effectuée en utilisant conjointement l'information spatiale, spectrale et temporelle. Trois méthodes en guise de solution ont été proposées, en l'occurrence la prédiction multimodale, la prédiction de l'erreur résiduelle issue d'un estimateur et enfin la post-reconstruction spatio-spectrale. La génération d'une Map d'erreur est utilisée comme critère d'évaluation supplémentaire de la qualité de restauration. Les résultats de la simulation ont été présentés à la fin du chapitre.

Le troisième chapitre présente les bases théoriques générales des techniques de modification d'histogramme. Les techniques de transformation ponctuelles sont considérées, en particulier l'égalisation et la spécification d'histogramme qui sont décrites en détail et par l'exemple pour la première. Trois critères de quantification de la qualité d'amélioration sont présentés et le chapitre s'achève par un aperçu sur la littérature concernant les méthodes d'égalisation d'histogramme.

Le quatrième chapitre concerne l'amélioration du contraste d'images de télédétection satellitaire en utilisant l'égalisation d'histogramme. Deux méthodes sont proposées, chacune se basant sur le seuillage d'une 2-partition floue pour satisfaire au critère de préservation de la luminosité des pixels. L'incorporation de l'information spatiale est exprimée dans la première méthode par le calcul des gradients du second ordre. Dans la deuxième méthode, le modèle spatial est exprimé par un histogramme bi-dimensionnel représentant la distribution spatiale conjointe des niveaux de gris dans un voisinage prédéterminé. Cet histogramme est calculée sur une zone prédéfinie de l'image et est utilisé par la suite pour le calcul de la densité de probabilité cumulative de l'image entière. Finalement, les résultats de la simulation sont présentés à la fin du chapitre.

# Contents

<b>INTRODUCTION</b>	<b>1</b>
<b>1. DIGITAL IMAGE RESTORATION</b>	<b>3</b>
1.1 INTRODUCTION	3
1.2 IMAGE DEGRADATION MODEL	4
1.3 MEASURE OF IMAGE RESTORATION QUALITY	5
1.3.1 Standard Metrics	5
1.3.2 Accuracy of the Measure	6
1.3.3 Precision of the Measure	6
1.3.4 Meaning of Measurement	6
1.4 LITERATURE SURVEY	7
1.4.1 Classical Image Restoration Techniques	7
1.4.2 New Image Restoration Techniques	10
1.5 SUMMARY	12
<b>2. CONTEXTUAL POST-RECONSTRUCTION OF CLOUD-CONTAMINATED IMAGES</b>	<b>13</b>
2.1 INTRODUCTION	13
2.2 CLOUD REMOVAL TECHNIQUES	14
2.3 Problem FORMULATION	17
2.4 PROPOSED SOLUTIONS	17
2.4.1 Spectral Information Source	18
2.4.2 SPATIAL Information Source	18
2.5 MULTIMODAL PREDICTOR	18
2.5.1 Spectral Information	18
2.5.2 Spatial Information	19
2.5.3 Prediction Function	19
2.6 RESIDUAL BASED PREDICTION	21

2.6.1	Sequential Residual-Based Prediction (SRBP)	21
2.6.2	PARALLEL Residual-Based Prediction (PRBP)	23
2.7	CONTEXTUAL SPATIO-SPECTRAL POST-RECONSTRUCTION	24
2.7.1	Description of the Method	24
2.7.2	Spectral Information	25
2.7.3	Spatial Information	25
2.7.4	Prediction Function	26
2.7.5	Error Map Generation	26
2.7.6	ALGORITHMIC Description	27
2.8	EXPERIMENTAL RESULTS	28
2.8.1	Data Set Description and Experiment Design	28
2.8.2	Previous Results	29
2.8.3	Multimodal Prediction Simulations	33
2.8.4	Residual-Based Prediction Simulations	37
2.8.5	CSSPR Simulations	43
2.9	Summary	49
<b>3.</b>	<b>HISTOGRAM MODIFICATION</b>	<b>50</b>
3.1	INTRODUCTION	50
3.2	HISTOGRAM MODIFICATION	51
3.2.1	Contrast of an Image	51
3.2.2	Image Transformation	51
3.2.3	Histogram Processing	51
3.3	QUALITY MEASURES	56
3.3.1	Absolute Mean Brightness Error	56
3.3.2	Contrast –Per-Pixel	55
3.3.3	Image Distortion	56
3.4	LITERATURE SURVEY	56
3.5	SUMMARY	58
<b>4.</b>	<b>CONTRAST ENHANCEMENT OF SATELLITE IMAGES BASED SPATIAL CONTEXT</b>	<b>59</b>
4.1	INTRODUCTION	59
4.2	CONTRAST ENHANCEMENT BASED THRESHOLDING	59
4.2.1	Brightness Preserving Bi-Histogram Equalization	60
4.2.2	Dualistic Sub-Image Histogram Equalization	62

4.2.3 Fuzzy 2-Partition Thresholding	62
4.2.4 Fuzzy 2-Partition Thresholding for Local Contrast Enhancement	68
4.3 CONTEXTUAL SPATIAL HISTOGRAM FOR CONTRAST ENHANCEMENT	70
4.3.1 Contextual Spatial Neighborhood	70
4.3.2 Contextual Spatial Histogram	70
4.3.3 Contextual Cumulative Density Function	70
4.3.4 Algorithm	71
4.4 EXPERIMENTAL RESULTS	71
4.4.1 Local Contrast Enhancement Based Thresholding Simulations	71
4.4.2 Contextual Spatial Histogram for Contrast Enhancement Results	72
4.5 SUMMARY	72
<b>CONCLUSION</b>	<b>88</b>
<b>Bibliography</b>	<b>90</b>

# List of Figures

Figure 2.1	Neighborhoods system	18
Figure 2.2	Block diagram of the SRBP system	22
Figure 2.3	Block diagram of the PRBP system	24
Figure 2.4	Block scheme of the whole contextual reconstruction process	25
Figure 2.5	Original sub-images in the Visible range used in the simulations	29
Figure 2.6	Original sub-images in the Infra-Red range used in the simulations	30
Figure 2.7	Masks adopted to simulate different cloud contaminations	30
Figure 2.8	CMLP reconstruction results	31
Figure 2.9	Linear multimodal prediction reconstruction results of channel 1	34
Figure 2.10	Linear multimodal prediction reconstruction results of channel 2	35
Figure 2.11	Linear multimodal prediction reconstruction results of channel 3	35
Figure 2.12	Nonlinear multimodal prediction reconstruction results of channel 1	36
Figure 2.13	Nonlinear multimodal prediction reconstruction results of channel 2	36
Figure 2.14	Nonlinear multimodal prediction reconstruction results of channel 3	37
Figure 2.15	Linear sequential residual-based prediction results of channel 1	40
Figure 2.16	Linear sequential residual-based prediction results of channel 2	40
Figure 2.17	Linear sequential residual-based prediction results of channel 3	41
Figure 2.18	Linear parallel residual-based prediction results of channel 1	41
Figure 2.19	Linear parallel residual-based prediction results of channel 2	42
Figure 2.20	Linear parallel residual-based prediction results of channel	42
Figure 2.21	Reconstruction results with the CSSPR method	45
Figure 2.22	Color composite result with the CSSPR method	46
Figure 2.23	Plotting graphs inside the contaminated area	47
Figure 2.24	Multichannel classification maps obtained by the K-means algorithm	48
Figure 2.25	Reconstruction $L_2$ -norm error maps	49
Figure 3.1	Examples of some point processing transformations	52
Figure 3.2	Histogram Shapes	53

Figure 3.3	Histogram equalization example	<b>54</b>
Figure 3.4	Illustration of some histogram equalization examples	<b>55</b>
Figure 4.1	Fuzzy membership function	<b>64</b>
Figure 4.2	Contextual spatial neighborhood system	<b>70</b>
Figure 4.3	Two level thresholding results of channel 1	<b>73</b>
Figure 4.4	Two level thresholding results of channel 2	<b>73</b>
Figure 4.5	Two level thresholding results of channel 3	<b>74</b>
Figure 4.6	Two level thresholding results of channel 4	<b>74</b>
Figure 4.7	Two level thresholding results of channel 5	<b>75</b>
Figure 4.8	Two level thresholding results of channel 7	<b>75</b>
Figure 4.9	Local contrast enhancement-based thresholding results of channel 1	<b>77</b>
Figure 4.10	Local contrast enhancement-based thresholding results of channel 2	<b>78</b>
Figure 4.11	Local contrast enhancement-based thresholding results of channel 3	<b>79</b>
Figure 4.12	Local contrast enhancement-based thresholding results of channel 4	<b>80</b>
Figure 4.13	Local contrast enhancement-based thresholding results of channel 5	<b>81</b>
Figure 4.14	Local contrast enhancement-based thresholding results of channel 7	<b>82</b>
Figure 4.15	Masks adopted to simulate different area locations	<b>82</b>
Figure 4.16	Contextual spatial contrast enhancement results of channel 1: Area C outside the mask	<b>84</b>
Figure 4.17	Contextual spatial contrast enhancement results of channel 4: Area C outside the mask	<b>85</b>
Figure 4.18	Contextual spatial contrast enhancement results of channel 1: Area C inside the mask	<b>86</b>
Figure 4.19	Contextual spatial contrast enhancement results of channel 1: Area C inside the mask	<b>87</b>

## List of Tables

Table 2.1	Quantitative results obtained by the linear multimodal prediction	<b>33</b>
Table 2.2	Quantitative results obtained by the non linear multimodal prediction	<b>34</b>
Table 2.3	Quantitative results obtained by the linear sequential residual predictor	<b>38</b>
Table 2.4	Quantitative results obtained by the non linear sequential residual predictor	<b>38</b>
Table 2.5	Quantitative results obtained by the linear parallel residual predictor	<b>39</b>
Table 2.6	Quantitative results obtained by the non linear parallel residual predictor	<b>39</b>
Table 2.7	Quantitative results obtained by the CSSPR method	<b>44</b>
Table 3.1	Histogram equalization procedure	<b>54</b>
Table 4.1	Quantitative results obtained by the local contrast enhancement based fuzzy 2-partition thresholding scheme	<b>76</b>
Table 4.2	Quantitative results obtained by the contrast enhancement based-contextual spatial histogram scheme: Area C outside the mask	<b>83</b>
Table 4.3	Quantitative results obtained by the contrast enhancement based-contextual spatial histogram scheme: Area C inside the mask	<b>83</b>

# INTRODUCTION

**T**he main part of the information received by a human is visual. Receiving and using visual information is referred to as sight perception or understanding. When a computer receives and uses visual information, we call this computer image processing and recognition. The modern advancement in this area is mainly due to the recent availability of image scanning and display hardware at a reasonable cost, the relatively free use of computers and the popularization of numerous computer processing techniques.

One of the major problems that have evolved in computer image processing was the *degradation* of the images in use. Images obtained from various imaging systems are subject to degradations and loss of information which could be devastating in many applications. The two main limitations in image accuracy are blur and noise. As a result, it was not long before the work on using computer techniques for retrieving meaningful information from degraded images began, what is today known as digital image restoration.

Images are captured in an excessively bright or dark environment in a number of different situations (e.g., pictures taken at night or against the sun rays). As a result, the images are low contrasted, i.e. too dark or too bright, and inappropriate for visual inspection and human interpretation and analysis. Improving the visual quality and enhancing the contrast of images constitutes one of the major issues in image processing. Histogram modification, and in particular histogram equalization is one of the basic and most useful operations in image processing. It has been recognized as the ancestor of plentiful contrast enhancement algorithms [1].

Contrast enhancement and restoration techniques are designed to improve the quality of an image as perceived by a human for a specific application. Image restoration is distinct from contrast enhancement techniques, which are designed to manipulate a degraded image in order to reveal subtle details and produce results more pleasing to an observer, without making use of any particular degradation models. Image restoration is applied to the restoration of a known distortion for which an objective criterion can be applied.

Remote sensing images typically contain an enormous amount of information. From the field of computer vision, enhancement procedures among other techniques determine one possibility to extract such information. The aim of the study at hand is to apply some developed algorithms as means for spatial information extraction.

The present thesis may be divided into two parts. The first deals with a contextual post-restoration technique of cloud-contaminated areas in multispectral multitemporal remote sensing images. Spatial, temporal and spectral information are incorporated in the post-restoration process to analyze which is more suited to improve the restoration quality. The second part concerns the contrast enhancement of remote sensing images using two independent channel processing methods. Based on the spatial context, the processes can be considered as local histogram equalization techniques.

The thesis is organized as follows. The first chapter provides a general and inevitably superficial review of digital image restoration techniques.

The second chapter deals with a contextual post-restoration of cloud-contaminated remote sensing images. The spatial and spectral information are effectively used to produce a better quality restored image. Numerical and visual results are presented and commented.

The third chapter introduces the histogram modification techniques. In particular, the histogram equalization technique is described and a rapid survey of different procedures is given.

The fourth chapter describes two different contrast enhancement techniques. Both of them are based on the fuzzy 2-partition two level thresholding for brightness preserving. In the first method, the spatial information is modeled to describe some spatial activity of the data in a predefined neighborhood, whilst in the second it is modeled with the use of a contextual spatial histogram. Numerical and visual results are presented and commented.

Finally, we conclude and present those areas which give rise to further improvements.

# Chapter 1

## DIGITAL IMAGE RESTORATION

### 1.1. INTRODUCTION

Images are the main sources of information in many applications. However, the images obtained from various imaging systems are subject to degradations and loss of information. The two main limitations in image accuracy are blur and noise. Hence, the extreme need for the ability to retrieve meaningful information from degraded images, what is today known as restoration of images, was and still is a valid challenge since the problem arises in almost every branch of engineering and applied physics.

Digital image restoration is being increasingly used in many applications. Just to name a few, restoration is encountered in astronomy, geophysics, biomedical imaging, computer graphics and enhancement, and defense-oriented applications. It has received some notoriety in the media, especially in the movies of the last two decades, and has been used in law enforcement and forensic science since several years. Another emerging application of this field concerns the restoration of aging and deteriorated films, and perhaps the most expanding area of application for digital image restoration is that in the field of image and video coding. Digital image restoration is being used in many other applications as well, the list is not exhaustive.

Image restoration is distinct from image enhancement techniques, which are designed to manipulate a degraded image in order to provide some interesting image features selectivity and produce results more pleasing to an observer, without making use of any particular degradation models. The problem of image reconstruction is a little more complicated since the true object is no longer a measure of light intensity over some scene, but a mapping of some physical property. The true object, therefore, must be reconstructed from data commonly called projections. Restoration and reconstruction techniques aim to the same

objective, however, which is that of recovering the original image and they end up solving the same mathematical problem which is that of finding a solution to a set of linear or non linear equations

Early techniques for digital image restoration were derived mostly from frequency-domain concepts. However, more modern algebraic approaches allow the derivation of numerous restoration methods that have been developed from different perspectives [1]-[3]. These algorithms have grown from denoising methods to spatially adaptive approaches and more recently neural networks and transform domain methods with the use of wavelets. Experiment results have shown that a single conventional restoration approach may not obtain satisfactory results. Therefore, hybrid methods have emerged.

## 1.2. IMAGE DEGRADATION MODEL

A two dimensional random field  $\mathbf{X} = \{x_{ij}\}$  on a lattice  $L = \{(i, j): 0 \leq i < N, 0 \leq j < M\}$  represents a true but non observable image, where  $x_{ij}$  measures the grey level/color intensity of the pixel at the  $(i, j)$ th location. The available data are  $\mathbf{Y}$ , a version of  $\mathbf{X}$  subject to various blurring phenomena as well as noise. Thus, image restoration techniques seek to recover an image from a blurred and noisy one. In digital image restoration, the standard linear observation model is expressed as:

$$\mathbf{Y} = \mathbf{H}\mathbf{X} + n \quad (1.1)$$

In this formulation,  $n$  represents an additive perturbation usually taken to be a zero mean Gaussian white noise.  $H$  is a point spread function (PSF) matrix of the imaging system. Sometimes however, the degradation involves a nonlinear transformation and a multiplicative noise. The problem of restoring  $x$  is then much more difficult. In model (1.1), matrix  $H$  and the statistical characteristics of the noise  $n$  are implicitly assumed to be known. But this assumption is not always fulfilled, and these quantities may also have to be estimated. Techniques used for image restoration require the modeling of the degradation; usually blur and noise and the image itself, then apply an inverse procedure to obtain an estimation of the original image.

Classical direct approaches to solving equation (1.1) have dealt with finding an estimate which minimizes the norm:

$$\|\mathbf{Y} - \mathbf{H}\hat{\mathbf{X}}\|^2 \quad (1.2)$$

leading to the least squares solution:

$$(\mathbf{H}^t \mathbf{H})\hat{\mathbf{X}} = \mathbf{H}^t \mathbf{Y} \quad (1.3)$$

This solution is usually unacceptable since  $H$  is most often ill conditioned. The critical issue that arises is that of noise amplification. This is due to the fact that the spectral properties of the noise are not taken into account. Indeed, it can be shown that the solution can be written in the discrete frequency domain as:

$$\hat{X}(l) = \frac{\hat{H}^*(l)\hat{Y}(l)}{|\hat{H}(l)|^2} \quad (1.4)$$

Where  $\hat{X}(l)$ ,  $\hat{H}(l)$ , and  $\hat{Y}(l)$  denote the DFT of the restored image,  $\hat{X}(i, j)$ , the PSF,  $h(i, j)$ , and the observed image,  $Y(i, j)$ , as a function of the 2-D discrete frequency index  $l$ , where  $l = (k_1, k_2)$  for  $k_1, k_2 = 0, \dots, N-1$ , for an  $N \times N$  point DFT, and  $*$  denotes complex conjugate. Clearly, for frequencies at which  $\hat{H}(l)$  becomes very small, division by it results in amplification of the noise. Assuming that the degradation is low pass, the small values of  $\hat{H}(l)$  are found at high frequencies, where the noise is dominant over the image. The noise component amplification exceeds any acceptable level.

In mathematical terms, image restoration is an ill-posed inverse problem. A problem is well-posed when its solution exists, is unique and depends continuously on the observed data. These are the so-called Hadamard conditions for a problem to be well posed [4]-[6]. Quite often in image restoration, no unique solution is available since many feasible solutions exist. In addition, image restoration is almost always ill-conditioned as shown above. It is interesting to note that the extent of the PSF has an effect on the severity of the ill-conditioning.

The ill conditioning is a direct consequence of the ill-posedness of the initial continuous data problem which is approximated by equation (1.1). In the restoration problem, the image is a convolution integral:

$$Y(s, s') = \iint_D h(s-r, s'-r') X(r, r') dr dr' \quad (1.5)$$

The kernel of this integral equation  $h$  is the 2-D impulse response or PSF of the imaging system. Since the data are erroneous or noisy, we cannot expect to solve this equation exactly and the true solution must be approximated in some sense.

The key idea is *regularization*. Obtaining the true solution from imperfect data is impossible. When regularizing the problem, it reduces to define a class of admissible solutions  $\{\hat{\mathbf{X}}\}$ :

$$\{\hat{\mathbf{X}}: \|\mathbf{Y} - H\mathbf{X}\| \leq \|b\|\} \quad (1.6)$$

among which an acceptable solution must be sought. The means is that to include some a priori information besides the information provided by the observed data.

### 1.3. MEASURE OF IMAGE RESTORATION QUALITY

#### 1.3.1. STANDARD METRICS

In most image restoration studies, the degradation modeled by blurring and additive noise is referred to in terms of a metric called the Signal-to-Noise Ration (SNR), defined as:

$$SNR = 10 \log_{10} \left[ \frac{\frac{1}{MN} \sum_{i,j} [X(i, j) - \bar{\mathbf{X}}]^2}{\sigma_n^2} \right] \quad (1.7)$$

for an  $M \times N$  image, where  $\mathbf{X}$  and  $\bar{\mathbf{X}}$  are the original image and its mean value respectively.

In applications of image restoration, image quality usually refers to the image's fidelity to its original. To measure the image restoration quality thus means to measure the amount of

improvement in image quality due to restoration. By far the most popular quantitative measures of image restoration quality are the Improvement in Signal-to-Noise Ratio (ISNR), the Mean Squared Error (MSE) and the Peak Signal-to-Noise Ratio (PSNR) metrics, which are defined as:

$$ISNR = 10 \cdot \log_{10} \left[ \frac{\sum_{i,j} [X(i,j) - Y(i,j)]^2}{\sum_{i,j} [X(i,j) - \hat{X}(i,j)]^2} \right] \quad (1.8)$$

$$MSE = \frac{1}{MN} \left[ \sum_{i,j} [X(i,j) - \hat{X}(i,j)]^2 \right] \quad (1.9)$$

$$PSNR = 10 \cdot \log_{10} \left[ \frac{MAX_p^2}{MSE} \right] \quad (1.10)$$

where  $X$ ,  $Y$  and  $\hat{X}$  are the original image, the degraded image and the restored image respectively.  $MAX_p$  is the maximum pixel value of the image. When the pixels are represented using 8 bits per sample, this is 255. More generally, when samples are represented using linear PCM with  $B$  bits per sample, maximum possible value of  $MAX_p$  is  $2^B - 1$ . Obviously, these metrics can only be used for simulation cases when the original image is available. While MSE, PSNR and ISNR do not always reflect the perceptual properties of the human visual system, they serve to provide an objective standard by which to compare different techniques. When the image restoration quality is measured with two different metrics, three important aspects are considered in a comparative evaluation of the two measures: accuracy, precision and meaning of the measurement.

### 1.3.2. ACCURACY OF THE MEASURE

An accurate measure of image restoration quality should closely mirror the subjective judgment made by human observers. However, there exists no clear definition of image quality and an 'absolutely' accurate measure of image quality is still not yet available in the field.

### 1.3.3. PRECISION OF THE MEASURE

Precision is an expression of relative smallness of variability within the measuring process. Suppose a set of similar distorted images of same type of blur and with same amount of noise images were restored by the same restoration operator. A high precision measure of image restoration quality, when applied to these restored images, should produce a set of measurements of small spread. The smaller the spread of the measurements, the more precise will be the measure.

### 1.3.4. MEANING OF MEASUREMENT

In (1.8), for example, the SNR improvement (ISNR) is defined as the difference between SNRs of the images before and after restoration. A positive SNR improvement indicates that the quality of distorted image is improved, while a negative one indicates deterioration. The zero value of the SNR improvement indicates there is neither improvement nor deterioration. However, when two different restoration methods are compared with each other by means of the SNR improvement, it only reveals which method is better.

## 1.4. LITERATURE SURVEY

### 1.4.1. CLASSICAL IMAGE RESTORATION TECHNIQUES

#### 1.4.1.1. Direct Regularized restoration Approaches

Numerous methods have been proposed for solving and regularizing equation (1.1). When considering the *direct restoration approaches*, one can use either a *stochastic* or a *deterministic* model for the original image,  $\mathbf{X}$ . In both cases, the model represents prior information about the solution which can be used to make the problem well-posed.

The *stochastic* regularization is based upon statistical considerations of the images and noise as stochastic or random processes. If the only random process involved is the additive noise,  $n$ , then solving for the minimum mean squared estimate of  $\mathbf{X}$

$$\min E \left\{ \left\| \mathbf{X} - \hat{\mathbf{X}} \right\|^2 \right\} \quad (1.11)$$

will be called the *regression* problem. If the image  $\mathbf{X}$  is also considered as a random image, subject to knowledge of  $R_{xx} = E \{ \mathbf{X} \mathbf{X}^T \}$ , which is the covariance matrix of  $\mathbf{X}$ , and  $R_{nn} = E \{ n n^T \}$ , which is the covariance matrix of the noise, then the problem will be referred to a *Wiener* estimation [7]. In this case, the linear estimate which minimizes equation (1.11) is given by:

$$\hat{\mathbf{X}} = R_{xx} H^T (H R_{xx} H^T + R_{nn})^{-1} \mathbf{Y} \quad (1.12)$$

By assuming block circulant structures for each of the matrices in (1.12), it can be rewritten and solved in the discrete frequency domain leading to the Fourier implementation of the Wiener filter. There are several methods that may be used to estimate the statistics required for implementing the Wiener filter. They can be separated into parametric and nonparametric approaches. Examples of techniques which fit into this framework can be found in [8]-[13].

The regression and Wiener estimation models are excellent restoration solutions for stationary random processes imaging situations. For imaging situations for which these assumptions are not appropriate, a variety of more advanced stochastic restoration solutions are available that are based upon estimation and decision theory concepts.

The *deterministic* regularization methods seek an estimate of  $\mathbf{X}$  that minimizes a predefined criterion of performance. Because of their simplicity, the least squares criterion functions have been often used leading to several well-known restoration methods. These methods are the result of considering either an unconstrained or a constrained approach to the least squares restoration problem.

The least squares solution is the minimizer of the total energy of residual error between the actual observed data  $y$  and the observed response, using the approximate solution  $\hat{\mathbf{X}}$  in the absence of any knowledge about noise. In other words, we want to find an  $\hat{\mathbf{X}}$  such that:

$$\|n\|^2 = \left\| \mathbf{Y} - H \hat{\mathbf{X}} \right\|^2 \quad (1.13)$$

Aside of the requirement that it minimizes equation (9),  $\hat{\mathbf{X}}$  is not constrained in any other way. The least squares solution is given by:

$$\hat{\mathbf{X}} = H^{-1} \mathbf{Y} \quad (1.14)$$

In general, this solution, although unbiased, is rejected since the true image is expected to be significantly smoother. Thus, some infidelity to the data must be introduced in order to obtain a smoother solution. Constrained least squares (CLS) restoration can be formulated by choosing an  $\hat{x}$  to minimize the Lagrangian

$$\min \left[ \| \mathbf{Y} - \mathbf{H}\hat{\mathbf{X}} \|^2 + \alpha \| \mathbf{C}\hat{\mathbf{X}} \|^2 \right] \quad (1.15)$$

where the term  $\mathbf{C}\hat{\mathbf{X}}$  generally represents a high pass filtered version of the image  $\hat{\mathbf{X}}$ . This is essentially a smoothness constraint. Use of  $\mathbf{C}$  operator provides an alternative way to reduce the effects of the small singular values of  $\mathbf{H}$ , occurring at high frequencies, while leaving the larger ones unchanged. This approach introduces considerable flexibility in the restoration process because it yields different solutions for different choices of  $\mathbf{C}$ . One typical choice of  $\mathbf{C}$  is the 2-D Laplacian operator described in [14].  $\alpha$  represents the Lagrange multiplier, commonly referred to as the regularization parameter, which controls the trade-off between fidelity to the data (as expressed by the term  $\| \mathbf{Y} - \mathbf{H}\hat{\mathbf{X}} \|^2$ ) and smoothness of the solution (as expressed by  $\| \mathbf{C}\hat{\mathbf{X}} \|^2$ ). The minimization in equation (1.15) leads to a solution of the form:

$$\hat{\mathbf{X}} = (\mathbf{H}^T \mathbf{H} + \alpha \mathbf{C}^T \mathbf{C})^{-1} \mathbf{H}^T \mathbf{Y} \quad (1.16)$$

This may also be solved directly in the discrete frequency domain when block-circulant assumptions are used. The critical issue in the application of equation (1.16) is the choice of  $\alpha$ . This problem has been investigated in a number of studies [15]. Several variants of the CLS restoration can be found, for example, in [16]-[22] and the references therein.

#### 1.4.1.2. Iterative Approaches

Iterative reconstruction algorithms have been widely used in computational imaging applications. They are advantageous in that:

- there is no need to explicitly implement the inverse of an operator;
- the process may be monitored as it progresses and additional regularization may be obtained by terminating the iteration before convergence;
- the effect of noise may be controlled with certain constraints;
- spatial adaptivity may be introduced;
- and the parameters determining the solution can be updated as the iteration proceeds.

The main disadvantage of iterative algorithms is their heavy computational burden. However, with the advance of high-performance computing technology, this is becoming a less serious hurdle.

There are many different iterative reconstruction algorithms. Among the first used are the *sequential block iterative* (SeqBI) algorithms that have been improved by the *simultaneous block iterative* (SimBI) algorithms ([23]-[31] and the references therein). All SimBI algorithms can be regarded as special cases of the general form, expressed in matrix-vector notations:

$$\mathbf{X}_{k+1} = \mathbf{X}_k + \beta_{k+1} \mathbf{P} \mathbf{H}^T \mathbf{Q} (\mathbf{Y} - \mathbf{H} \mathbf{X}_k) \quad (1.17)$$

where  $\mathbf{H}^T$  is the conjugate transpose of  $\mathbf{H}$ ,  $\mathbf{P}$  and  $\mathbf{Q}$  are positive definite matrices and  $\beta_{k+1}$  is a positive scalar called the relaxation coefficient or the step size. Oftentimes  $\beta_{k+1} = \beta$  is a constant, but it does not have to be.

More recently, one of the most basic of deterministic iterative techniques, that is widely used in various applications, considers solving

$$(H^T H + \alpha C^T C)X = H^T Y \quad (1.18)$$

with the method of successive approximations [32]. This leads to the following iteration for  $x$ :

$$\begin{aligned} X_0 &= \beta H^T Y \\ X_{k+1} &= X_k + \beta [H^T Y - (H^T H + \alpha C^T C)X_k] \end{aligned} \quad (1.19)$$

This iteration is often referred to as the iterative CLS or Tikhonov-Miller method (see for example [32]-[38] and the references therein), depending on the way the regularization parameter  $\alpha$  is computed. Obviously, if the matrices  $H$  and  $C$  are block circulant, the iteration in equation (1.19) can be implemented in the discrete frequency domain. The termination criterion most frequently used compares at each iteration the normalized changes in energy to a threshold such as:

$$\frac{\|X_{k+1} - X_k\|^2}{\|X_k\|^2} \leq 10^{-6} \quad (1.20)$$

The choice of the regularization parameter,  $\alpha$ , is still an issue with this approach, and it may be computed in a direct or iterative manner. There are other deterministic techniques which can be used to perform iterative restoration as well. For example, the deterministic approach described above can be generalized to form an iterative method called projections onto convex sets, or POCS, in which any number of prior constraints on a solution can be imposed as long as the constraint sets are closed convex [39]. POCS has been used very successfully in both deterministic and stochastic based image recovery techniques [40]-[44]. Other stochastic approaches also lead to iterative restoration techniques including in particular maximum likelihood solutions [45]-[49], various formulations of the Expectation-Maximization (EM) algorithm for image and blur identification and restoration [50]-[52] and the iterative Wiener filter [53]-[55].

### 1.4.1.3 Recursive Approaches

Recursive filtering operations usually require less memory for storage than the direct or iterative methods when reduced order models are used. The recursive equivalent of the Wiener filter is the discrete Kalman filter [56]-[58].

In the state space representation, the Kalman filter addresses the problem of estimating an image distorted by noise that is governed by the linear stochastic difference equation

$$\bar{X}(i, j) = \mathbf{A} \bar{X}(i, j - 1) + \bar{w}(i, j) \quad (1.21)$$

with a measurement that is

$$\bar{Y}(i, j) = H \bar{X}(i, j) + \bar{v}(i, j) \quad (1.22)$$

The random variables  $w$  and  $v$  represent the process and measurement noise (respectively). They are assumed to be independent (of each other), zero Gaussian processes with  $R_{ww} = E[\bar{w}\bar{w}^T]$  and  $R_{vv} = E[\bar{v}\bar{v}^T]$ .  $\mathbf{A}$  is the prediction matrix.

The Kalman filter estimates a process by using a form of feedback control: the filter estimates the process state at some time and then obtains feedback in the form of (noisy) measurements.

As such, the equations for the Kalman filter fall into two groups: *time update* equations (or predictor equations) and *measurement update* equations (or corrector equations). The time update equations are responsible for projecting forward (in time) the current state and error covariance estimates to obtain the *a priori* estimates for the next time step. The measurement update equations are responsible for the feedback, i.e. for incorporating a new measurement into the *a priori* estimate to obtain an improved *a posteriori* estimate. The prediction and update terms for the Kalman filter are simply:

*Prediction equations:*

$$\hat{X}^+(i, j) = \mathbf{A} \hat{X}(i, j-1) \quad (1.23)$$

$$P^+(i, j) = \mathbf{A} P(i, j-1) \mathbf{A}^T + R_{ww} \quad (1.24)$$

*Measurements update equations:*

$$\hat{X}(i, j) = \hat{X}^+(i, j) + K(i, j)[\bar{Y}(i, j) - H \hat{X}^+(i, j)] \quad (1.25)$$

$$P(i, j) = [\mathbf{I} - K(i, j) H] P^+(i, j) \quad (1.26)$$

$$K(i, j) = P^+(i, j) H^T [H P^+(i, j) H^T + R_{vv}]^{-1} \quad (1.27)$$

However, different models of Kalman filter have been developed as heuristic tools with different motivations [59]-[62]. Recall that there are other techniques which can be used to perform recursive restoration as well [63].

## 1.4.2. NEW IMAGE RESTORATION TECHNIQUES

The algorithms presented in the previous section represent the foundation of the approaches to the restoration problem today. They are successful approaches and they have been applied to many different image restoration problems. However, most of these algorithms deal with some global assumptions about the behavior of an image, which are at the origin of the two most prevalent restoration artifacts: ringing around the edges, and filtered noise causing false texturing in the flat regions of the image.

As we move into the different phases of research in this field, much progress has been made in the last two decades. Newer successful techniques which address the problem with the same assumptions as in the classical approaches include the use of robust functionals and total least squares. However, spatially adaptive or non-stationary approaches have also been developed to alleviate some of the problems associated with such rigid global restrictions.

### 1.4.2.1 Spatially Adaptive Approaches

Spatially adaptive algorithms frequently incorporate the properties of the human visual system [64]-[76]. Because the visual system is sensitive to sharp changes in an image, it is not desirable to smooth over the edges when performing restoration. Therefore, the application of a different restoration filter at each spatial location is desirable.

An iterative algorithm is generally employed in the case of spatially adaptive restoration, and the spatial adaptivity can be achieved with the use of weight matrices. These can be kept fixed, or be adapted at each iteration step based on the partially restored image.

Recursive methods can accommodate spatial adaptivity when using a stochastic model of the image, by changing the parameters of the model at the edges. The multiple model approach can also lead to a reduction in ringing artifacts around the edges in a restored image.

*Maximum a posteriori* (MAP) probability methods have also been investigated in great detail for non-stationary image restoration. These methods utilize space-variant density function as prior knowledge to capture the non-stationarity of the original image with Gibbs- Markov random field (MRF) models as powerful and robust descriptors of the spatial information. A rapid overview on the methods which fall under the Bayesian framework will be given in a subsection below.

#### **1.4.2.2. Color and Multichannel Image Restoration**

The problem of color image restoration presents a unique difficulty in that the multiple color channels are related. Thus, cross-channel correlations need to be exploited in order to achieve optimal restoration results. A number of approaches have been used to handle not only the color multichannel image restoration problem, but also other inherent multichannel problems such as image sequence restoration and multispectral remote sensing image restoration, see for example [77]-[91].

#### **1.4.2.3. Astronomical Image Restoration**

The first encounters with digital image restoration in the engineering community were in the area of astronomical imaging. Indeed, ground-based imaging systems were often subject to one or another of the two following forms of noise: a blurring due to the rapidly changing index of refraction of the atmosphere, and a motion blur resulting from slow camera shutter speeds relative to rapid spacecraft motion. Iterative approaches are found to be well-suited at restoring astronomical data, in particular entropy-based methods [92], modified Richardson-Lucy iterative approaches [93], [94], regularized iterative constrained least-squares techniques [95] and Bayesian approaches [96].

#### **1.4.2.4. Neural Networks and Restoration**

Neural networks may be used to realize well-known algorithms without the need for extensive underlying assumptions about the distribution of the parameters being estimated. They may also be used to estimate the regularization parameter in the CLS approach, and can be developed to alternate between learning and restoration cycles. In addition, neural processing techniques have led to efficient VLSI architectures for image restoration due to their highly parallel nature, see for example [97]-[101].

#### **1.4.2.5. Wavelets in Restoration**

Past adaptive restoration techniques have examined the problem in the spatial domain, using various local measures to describe the type of activity near a pixel. However, many regularized image restoration algorithms result in edge smoothness of the restored image. The use of wavelet based method greatly improves this condition.

The wavelet transform is a time-frequency representation which has good localization in both domains. The good performance of wavelet-based denoising is intimately related to the approximation capabilities of wavelets. The wavelet transforms of images tend to be sparse (i.e., many coefficients are close to zero) and the noise is uniformly spread throughout the coefficients, while most of the image information is concentrated in the few largest ones. This implies that image approximations based on a small subset of wavelets are typically very accurate. A number of researchers have investigated the restoration and recovery problems

from the subband/multiresolution perspective, see for example [102]-[112] and the references therein.

#### **1.4.2.6. Blur Identification**

Most classical techniques assume that the convolution operator representing the blur is known a priori. This, however, is almost never the case in practical imaging situations, thus, the area of blur identification, or blind deconvolution, is a very important subset of image restoration in which much important work has been performed.

Existing blind restoration methods can be categorized into two main classes: the first includes a large group of methods, which require estimating the PSF as a prerequisite stage to the image restoration process. In this approach, estimating the PSF and calculating the true image are disjoint procedures, such as zero sheet separation [113], generalized cross validation (GCV) [114], and maximum likelihood and expectation maximization (ML-EM) [115] based on the ARMA image model; the second incorporates the PSF identification procedure within the restoration algorithm, via simultaneously estimating the PSF and the original image, such as nonnegative and support constraints recursive inverse filtering (NAS-RIF) [116], maximum likelihood and conjugate gradient minimization (ML-CGM) [117], ML-EM [118], and simulated annealing (SA) [119]. There are also several other emerging techniques that have been used to address this identification problem, see for example [120]-[126] and the references therein.

### **1.5. SUMMARY**

In this rapid and inevitably superficial survey, we have mentioned many approaches for solving the restoration problem that have been proposed for different applications. In the same way, there are many other applications in today's world that make ready use of image restoration techniques. Some of the most interesting of these lie in the areas of medical imaging [127]-[129], motion restoration [130]-[132], image and video coding [133], [134], digital restoration of films [135], digital consumer products, optics, geophysics, defense oriented applications, printing applications that require the use of restoration to ensure halftone reproductions of continuous images to be of high quality, etc .

In spite of their apparent variety, image restoration methods have a common estimation structure. This can be summed up in a single word: *regularization*. In addition, most image restoration and estimation methods present some common practical limitations. The most sophisticated methods require the use of several tuning parameters (referred to as hyperparameters) which should be estimated from the data. Methods are available to perform this task. Some of them are reputed to give correct results, others not.

Though more complex than classical approaches, newer techniques, in particular spatially varying restoration methods such as those based on MRFs [136]-[228] and wavelets modeling, allow an improvement in the description of an image with the use of more complete models. Computational and methodological complexity has, thus, to be balanced against the quality of results, depending on the reliability for a given application.

# Chapter 2

## CONTEXTUAL POST-RECONSTRUCTION OF CLOUD-CONTAMINATED IMAGES

### 2.1. INTRODUCTION

Images acquired from passive sensors are often subject to cloud contamination whose extent varies depending on the season and the geographic area. For example, only 40% of the Brazilian Amazon basin has a good probability (>90%) of one image with less than 10% cloud contamination [229]. In some of the Canadian coastal regions there are areas where the probability of acquiring one satellite scene with less than 10% cloud cover during July and August is less than 20% [230]. In fact, approximately 50% of the earth's surface is obscured by clouds on any given day [231].

Cloud obscuration presents a major impediment to the effective use of passive remotely sensed imagery. Cloud occurrence distorts or completely obscures the spectral response of land covers, which contributes to difficulties in understanding scene content. Therefore, a cloud removal task is needed as the primary important step to recover the missing measurements.

The cloud removal process usually begins with the cloud detection procedure. In general, the objective of *detection* is simply identification of pixels within the image in which the cloud optical depth is greater than a specified threshold. This is, practically speaking, a necessary prerequisite for *characterization*, in which the basic cloud properties (optical depth, altitude, etc.) are retrieved.

Remote sensing image data typically contain an enormous amount of information. Image processing, in particular segmentation and boundary extraction, play a vital role in the extraction of spatial information associated to the content of these images. Accurate cloud detection in satellite scenes consists of discriminating between clouds and the land surface. It usually involves two basic steps: 1) segment the scene into natural groups (e.g., cloud versus land versus ocean); and 2) label each segment correctly. These two steps can be combined into a single step as is done in simple thresholding approaches [232]. In recent years, considerable research has been focused on this area resulting in the development of two major classes of cloud detection/ classification methods: spectral-based and textural-based algorithms.

The first class utilizes the information on the cloud radiances in different spectral bands. Some of the most commonly used methods in this category include threshold-based techniques and clustering approach. Most of the algorithms developed before made use of visible/near-infrared static spectral thresholds to detect cloud according to the characteristic of cloud with high reflectance and low temperature [233]. The accuracy of a static threshold, however, is affected by changes in atmospheric water vapor, aerosol type and concentration, and seasonal and inter-annual variations in surface reflectivity and emissivity which affect the albedo and brightness temperatures observed by the sensor. In fact, a static threshold which accurately screens a satellite scene at a given location often will fail for a different time of year at the same location [234]. Unlike the thresholding of non satellite images for which the thresholds are simply related to the pixels intensities [235]-[237], the thresholds of cloud detection are strongly related to time, region and sensor (sun elevation) [238]. Consequently, a more advantageous way has been developed for multispectral cloud detection and processing. Variants of this method combine several thresholds on different radiance channels [239] or threshold the differences between channel radiances [240].

The second category uses textural-based methods to classify the data based on the characteristics of spatial distribution of gray levels corresponding to a region/block within the image. Most of the textural-based cloud detection classification methods, in the past used statistical measures to characterize the textural features such as Gray-level Co-occurrence Matrix (GLCM), Gray-level Difference Matrix (GLDM), Gray-level Difference Vector (GLDV) and Sum And Difference Histogram (SADH) [241],[242]. Recently, new texture analysis schemes based on the Gabor Transform, Wavelet Transform and Neural Network have been developed which not only extract the salient features of the data efficiently but also reduce the dimensionality of the data to a manageable size [243].

## **2.2. CLOUD REMOVAL TECHNIQUES**

To enhance the difference between cloud and land surface, people adopt many methods to remove cloud. In the remote sensing field scarce attention has been paid to the specific problem of cloud removal [244].

Among the earliest attempts at removing cloud cover from the passive remotely sensed imagery, one can find the simple NASA compositing technique [245] which consists of selecting the optimal pixel (the most cloud-free pixel) with maximum NDVI (Normalized Difference Vegetation Index) among a set of data acquired at the same location over a limited time period. The main drawbacks of this technique are three: 1) it requires a high temporal resolution acquisition over a short time period; 2) it loses temporal resolution over the considered time period; and 3) it is not effective in persistent cloud cover areas. Recently, in developing a compositing methodology specifically designed for the humid tropics [246], the

blue band was used in place of the red band of the normal NDVI equation in [245]. The new NDBI (Normalized Difference Blue Index) technique provides compositing result with considerably less speckle, but slightly blurred.

In another compositing method [247], the pixel with maximum brightness temperature has been selected as the optimal pixel under the assumption that clouds tend to decrease the apparent surface temperature and higher surface temperature should be measured for pixels with lower atmospheric attenuation. The algorithm can lead to avoid clouds and cloud shadows.

In [248] the compositing method performs into two steps. First, among candidates, a pixel is retained if the corresponding NDVI is greater than a predetermined threshold, which indicates the variation that the NDVI depends upon sensor scan angles. Second, the pixel with minimum scan angle among retained pixels is selected as the optimal. The second condition shows a preference for pixels of near-nadir acquisition geometry with high spatial resolution. The threshold was established by trial and error and varies for areas variations.

In the algorithm of [249], the optimal pixel is selected to minimize a discriminant equation of composite. The algorithm was found to be limited to satellite zenith angle. Based on assessment of the algorithms in [245]-[249], a new hybrid algorithm was devised in [250]. Among 10 days time series AVHRR/HRPT data of four seasons, the optimal pixel was selected by the following steps:

- 1) Pixel  $k$  is retained among candidates if the difference between the maximum brightness temperature collected from channel 4 and the brightness temperature of pixel  $k$ , collected from channel 4, is less than 12 [centigrade units];
- 2) Pixels are retained among the retained pixels by step 1, if the corresponding NDVIs are greater than a predetermined threshold;
- 3) Finally pixel with minimum scan angle over the retained pixels by step 2 is selected as the optimal pixel. The method has proved to be superior to the four previous ones; however it is sensor dependant besides the limitation to the Asian region.

The SSM/I radiometer, like optical sensors, is sensitive to the presence of cloud cover and precipitation, which lower the observed brightness temperature and may confuse the measurements with some surface features like rivers or lakes. Several algorithms, like the second highest (SH) [251] and the modified maximum average (MMA) [252], have been developed to remove cloud effects from SSM/I images. Both algorithms aim at producing a composite cloud-free image from a sequence of SSM/I images acquired over a short time period. While the former is based on the idea of representing each image pixel by the second highest value in the considered vector of multitemporal measurements as an alternative to the mean or the median values, the latter removes cloud noise by averaging only part of the measurements contained in the vector. Selection of the MMA subset of measurements is carried out by considering all the measurements above the vector mean except the one with the highest value. In [159], authors show that an hybrid algorithm that implements MMA in the presence of clouds and averages the measurements in their absence, can significantly improve the quality of the composite image compared to the MMA and the SH algorithms. A further improvement of the algorithms has been achieved in [253], with the development of new alternative heuristics for cloud removal specifically for 85 GHz SSM/I data. Higher accuracy result can be obtained.

Unlike traditional interpolation methods, the authors in [254] tried to take full advantage of the spatial information in the image to perform a geostatistical interpolation for predicting

obscured pixel values by cloud cover. The method is limited by the spatial distribution and the optical depth of clouds.

In [255], a robust method termed Haze Optimized transformation (HOT) was developed for the detection and characterization of Haze/Cloud spatial distribution in Landsat scenes. The transformation quantifies the perpendicular displacement of a pixel from a clear line, which is derived from a spectral analysis of a visible band-space. The transformed image has good quality for diverse surface cover and atmospheric characteristics. However, thick clouds still obscure the scene.

In [256] a mathematically well founded method was proposed to remove the distortions caused by a particular kind of clouds from visible channels, namely cirrus clouds usually found above the 10-Km altitude. The authors base their method on the fact that the measurements acquired at the 1.38- $\mu\text{m}$  band are essentially due to cirrus reflectance attenuated by the absorption of water vapor contained in the uppermost layer of the atmosphere (above cirrus clouds), and develop a mathematical model for correcting those attenuation effects. They exploit this result to derive and then remove the true cirrus cloud reflectance from contaminated measurements in visible channels. This interesting method was assessed successfully on data acquired by two different hyperspectral sensors: the Moderate Resolution Imaging Spectroradiometer (MODIS) and the Airborne Visible Infrared Imaging Spectrometer (AVIRIS).sensors.

In [257], authors tried to improve the traditional homomorphism filtering method [258] for cloud removal. Instead of the filtering in the frequency field, the new algorithm isolates the low frequency component of the image representing the cloud information with calculating a neighbourhood average in the spatial field.

In [259], an ecosystem classification-dependent temporal interpolation technique is proposed for reconstructing surface reflectance for MODIS data. It is based on the computation of pixel-level and regional ecosystem-dependent phenological curves. Missing temporal data associated with a given pixel are reconstructed from the most appropriate curve among the available pixel-level and regional curves.

A new strategy for making nearly cloud-free image mosaics is that described in [260]. The cloud removal process is carried out in two steps. Firstly, the pixel value of a cloud/cloud shadow contaminated pixel in the reference scene is predicted from other scene dates using a regression tree model. Secondly, a correction based histogram matching to adjacent scenes is then applied to compensate for the apparition of the visible seam-lines. While effective, thick clouds still remain.

In [261], authors have addressed the problem of restoring the contrast of atmospherically degraded images and video. They presented a physics-based model [262] that describes the appearances of scenes in uniform bad weather conditions. In the considered model, changes in intensities of scene points under different weather conditions provide simple constraints to detect depth discontinuities in the scene and also to compute scene structure. Depending on the scenes structures, either depth segmentation method (regions within closed contours of depth edges) or scene structure method (scaled depths) may appear more valuable. This weather removal algorithm does not require any a priori scene structure, distribution of scene reflectance, or detailed knowledge about the particular weather condition. Both of the two methods are effective under a wide range of weather conditions including haze, mist, fog and conditions arising due to other aerosols. Although the entire analysis was presented for

monochrome images, however the methods can be applied to gray scale, RGB color, multispectral and IR images.

### 2.3. PROBLEM FORMULATION

In [244], two general methods for the reconstruction of cloud-contaminated areas in a sequence of multitemporal multispectral images acquired over the same geographical area have been introduced. The methods were based on the assumptions that spectral nonstationarity is allowed, while the spatial structure should be almost identical over the considered multitemporal multispectral sequence. Given a contaminated image of the sequence, each area of missing measurements (i.e., cloudy or shadowed area) can be recovered by means of a contextual prediction process that reproduces the local spectrotemporal relationships. These are deduced from the cloud-free areas in the spatial neighborhood of the contaminated region over the series of temporal images available. In the first method, called the contextual multiple linear prediction (CMLP), the contextual prediction is implemented by an ensemble of linear predictors, each trained in an unsupervised way over a local temporal region that is spectrally homogeneous in each temporal image of the sequence. In order to obtain such regions, each temporal image is locally classified in an unsupervised way by the expectation-maximization (EM) algorithm assuming that the data classes are Gaussian. In the second method, namely the contextual nonlinear prediction (CNP), the local spectrotemporal relationships are reproduced by a single nonlinear predictor based on the support vector machine approach (SVM) [263],[264].

Though these contextual reconstruction approaches allow to face some general issues raised by the methods proposed in the literature (such as sensor, ground-cover type, and cloud type dependences) and has proved promising, they still do not fully exploit all available information and thus leave room for further methodological improvement. The first improvement derives from the fact that the prediction systems do not use spatial information, whose integration in an image processing scheme can prove valuable as shown in other applications [265],[266]. The second is related to the problem that the CMLP and the CNP processes are carried out independently for each channel of the sequence without exploiting the inter-channel correlation potential. In this study, we introduce enhanced and post-reconstruction methodologies that address both issues.

### 2.4. PROPOSED SOLUTIONS

Let us consider a sequence of  $N$ -channel images acquired and registered over the same geographical area by an optical sensor at  $T$  different dates,  $X_b^{(i)}$  ( $i \in S = \{1, 2, \dots, T\}$  and  $b \in B = \{1, 2, \dots, N\}$ ). The specific problem of the detection of clouds is not dealt within this study. Accordingly, we assume that the original sequence of images has first been processed to generate a sequence of cloud/no cloud classification maps by using an automatic cloud-masking method or simply by photo-interpretation. Let  $N(C)$  be a spatial area over a cloud-contaminated image  $X^{(i)}$  ( $i \in S$ ) of the sequence such that  $N(C) = C \cup \bar{C}$  and  $C \cap \bar{C} = \emptyset$ , where  $C$  represents the considered cloudy area and  $\bar{C}$  stands for the cloud-free neighboring area.

Let  $Y_b^{(i)}$  be the image reconstructed from  $X_b^{(i)}$  using the CMLP method. This work aims at generating an improved reconstruction image  $Z_b^{(i)}$  from  $Y_b^{(i)}$  by opportunely capturing spatial and spectral correlations characterizing the considered images. At this end, we propose as a first method an improved prediction scheme that is:

- A multimodal prediction

Thereafter, we present two post-reconstruction methods which provide an improved version of the CMLP reconstructed image:

- A residual based predictors post-reconstruction,
- A contextual spatio-spectral post-reconstruction,

#### 2.4.1. SPECTRAL INFORMATION SOURCE

Its definition will mainly depend on both the used method and the availability or not of some prior knowledge about which channels in the multitemporal multispectral sequence are more suited to contribute to the improved or post-reconstruction of cloud-contaminated areas in the  $b$ th channel at time  $(t_i)$ .

#### 2.4.2. SPATIAL INFORMATION SOURCE

Incorporation of the spatial information in the proposed methods aims at taking advantage of the local properties between pixels in a predefined neighborhood system to further improve reconstruction accuracy. For this purpose we shall consider the common first and second-order spatial neighborhood systems (Fig. 2.1). The extension to larger neighborhood systems only causes superfluous complexity of the description without any more benefit [267].

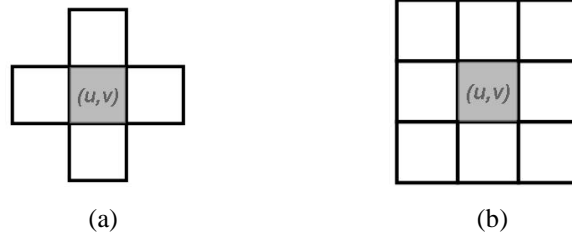


Fig. 2.1: Neighborhoods system. (a) First-order system. (b) Second-order system.

### 2.5. MULTIMODAL PREDICTOR

The multimodal predictor is a global predictor, similar to the one described in [244], which manipulates not only those temporal observations belonging to the channel to be predicted, but all spectral bands available in the multitemporal sequence. In the multimodal prediction scheme, the improved version  $Z_b^{(i)}$  of  $Y_b^{(i)}$  is defined as:

$$Z_b^{(i)}(u,v) = \begin{cases} X_b^{(i)}(u,v), & \text{if } (u,v) \notin C \\ \Phi[X_b^{(k)}(u,v) | N_\beta(X_b^{(k)}(u,v)), N_\gamma(X_b^{(k)}(u,v))] & k \in S_C, \text{ otherwise} \end{cases} \quad (2.1)$$

where  $[\cdot]$  is a prediction function, and  $N_\beta(\cdot)$  and  $N_\gamma(\cdot)$  represent spectral and spatial information sources, respectively.  $S_C$  is the subset of indexes corresponding to images  $X_b^{(k)}$  ( $k$   $i$ ) that are cloud-free in the spatial area  $N(C)$ .

#### 2.5.1. SPECTRAL INFORMATION

It can be expressed as a vector stacking the contributing channels from the multitemporal multispectral sequence:

$$N_\beta(X_b^{(k)}(u,v)) = [X_j^{(k)}(u,v) : j \in \Omega \text{ and } \Omega \subseteq B - \{b\}, k \in S_C] \quad (2.2)$$

## 2.5.2. SPATIAL INFORMATION

The spatial model, (SM1), used is defined as a simple stacked vector of the neighboring pixels:

$$N_\gamma(X_b^{(k)}(u,v)) = [X_j^{(k)}(p,q) : p \in \{u-1, u, u+1\}, q \in \{v-1, v, v+1\}, \\ (p,q) \neq (u,v), j \in \Omega, k \in S_C] \quad (2.3)$$

## 2.5.3. PREDICTION FUNCTION

[.] is formulated as an explicit combination of its information components:

$$\Phi[X_b^{(i)}(u,v) | N_\beta(X_b^{(i)}(u,v)), N_\gamma(X_b^{(i)}(u,v))] \\ = g[X_j^{(k)}(u,v), N_\beta(X_b^{(k)}(u,v)), N_\gamma(X_b^{(k)}(u,v))] \quad (2.4)$$

where  $g[.]$  is a global contextual prediction function that can be derived from both a linear and non linear combination of the information components of the multitemporal multispectral observations  $X_j^{(k)}$ , ( $j \in \Omega$  and  $\Omega \subseteq B - \{b\}$ ,  $k \in S_C$ ).

### 2.5.3.1. Linear Prediction Model

Given a contextual multitemporal multispectral vector  $\bar{X} = [X_s^1(u,v), X_s^2(u,v), \dots, X_s^K(u,v)]$  ( $K$  is the cardinality of  $S_C$ ), such that  $X_j^k(u,v)$  represents the vector of pixels values depicted in the spatial model (SM1) from the  $j$ th channel at time  $t_k$  of the observation sequence, the linear prediction model can be written as:

$$Z = g[X_s^1(u,v), X_s^2(u,v), \dots, X_s^K(u,v)] \\ = \sum_{k \in S_C} \sum_{s \in \Omega + \{b\}} \alpha_s^k(u,v) X_s^k(u,v) \quad (2.5)$$

where  $\alpha_s^k(u,v)$  stands for a vector of scalars weighting the contribution to the combination (2.5) of all vector components in the neighborhood system. A simple way to find the weight vectors is to solve the system (2.5) on the basis of the minimum square error pseudo-inverse technique [268].

### 2.5.3.2. Non linear Prediction Model – Prediction with SVM

In this case, the combination function  $g[.]$  is carried out through a nonparametric model based on the support vector machine (SVM) regression approach that has proved particularly effective to deal with different complex regression problems.

Given training data  $\{(x_i, y_i), i=1,2,\dots,N\} \subset \mathfrak{R}^d \times \mathfrak{R}$ , in  $\nu$ -SVM regression the goal is to find a function  $f(x)$  that has at most  $\nu$  deviation from the actually obtained targets  $y_i$  for all the training data, and at the same time is as flat as possible. This is achieved by non-linearly mapping the data from the input patterns space to a higher dimensional feature space, i.e.,  $\Phi : \mathfrak{R}^d \rightarrow \mathfrak{R}^{d'}$  ( $d' > d$ ). In this feature space, a linear function is constructed taking the form:

$$f(x) = w \cdot \Phi(x) + b \quad (2.6)$$

Flatness in (2.6) means that one seeks a small  $w$ . one way to ensure this is to solve the following optimization problem:

Minimize

$$\Psi(w, \xi, \xi^*) = \frac{1}{2} (w^T w) + C \sum_{i=1}^N (\xi_i + \xi_i^*) \quad (2.7)$$

Subject to

$$\begin{cases} y_i - (w \cdot \Phi(x_i) + b) \leq \varepsilon + \xi_i \\ (w \cdot \Phi(x_i) + b) - y_i \leq \varepsilon + \xi_i^*, & i = 1, 2, \dots, N \\ \xi_i, \xi_i^* \geq 0 \end{cases} \quad (2.8)$$

where  $\xi_i$  and  $\xi_i^*$  are the so-called *slack variables* introduced to account for samples that do not lie in the  $\varepsilon$ -deviation tube. The constant  $C > 0$  determines the trade-off between the flatness of  $f$  and the amount up to which deviations larger than  $\varepsilon$  are tolerated.

Equivalently, one can solve the dual formulation of the above optimization problem through a Lagrange functional, by introducing a dual set of variables:

Maximize

$$-\frac{1}{2} \sum_{i,j=1}^N (\alpha_i - \alpha_i^*)(\alpha_j - \alpha_j^*) K(x_i, x_j) - \varepsilon \sum_{i=1}^N (\alpha_i + \alpha_i^*) + \sum_{i=1}^N y_i (\alpha_i - \alpha_i^*) \quad (2.9)$$

Subject to

$$\sum_{i=1}^N (\alpha_i + \alpha_i^*) = 0 \quad \text{and} \quad \alpha_i, \alpha_i^* \in [0, C] \quad (2.10)$$

The final result is the *flattest* function written as:

$$f(x) = \sum_{i=1}^N (\alpha_i - \alpha_i^*) K(x_i, x) + b \quad (2.11)$$

Where  $K(\cdot, \cdot)$  is a kernel function,  $\alpha_i$  and  $\alpha_i^*$  are Lagrange multipliers.  $x_i$  is the image of a support vector in input space,  $\alpha_i$  and  $\alpha_i^*$  are the weight of a support vector in the feature space and  $b$  is a bias. Note that only those training samples associated to nonzero weights are called *support vectors*. The kernel is a function satisfying the Mercer's condition [269]. Examples of common nonlinear admissible kernels are the polynomial and the Gaussian kernel functions. For greater detail on  $\varepsilon$ -SVM see [270].

The non linear prediction is summarized through the following key steps:

### **Training Phase:**

1) Adopt a spatio-spectral information model.

For each band  $Z_b^{(i)}$  at time  $t_i$ , ( $b \in B$ ),

2) Collect the contextual training and validation samples from the area  $\bar{C}$  of the multitemporal multispectral observations  $X_s^{(k)}$  ( $s \in \{b\}$ ,  $k = i$ ).

3) Collect the corresponding target values  $z_b^{(i),l} = x_b^{(i),l}$  ( $l = 1, 2, \dots, Nt$ ), where  $Nt$  refers to the number of training and validation samples.

4) Train an  $\varepsilon$ -SVM post-predictor on the training set while tuning its parameters on the validation samples.

### **Reconstruction Phase:**

For each band  $Z_b^{(i)}$  at time  $t_i$ , ( $b \in B$ ), predict each contaminated observation in  $C$  by means of the related SVM predictor.

## **2.6. RESIDUAL BASED PREDICTION**

A second solution we propose facing the problem at hand is to investigate the possible validity of the Residual-Based Estimation (RBE) technique, used successfully in [271]-[273], as a post-reconstruction process.

The RBE method consists, basically, in the combination of two estimators; the functional estimator and the residual estimator. While the former provides an estimation model, the latter accomplishes the task of estimating the residuals (errors) generated by the functional estimator. A simple addition of the contribution of the two estimators is expected to offer a more accurate estimation. Two structure models are considered in this study:

- A sequential system,
- A parallel system.

### **2.6.1. SEQUENTIAL RESIDUAL-BASED PREDICTOR (SRBP)**

The SRBP system is shown in figure 2.2. Let  $x_s^{(k),l}$  ( $s \in \{a, b\}$ ,  $k \in S_C$ ,  $l=1, 2, \dots, N_l$ ) be a set of  $N_l$  contextual training vector samples, collected from the area  $\bar{C}$  in the multispectral multitemporal observation images  $X_s^{(k)}$ . A corresponding target set  $y^l$  ( $l=1, 2, \dots, N_l$ ) is that depicted from area  $\bar{C}$  in the  $b$ th band  $X_b^{(i)}$  at time  $t_i$ , to be predicted. The first estimator (functional estimator) (Fig. 2.2a) provides an estimation model between the image  $X_b^{(i)}$  and the observations  $X_s^{(k)}$  by means of a multimodal prediction process, described above, in which the predictor learns from information available in the feature space. We note that the prediction is applied over  $C$  and  $\bar{C}$  of the  $b$ th channel  $X_b^{(i)}$  to provide a full prediction  $\hat{Y}_b^{(i)}$  of the considered image  $X_b^{(i)}$  (i.e., inside and outside the cloud-contaminated area). The second estimator (residual estimator) is trained in a new feature space, defined by the contextual vector samples  $\hat{y}^f$  ( $f=1, 2, \dots, N_f$ ) collected from the area  $\bar{C}$  in the estimate  $\hat{Y}_b^{(i)}$ , to model in a supervised way the error function associated with the functional estimator (Fig. 2.2a) and defined as:

$$\varepsilon_b^{(i)} = X_b^{(i)} - \hat{Y}_b^{(i)} \quad (2.12)$$

This modeling will be used to deduce the residuals  $\hat{\varepsilon}$  that are generated by the functional estimator in the contaminated area  $C$ . The final estimate of the desired  $b$ th band  $Z_b^{(i)}$  is given by (Fig. 2.2b):

$$Z_b^{(i)} = \hat{Y}_b^{(i)} + \hat{\varepsilon}_b^{(i)} \quad (2.13)$$

Where:

$$\hat{\varepsilon}_b^{(i)}(u, v) = \begin{cases} X_b^{(i)}(u, v) - \hat{Y}_b^{(i)}(u, v), & \text{if } (u, v) \notin C \\ \Psi[\hat{Y}_b^{(i)}(u, v) | N_\beta(\hat{Y}_b^{(i)}(u, v), N_\gamma(\hat{Y}_b^{(i)}(u, v))], & \text{otherwise} \end{cases} \quad (2.14)$$

Similarly to what was done for the multimodal predictor,  $\Psi[\cdot]$  is a contextual prediction function which is carried out by using both linear and nonlinear regression methods, with  $N_\beta(\cdot)$  and  $N_\gamma(\cdot)$  as the spectral and spatial information sources respectively.

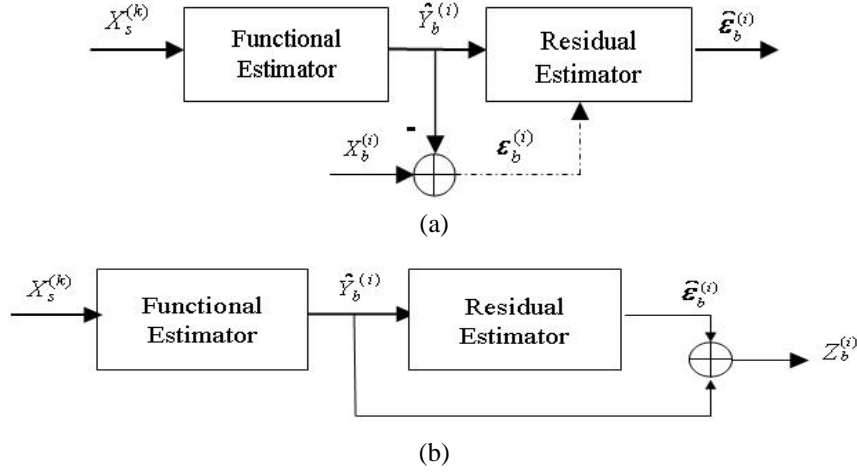


Fig.2.2: Block diagram of the SRBP system. (a) Training phase of the residual estimator. (b) Estimation phase of the SRBP.

### 2.6.1.1 Spectral Information

The spectral information resumes to the single CMLP or CNP estimate  $b$ th channel  $\hat{Y}_b^{(i)}$ .

### 2.6.1.2 Spatial Information

The spatial model, (SM1), used here is defined as:

$$N_\gamma(\hat{Y}_b^{(i)}(u,v)) = [\hat{Y}_b^{(i)}(p,q) : p \in \{u-1, u, u+1\}, q \in \{v-1, v, v+1\}, (p,q) \neq (u,v)] \quad (2.15)$$

#### • Linear Prediction Model

Under a linear regression model the residuals in the  $b$ th band are modeled by the following linear combination:

$$\hat{\epsilon} = h[\hat{y}_{(u,v)}] = \sum_{(u,v)} \beta_{(u,v)} \hat{y}_{(u,v)} \quad (2.16)$$

The scalar weights vectors  $\beta_{(u,v)}$  are calculated by solving the system (2.16) on the basis of the minimum square error pseudo-inverse technique. Each contaminated observation in  $C$  is then post-reconstructed by means of the equation (2.13).

#### • Non Linear Prediction Model

In this case, the residuals are estimated by means of the nonparametric model based on the SVM regression approach which involves both training and post-reconstruction phases.

#### *Algorithm:*

- 1) Adopt a spatio-spectral information model.  
For each image channel  $Z_b^{(i)}$  at time  $t_i$ , ( $b \in B$ ),
- 2) Predict each cloud-free observation  $\hat{Y}_b^{(i)}(\cdot)$  in  $\bar{C}$  using either the CMLP or the CNP method.

- 3) Compute the resulting reconstruction error  $\varepsilon_b^{(i)}(.)$  for each sample  $(u,v)$  of  $\bar{C}$  by means of equation (2.12).
- 4) Collect training and validation samples and their related error target values from  $\bar{C}$ .
- 5) Train an SVM predictor of the reconstruction errors on the training set while tuning its parameters on the validation samples.
- 6) Predict each reconstruction error  $\hat{\varepsilon}_b^{(i)}(.)$  for each sample  $(u,v)$  of  $C$  by means of the trained SVM predictor.
- 7) Post-predict each contaminated observation in  $C$  by means of the equation (2.13).

### 2.6.2. PARALLEL RESIDUAL-BASED PREDICTOR (PRBP)

The PRBP system is that shown in Fig. 2.3. The functional estimator is exactly similar to the one described in the SRBP system. The residual estimator (Fig. 2.3a), however, analyzes and models in the same feature space (set  $x_s^{(k),l}$  ( $s \in \Omega + \{b\}$ ,  $k \in S_C$ ,  $l=1, 2, \dots, N_l$ ) from the area  $\bar{C}$  in the multispectral multitemporal observations  $X_s^{(k)}$ ) the error function associated with the functional estimator and defined by the quantity (2.12). This analysis will serve, obviously, to guess the residuals  $\hat{\varepsilon}$  that are generated by the functional estimator in the contaminated area  $C$  and consequently to post-predict each contaminated observation in  $C$  by means of the equation (2.13), (Fig. 2.3b). This scheme can also be carried out by using both linear and nonlinear regression methods incorporating spectral and spatial information sources.

#### 2.6.2.1 Spectral Information

It is expressed as a vector stacking the contributing channels described in equation (2.2).

#### 2.6.2.2 Spatial Information

The spatial model (SM1) used here is that described in equation (2.3).

##### • Linear Prediction Model

In this case, the residuals in the  $b$ th band are modeled by the same linear combination of equation (2.5) such that:

$$\begin{aligned} \hat{\varepsilon} &= \tilde{g} \left[ x_s^1(u,v), x_s^2(u,v), \dots, x_s^K(u,v) \right] \\ &= \sum_{k \in S_C} \sum_{s \in \Omega + \{b\}} \alpha_s^k(u,v) x_s^k(u,v) \end{aligned} \quad (2.17)$$

Obviously, the scalar weights vectors  $\alpha_s^k(u,v)$  are calculated by solving the system (2.17) on the basis of the minimum square error pseudo-inverse technique.

##### • Non Linear Prediction Model

Similarly, the residuals here are estimated by means of the nonparametric model based on the -SVM regression approach.

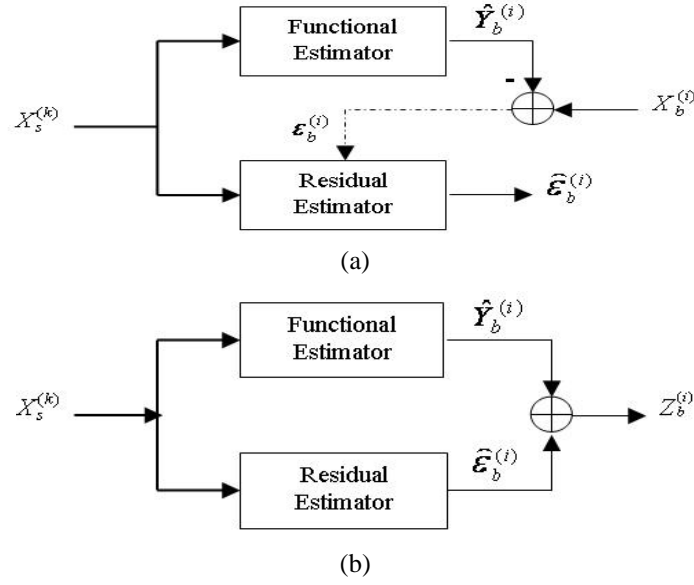


Fig.2.3: Block diagram of the PRBP system. (a) Training phase of the residual estimator. (b) Estimation phase of the SRBP

**Algorithm:**

- 1) Adopt a spatio-spectral information model.

For each image channel  $Z_b^{(i)}$  at time  $t_i$ , ( $b \in B$ ),

- 2) Predict each cloud-free observation  $\hat{Y}_b^{(i)}(.)$  in  $\bar{C}$  using either the CMLP or the CNP method.
- 3) Compute the resulting reconstruction error  $\epsilon_b^{(i)}(.)$  for each sample  $(u, v)$  of  $\bar{C}$  by means of equation (2.12).
- 4) Collect training and validation samples from the multitemporal multispectral observations and their related error target values from  $\bar{C}$ .
- 5) Train the SVM predictor of the reconstruction errors on the training set while tuning its parameters on the validation samples.
- 6) Predict each reconstruction error  $\hat{\epsilon}_b^{(i)}(.)$  for each sample  $(u, v)$  of  $C$  by means of the trained SVM predictor.
- 7) Post-predict each contaminated observation in  $C$  by means of the equation (2.13).

## 2.7. CONTEXTUAL SPATIO-SPECTRAL POST-RECONSTRUCTION

In this section, we introduce a post-reconstruction methodology that addresses the issues stated previously in the formulation of the problem at hand, that is to say the incorporation of both spatial and spectral information sources to get an improved reconstruction quality. Moreover, as a third methodological improvement, we also propose facing a problem that has not yet been addressed in the remote sensing literature, i.e. the generation of an error map besides the reconstructed images in order to provide the end-user with an indication about the degree of reconstruction reliability associated with each reconstructed pixel [274],[275].

### 2.7.1. DESCRIPTION OF THE METHOD

Let  $Y_b^{(i)}$  be the CMLP reconstructed image from  $X_b^{(i)}$  (Fig. 2.4). For notation simplicity, we shall drop the superscript  $i$ . The contextual spatio-spectral post-reconstruction (CSSPR)

process aims at generating an improved reconstruction image  $Z_b$  from  $Y_b$  by means of the following formulation:

$$Z_b(u, v) = \begin{cases} Y_b(u, v) = X_b(u, v), & \text{if } (u, v) \notin C \\ \Theta[Y_b(u, v) | N_\beta(Y_b(u, v)), N_\gamma(Y_b(u, v))] & \text{otherwise} \end{cases} \quad (2.18)$$

where  $[\cdot]$  is a post-prediction function with  $N_\beta(\cdot)$  and  $N_\gamma(\cdot)$  as spectral and spatial information sources, respectively.

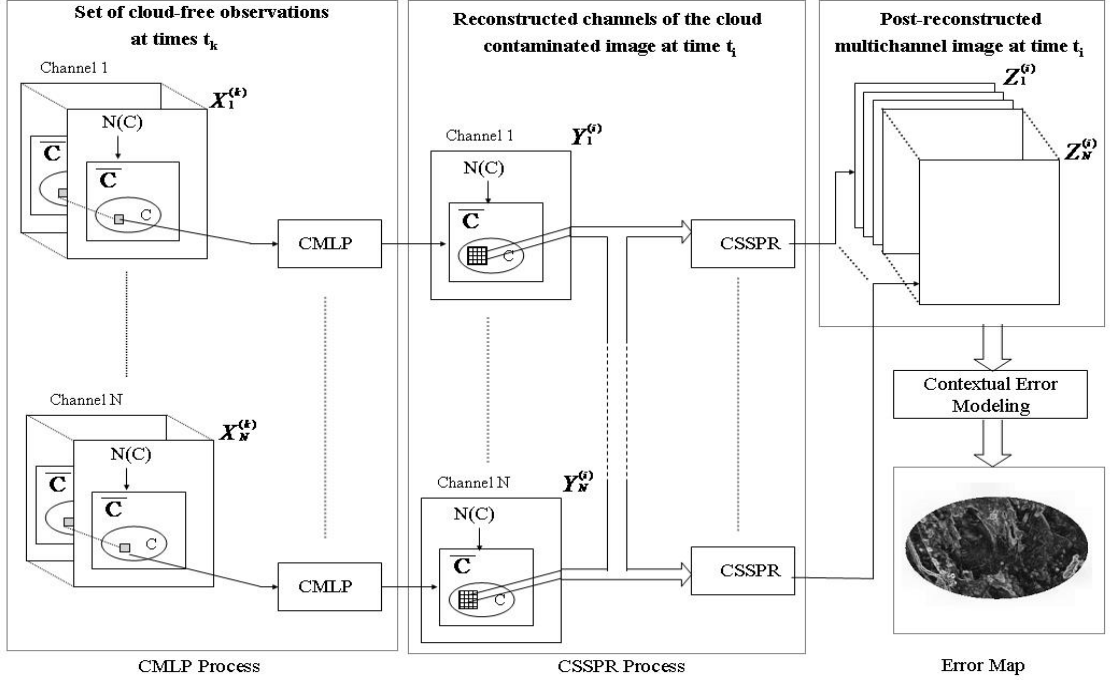


Fig.2.4: Block scheme of the whole contextual reconstruction process.

### 2.7.2. SPECTRAL INFORMATION

In general, it can be simply expressed as a vector stacking the contributing channels:

$$N_\beta(Y_b(u, v)) = [Y_i(u, v) : i \in \Omega \text{ and } \Omega \subseteq B - \{b\}] \quad (2.19)$$

### 2.7.3. SPATIAL INFORMATION

In this method, we shall investigate three different spatial models to analyze which of is better adapted to our post-reconstruction problem. For all the three models, we shall make use of the common second-order spatial neighborhood system.

As in the previous methods, the first spatial model (SM1) is defined as a simple stacked vector of the neighboring pixels:

$$N_\gamma(Y_b(u, v)) = [Y_b(p, q) : p \in \{u-1, u, u+1\}, q \in \{v-1, v, v+1\}, (p, q) \neq (u, v)] \quad (2.20)$$

The second model (SM2) is derived from the autobinomial model originally presented in [276]:

$$N_\gamma(Y_b(u,v)) = \left[ \begin{array}{l} \beta_{11} \cdot \frac{Y_b(u,v-1) + Y_b(u,v+1)}{G}, \beta_{12} \cdot \frac{Y_b(u-1,v) + Y_b(u+1,v)}{G}, \\ \beta_{21} \cdot \frac{Y_b(u-1,v+1) + Y_b(u+1,v-1)}{G}, \beta_{22} \cdot \frac{Y_b(u-1,v-1) + Y_b(u+1,v+1)}{G} \end{array} \right] \quad (2.21)$$

where the  $\beta$ 's express the weight of each spatial direction in the neighborhood system and  $G$  denotes the maximum grey level value. On the one hand, SM2 presents the advantage that it is more compact than SM1. On the other, it raises a weight estimation problem. We shall tackle this issue by adopting the algorithm described in [174].

Finally, the third model (SM3) is based on the median-type predictor used for isolating transmission errors in predictive coding [277]:

$$N_\gamma(Y_b(u,v)) = [\gamma_1(u,v), \gamma_2(u,v)] \quad (2.22)$$

where:

$$\gamma_1(u,v) = \text{Median} \left[ \begin{array}{l} Y_b(u,v-1), \frac{Y_b(u-1,v+1)}{2} + Y_b(u,v-1) + \frac{Y_b(u+1,v-1)}{4}, \\ 2Y_b(u-1,v+1), 2Y_b(u-1,v+1) + \frac{Y_b(u,v-1)}{2} - Y_b(u+1,v-1) \end{array} \right] \quad (2.23)$$

$$\gamma_2(u,v) = \text{Median} \left[ \begin{array}{l} Y_b(u,v+1), \frac{Y_b(u+1,v-1)}{2} + Y_b(u,v+1) + \frac{Y_b(u-1,v+1)}{4}, \\ 2Y_b(u+1,v-1), 2Y_b(u+1,v-1) + \frac{Y_b(u,v+1)}{2} - Y_b(u-1,v+1) \end{array} \right]$$

This model seems attractive a priori since it is compact and parameter-free. We note that compactness is a desirable property since it allows to limit the dimensionality of the space where the prediction function  $[.]$  will be defined.

#### 2.7.4. PREDICTION FUNCTION

Similarly to what was done in the previous methods,  $[.]$  is a post-prediction function derived from a nonparametric model based on the  $\gamma$ -SVM regression approach.

#### 2.7.5. ERROR MAP GENERATION

The unsupervised nature of cloud-contaminated image reconstruction problems makes it difficult to provide the user with a result conveying a form of self-evaluation. The choice of a reconstruction method is typically done on the basis of the accuracy it achieves on simulation experiments. Thus the user is somewhat constrained to trust any result obtained for real reconstruction scenarios by the selected method without any indication of its actual reliability. In this work, an attempt to provide an answer to this issue is proposed. It relies on the idea of providing the user with an error map associated with the (CSSPR) post-reconstruction result so as to give an indication of the degree of reliability associated with each post-reconstructed pixel. This map will thus accompany the post-reconstructed image in each of its applications. During photo-interpretation or after automatic processing for thematic information extraction, such as land cover/use classification and change detection, the user can decide whether or not to discard an area that originates from a reconstruction process by consulting the error map. In addition to a downstream use of the error map, reconstruction errors may be exploited

upstream by integrating them through a weighting mechanism within the thematic information extraction process in order to improve its reliability.

To this purpose, we shall go round the unsupervised nature of the problem by exploiting information available in  $\bar{C}$  to deduce in a supervised way a contextual error model that will be used for guessing errors generated by the CSSPR process in  $C$ . In greater detail, first the CSSPR method is applied over  $C$  and  $\bar{C}$  of each channel  $Y_b^{(i)}$  ( $b \in B$ ) to provide a full post-reconstruction  $\tilde{Z}^{(i)}$  of the considered image  $Y^{(i)}$  (i.e., inside and outside the cloud-contaminated area). We note that  $\tilde{Z}^{(i)} = Z^{(i)}$  in  $C$ , while  $\tilde{Z}^{(i)} \neq Z^{(i)}$  in  $\bar{C}$ , where  $Z^{(i)} = X^{(i)}$ . This step is important since it allows quantifying post-reconstruction errors in the cloud-free region ( $\bar{C}$ ) of the image by comparing each post-reconstructed pixel with its known true value:

$$\xi_b(u, v) = |\tilde{Z}_b(u, v) - X_b(u, v)| \quad (b \in B \text{ and } (u, v) \in \bar{C}) \quad (2.24)$$

where  $\tilde{Z}_b(u, v)$  and  $X_b(u, v)$  are the post-reconstructed and original cloud-free pixels at the  $(u, v)$ th location, respectively. The resulting contextual single-channel error maps are then combined through an  $L2$ -norm operator to generate a single contextual  $L2$ -norm error map:

$$\|\xi(u, v)\| = \sqrt{\sum_{b=1}^N (\xi_b(u, v))^2} \quad ((u, v) \in \bar{C}) \quad (2.25)$$

This contextual map aims at inferring by regression a contextual error model (for  $\bar{C}$ ) that will be used to approximate the errors generated in the cloud-contaminated area  $C$ . Similarly, we shall adopt the SVM regression approach to predict contextual  $L2$ -norm errors as follows:

$$\|\hat{\xi}(u, v)\| = I[\tilde{Z}_1(u, v), N_\gamma(\tilde{Z}_1(u, v)), \dots, \tilde{Z}_N(u, v), N_\gamma(\tilde{Z}_N(u, v))] \quad (2.26)$$

### 2.7.6. ALGORITHMIC DESCRIPTION

The CSSPR post-reconstruction and error map generation processes (Fig.2.4) are summarized through the following key steps:

#### **Training Phase:**

- 1) Adopt a spatio-spectral information model.
- 2) For each image channel  $Z_b$  ( $b \in B$ ),
  - Collect the contextual training and validation samples from the area  $\bar{C}$  of the images  $Y_a$  ( $a \in \Omega(b) + \{b\}$ ) reconstructed with the CMLP method.
  - Collect the corresponding target values  $z_b^l = x_b^l$  ( $l=1, 2, \dots, N_l$ ), where  $N_l$  refers to the number of training and validation samples.
  - Train an SVM post-predictor on the training set while tuning its parameters on the validation samples.

#### **Post-Reconstruction Phase:**

For each image channel  $Z_b$  ( $b \in B$ ), post-predict each contaminated observation in  $C$  by means of the related SVM predictor.

#### **Error Map Generation:**

- 1) For each image channel  $Z_b$  ( $b \in B$ ),

- Post-predict each (cloud-free) observation in  $\bar{C}$  using the previously trained post-prediction model.
  - Compute the resulting contextual post-reconstruction error  $\xi_b(\cdot)$  for each sample  $(u, v)$  of  $\bar{C}$ .
- 2) Using (2.25), compute the contextual  $L2$ -norm error  $\xi(\cdot)$  for each sample  $(u, v)$  of  $\bar{C}$ .
  - 3) Collect training and validation samples and their related  $L2$ -norm error target value from  $\bar{C}$ .
  - 4) Train an SVM predictor of the  $L2$ -norm errors on the training set while tuning its parameters on the validation samples.
  - 5) Generate the error map over  $C$  by means of the trained SVM predictor.

## 2.8. EXPERIMENTAL RESULTS

### 2.8.1 DATA SET DESCRIPTION AND EXPERIMENT DESIGN

In order to perform simulation experiments for the quantitative assessment of the proposed methodologies, we considered the same images used in [151]. They represent a set of multitemporal multispectral cloud-free images acquired with the Landsat-7 ETM+ sensor over the Trentino area in Northern Italy in May, July and September 2000 (Figs. 2.5-2.6). The main land covers characterizing these images include forest, grass, rock, urban areas, vineyard and water. The three images exhibit a very similar spatial structure while some changes in the spectral appearance of vegetated areas due to natural seasonal effects can be observed.

We made extensive tests on the data described above. The simulation experiments conducted within the multimodal prediction and the residual based prediction methods aim at assessing the post-reconstruction quality for a given image channel subject to a constant cloud contamination conditions whereas the CSSPR algorithm uses for the same goal different cloud contamination conditions including the typology of obscured ground cover and the size of the contaminated area. In addition, in the CSSPR method a second set of computations is conducted to assess the post-reconstruction performance over all channels of the image for a given cloud-contamination simulation (that corresponding to the largest simulated cloud).

For the purpose of evaluating the contribution of the spectral and spatial contextual information sources to the proposed processes, experiments were conducted exploiting them jointly as well as separately. We note that both of the multimodal prediction and the residual based prediction methods use only one spatial model, whereas the CSSPR method uses three different ones. Similarly to what was done in [151], we adopted for the three methods the following metrics for post-reconstruction accuracy evaluation: the mean square error (MSE) and the error bias computed over the reconstructed area, in addition of the impact on the classification process inside and outside the contaminated area for the CSSPR method.

The simulation of different cloud-contamination conditions was carried out by adopting two groups of masks (Fig. 2.7). The first group includes masks  $(C_{1,2,3,4})$  whose positions were selected in such a way as to simulate the obscuration of different kinds of ground covers. The second (masks  $C_{A,B,C,D}$ ) was adopted to simulate increasing cloud cover sizes, varying from 3.2% ( $C_A$ ) to 48.6% ( $C_D$ ) of the total image size. In all the methods, the masking was applied on the July image (assumed to be the cloud-contaminated image) while the May and September images were used as cloud-free input images.

Finally, in all the methods the SVM regression approach was implemented with the nonlinear Gaussian kernel.

### 2.8.2. PREVIOUS RESULTS

The methods described here are a follow up of the CMLP and CNP methods. As a starting point, we will show in Fig.2.8 an example of a CMLP achieved reconstruction results for Band 2 of the considered July subimage masked with ( $C_D$ ), the largest simulated cloud cover.

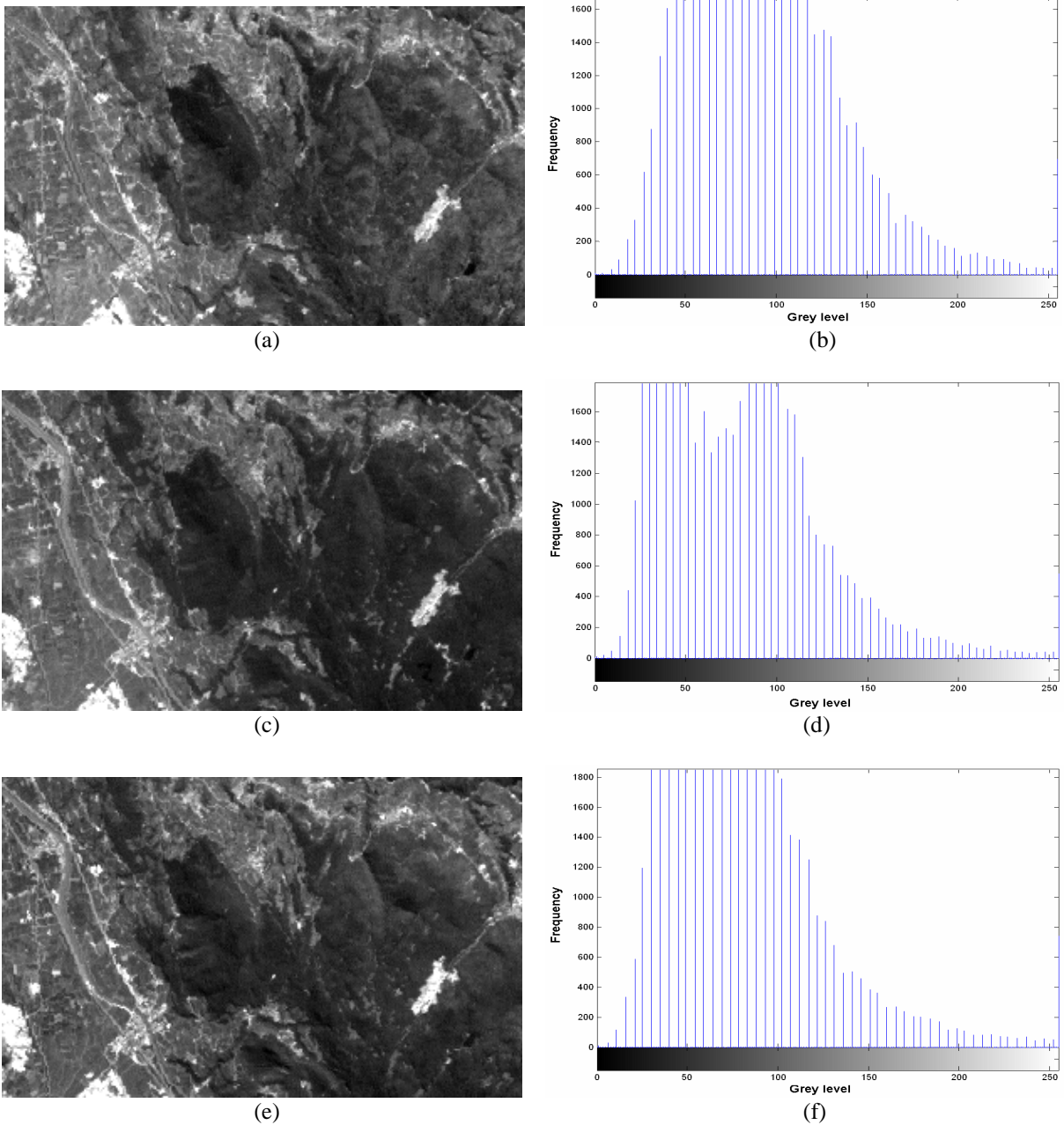


Fig.2.5: Cloud-free portion of the multispectral multitemporal sequence used in the simulations: band 2. a) Original May subimage. b) Histogram of May subimage. c) Original July subimage. d) Histogram of July subimage. e) Original September subimage. f) Histogram of September subimage.

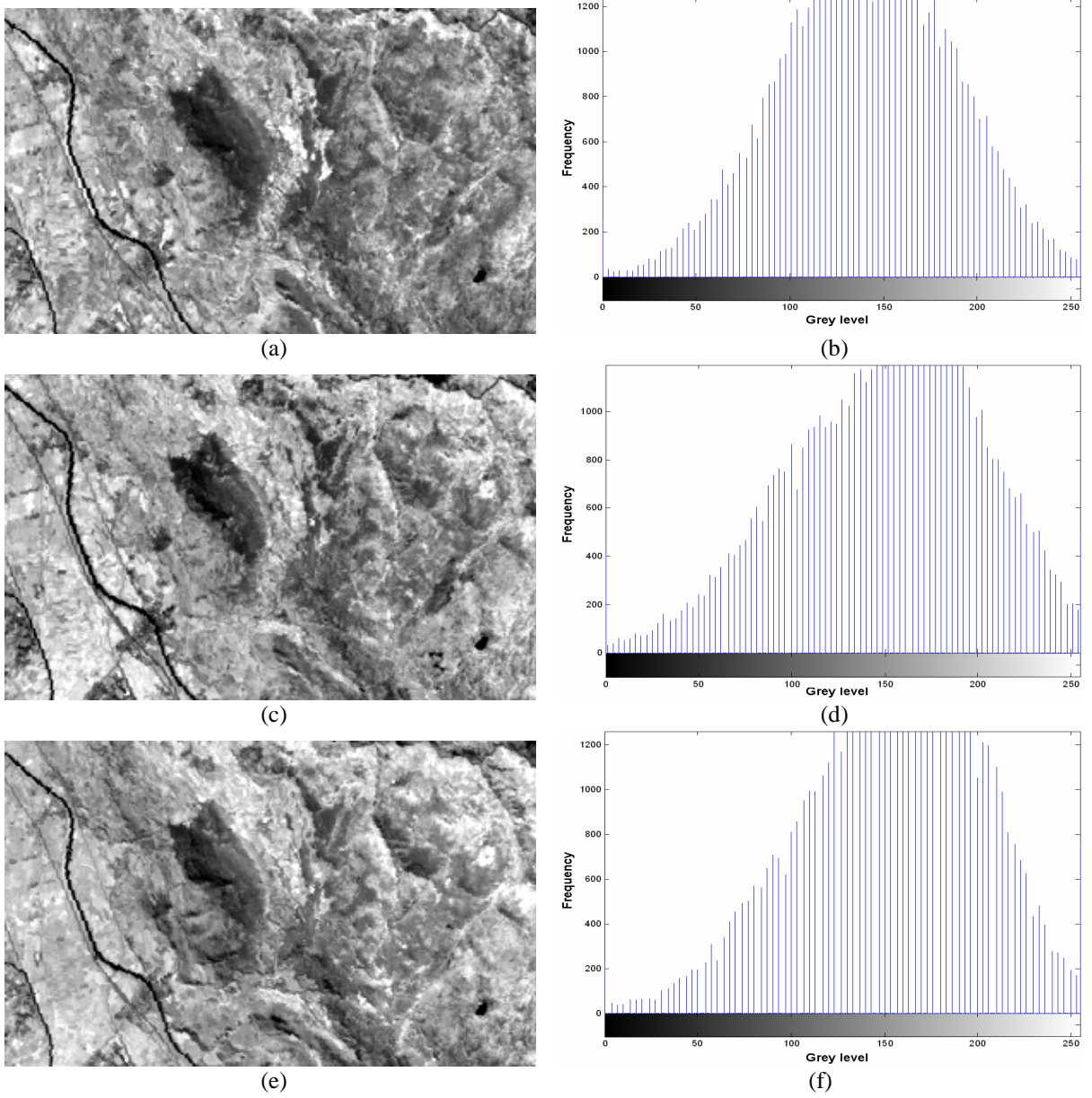


Fig.2.6: Cloud-free portion of the multispectral multitemporal sequence used in the simulations: band 4. a) Original May subimage. b) Histogram of May subimage. c) Original July subimage. d) Histogram of July subimage. e) Original September subimage. f) Histogram of September subimage.

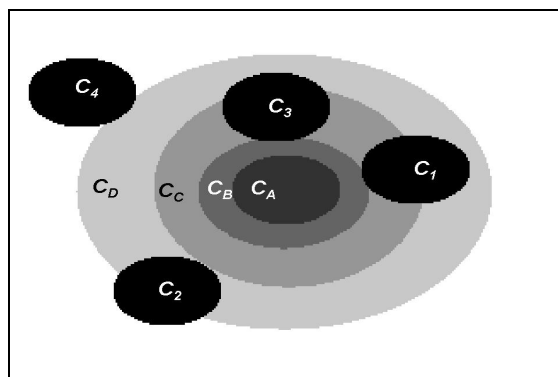
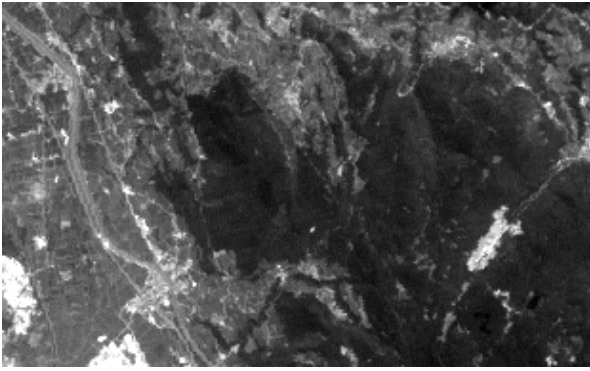
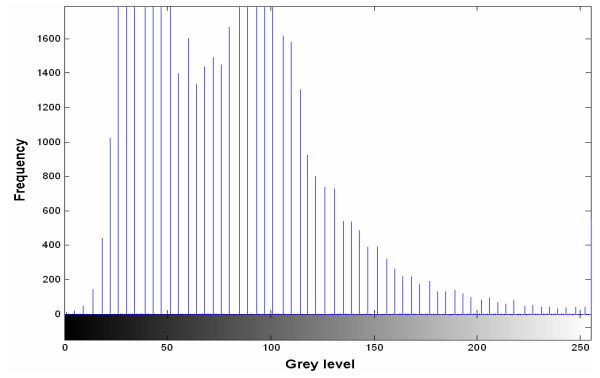


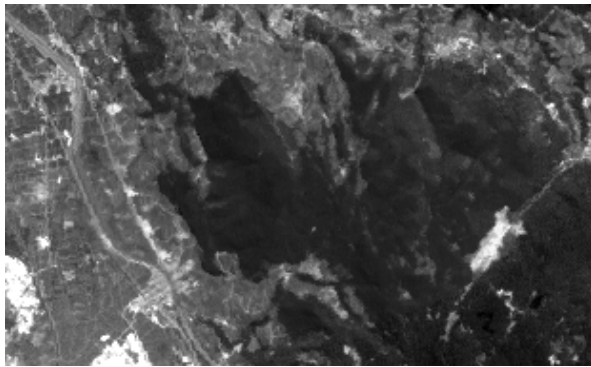
Fig.2.7: Masks adopted to simulate different cloud contaminations.



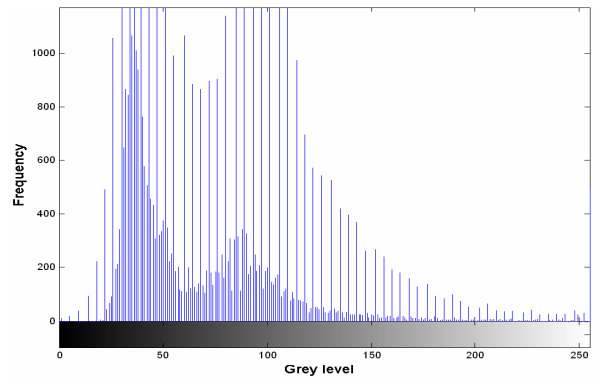
(a)



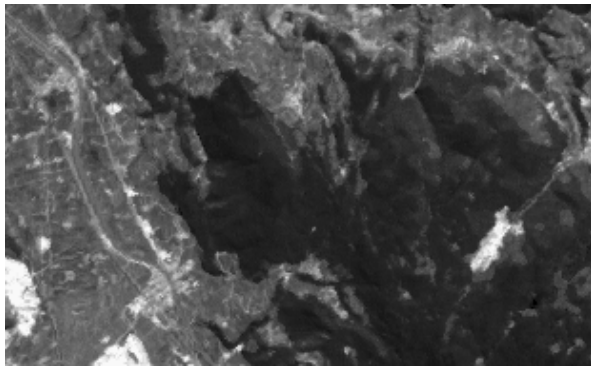
(b)



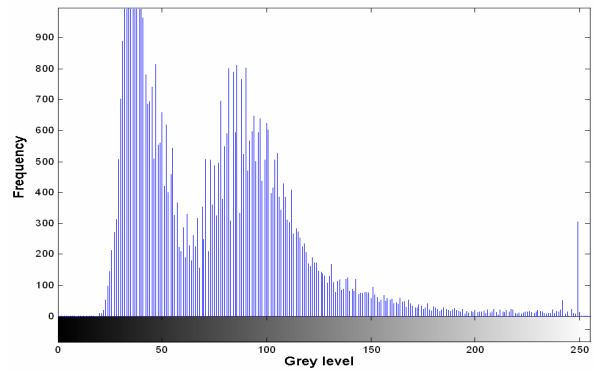
(c)



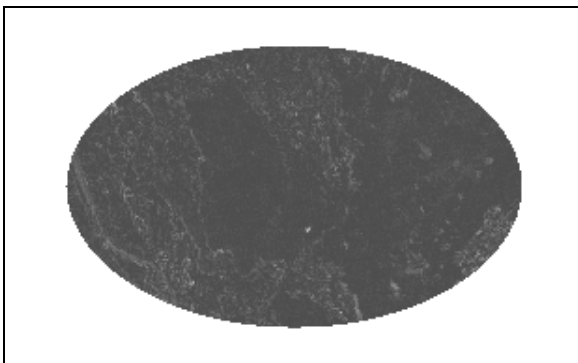
(d)



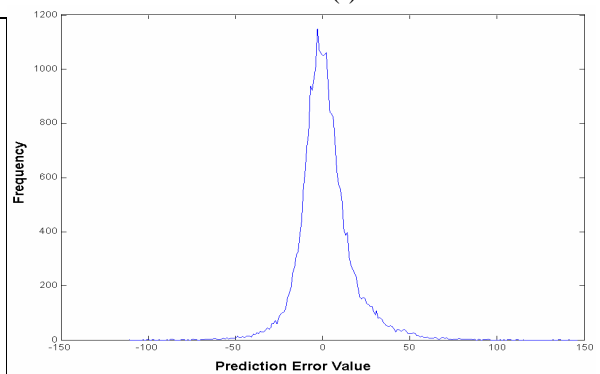
(e)



(f)



(g)



(h)

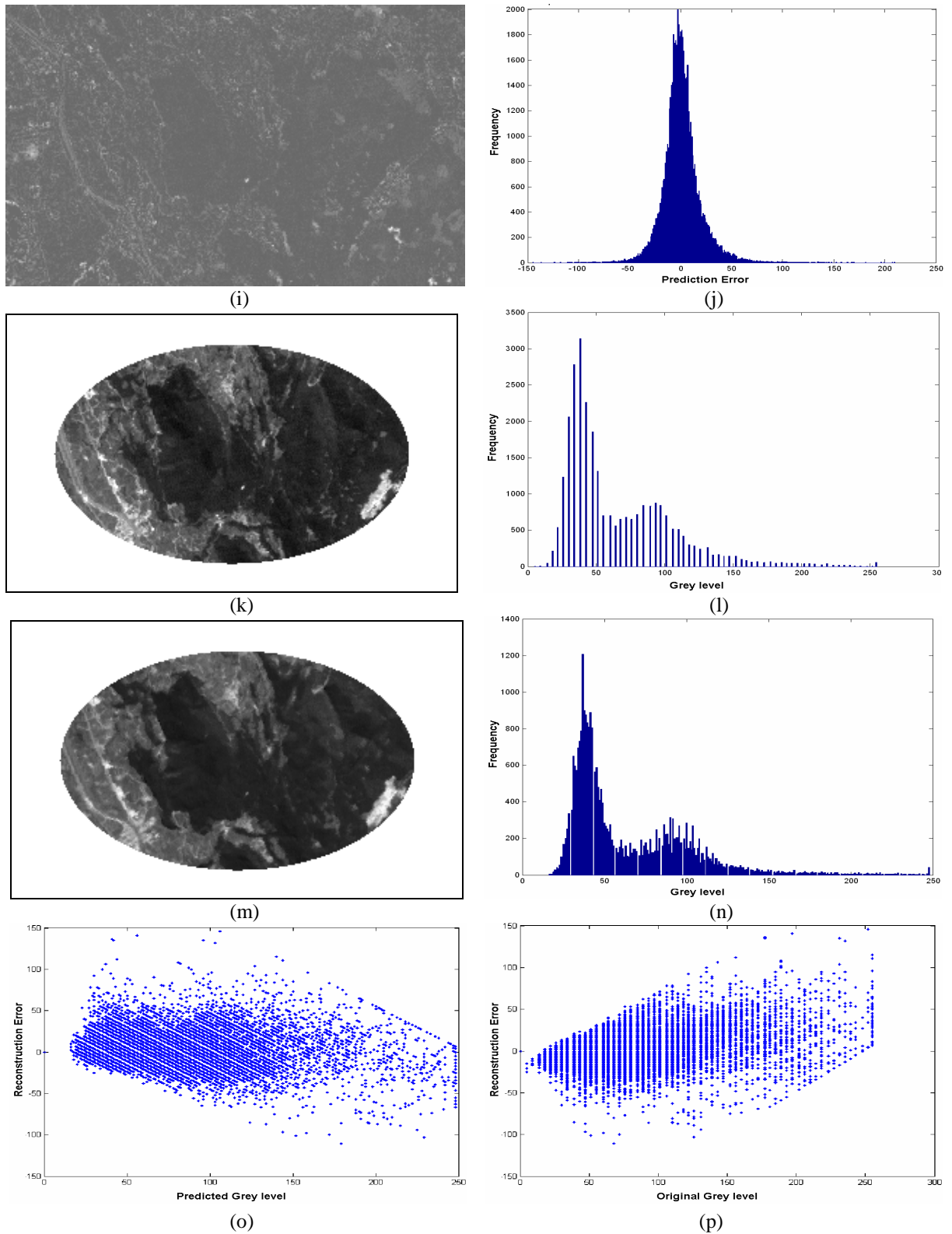


Fig.2.8: CMLP reconstruction results obtained after contamination with the largest simulated cloud  $C_D$  of channel 2 of the July image. (a) Original July subimage. (b) Histogram of original image. (c) CMLP reconstructed image inside the cloud  $C_D$ . (d) Histogram of image in (c). (e) Reconstructed image inside and outside cloud  $C_D$ . (f) Histogram of image in (e). (g) Difference image between images (a) and (c). (h) Histogram of prediction error in (g). (i) Difference image between images (a) and (e). (j) Histogram of image in (i). (k) Original masked area. (l) Histogram of the original masked area. (m) Reconstructed masked area. (n) Histogram of the reconstructed masked area. (o) Scatter of the reconstruction errors versus the predicted pixels inside the cloud. (p) Scatter of the reconstruction errors versus the original pixels inside the cloud.

### 2.8.3. MULTIMODAL PREDICTION SIMULATIONS

Table 2.1 shows the quantitative results of the linear multimodal prediction (LMP), obtained on channels 1, 2 and 3 masked by the largest cloud cover mask  $C_D$  which represents 48.6% of the total image size. Depending on the kind of used information, different variants of the method were applied to reconstruct each of the three channels. The obtained gains of MSE and bias are reported with respect to the CMLP method. From the results, we see that the lowest gains in terms of MSE are those obtained when exploiting only the spectral information (-8.6% for band 1, 1.7% for band 2 and -1.4% for Band 3). In comparison, the gains are higher when using solely the spatial information (14.1% for band 1, 5.4% for band 2 and 14.0% for Band 3). The fusion of both information sources allows better results further (18.9% for band 1, 22.8% for band 2 and 17.2% for Band 3). The gains in terms of bias, however, vary inversely such that they are the lowest when incorporating only the spatial information (44.1% for band 1, -62.9% for band 2 and -32.0% for Band 3) and increase significantly while using the spectral information separately (83.0% for band 1, 81.1% for band 2 and 72.8% for Band 3). As for the MSE gains, the best results are obtained with the fusion of both information sources (99.8% for band 1, 59.6% for band 2 and 76.9% for Band 3). Figs. 2.9-2.11 display an example of achieved reconstruction of channels 1, 2 and 3 respectively, using both spatial and spectral information sources.

As for the linear prediction model, Table 2.2 shows the quantitative results of the nonlinear multimodal prediction (NMP) obtained on channels 1, 2 and 3 under the same contamination conditions and for different variants of the method, depending on the used information source. Obviously, the obtained gains of MSE and bias are reported with respect to the CNP method. The results confirm that the spatial-based method produces MSE gains superior to the spectral-based method (17.0% vs. 0.7% for band 1, 20.9% vs. 17.2% for band 2 and 17.6% vs. 3.4% for band 3), while the fusion of the two information sources remains the best way to get higher accuracies (21.8% for band 1, 31.7% for band 2 and 19.2% for band 3). Unlike the linear prediction model, the gains on the bias, here, vary differently from one band to another. Nonetheless, the best results are still obtained when spatial and spectral information sources are jointly used. An example of achieved reconstruction of channels 1, 2 and 3 are displayed in Figs. 2.12-2.14.

Band	Method		MSE	MSE-Gain [%]	Bias	Bias Gain [%]	
1	<b>CMLP</b>		<b>238.78</b>	<b>-</b>	<b>1.88</b>	<b>-</b>	
	LMP	Spectral	259.41	- 8.6	0.32	83.0	
		Spatial	SM1	204.93	14.1	1.05	44.1
		Spatial + spectral	SM1	193.75	18.9	0.004	99.8
2	<b>CMLP</b>		<b>259.2</b>	<b>-</b>	<b>1.7</b>	<b>-</b>	
	LMP	Spectral	254.70	1.7	0.32	81.1	
		Spatial	SM1	245.13	5.4	2.77	- 62.9
		Spatial + spectral	SM1	200.19	22.8	0.76	59.6
3	<b>CMLP</b>		<b>331.24</b>	<b>-</b>	<b>1.47</b>	<b>-</b>	
	LMP	Spectral	336.15	- 1.4	0.4	72.8	
		Spatial	SM1	284.90	14.0	1.94	- 32.0
		Spatial + spectral	SM1	274.39	17.2	0.34	76.9

TABLE 2.1. QUANTITATIVE RESULTS OBTAINED BY THE LINEAR MULTIMODAL PREDICTION.

Band	Method		MSE	MSE Gain [%]	Bias	Bias Gain [%]	
1	<b>CNP</b>		<b>252.59</b>	-	<b>0.79</b>	-	
	NMP	Spectral	250.44	0.7	1.12	- 41.8	
		Spatial	SM1	209.80	17.0	2.15	- 172.2
		Spatial + spectral	SM1	197.64	21.8	0.36	54.4
2	<b>CNP</b>		<b>289.0</b>	-	<b>2.9</b>	-	
	NMP	Spectral	239.24	17.2	1.9	34.5	
		Spatial	SM1	228.66	20.9	1.53	47.2
		Spatial + spectral	SM1	197.41	31.7	1.45	50.0
3	<b>CNP</b>		<b>341.74</b>	-	<b>2.75</b>	-	
	NMP	Spectral	330.04	3.4	3.4	- 23.1	
		Spatial	SM1	281.51	17.6	2.2	20.3
		Spatial + spectral	SM1	276.19	19.2	2.7	2.2

TABLE 2.2. QUANTITATIVE RESULTS OBTAINED BY THE NON LINEAR MULTIMODAL PREDICTION.

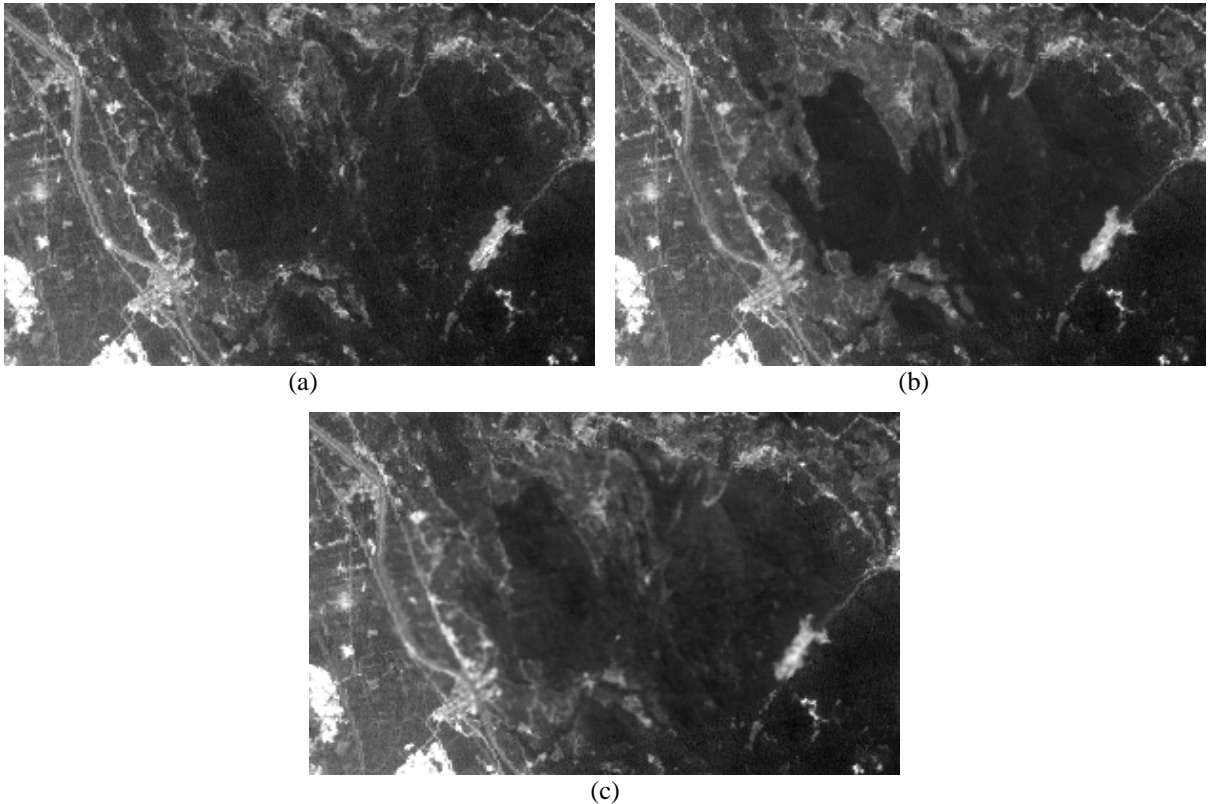


Fig.2.9: Linear multimodal prediction reconstruction results obtained after contamination with the largest simulated cloud  $C_D$  of channel 1 of the July image using both spectral and spatial information sources. a) Original subimage. b) CMLP reconstructed image (MSE = 238.78). c) LMP reconstructed image (MSE = 193.75).

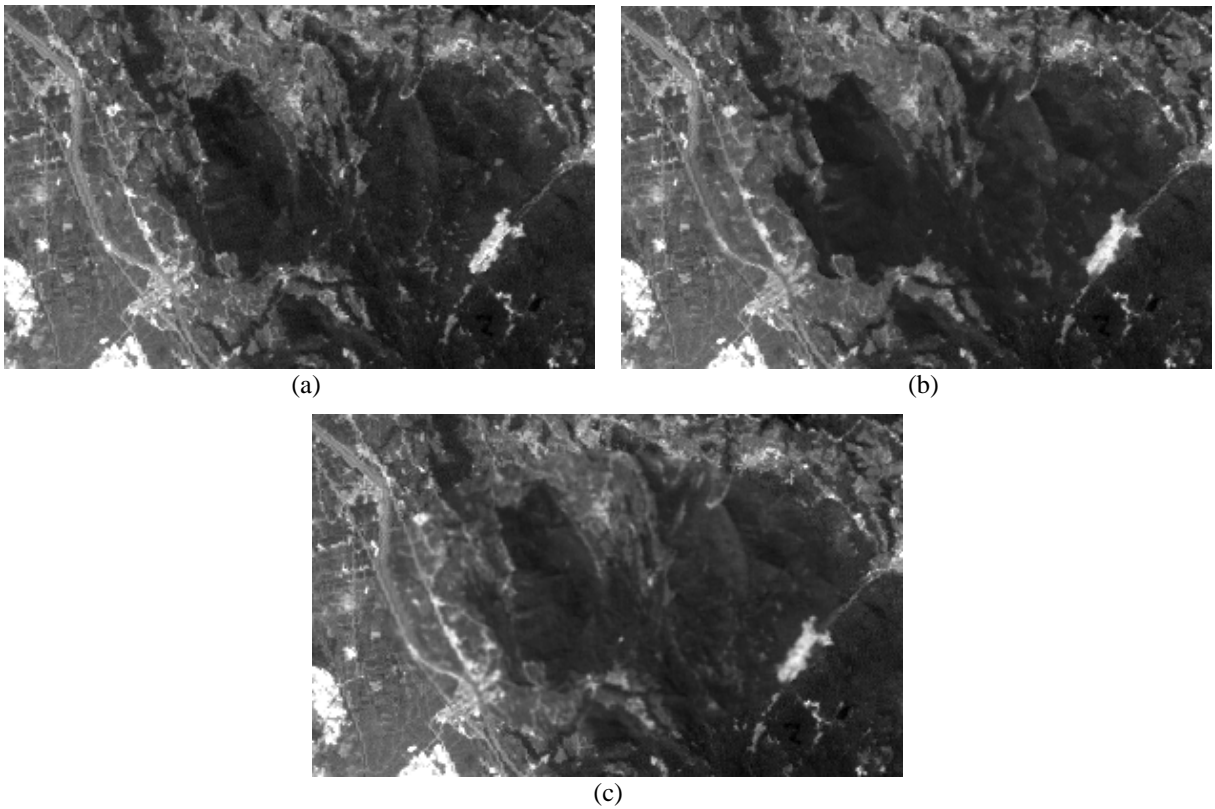


Fig.2.10: Linear multimodal prediction reconstruction results obtained after contamination with the largest simulated cloud  $C_D$  of channel 2 of the July image using both spectral and spatial information sources. a) Original subimage. b) CMLP reconstructed image (MSE = 259.2). c) LMP reconstructed image (MSE = 200.19).

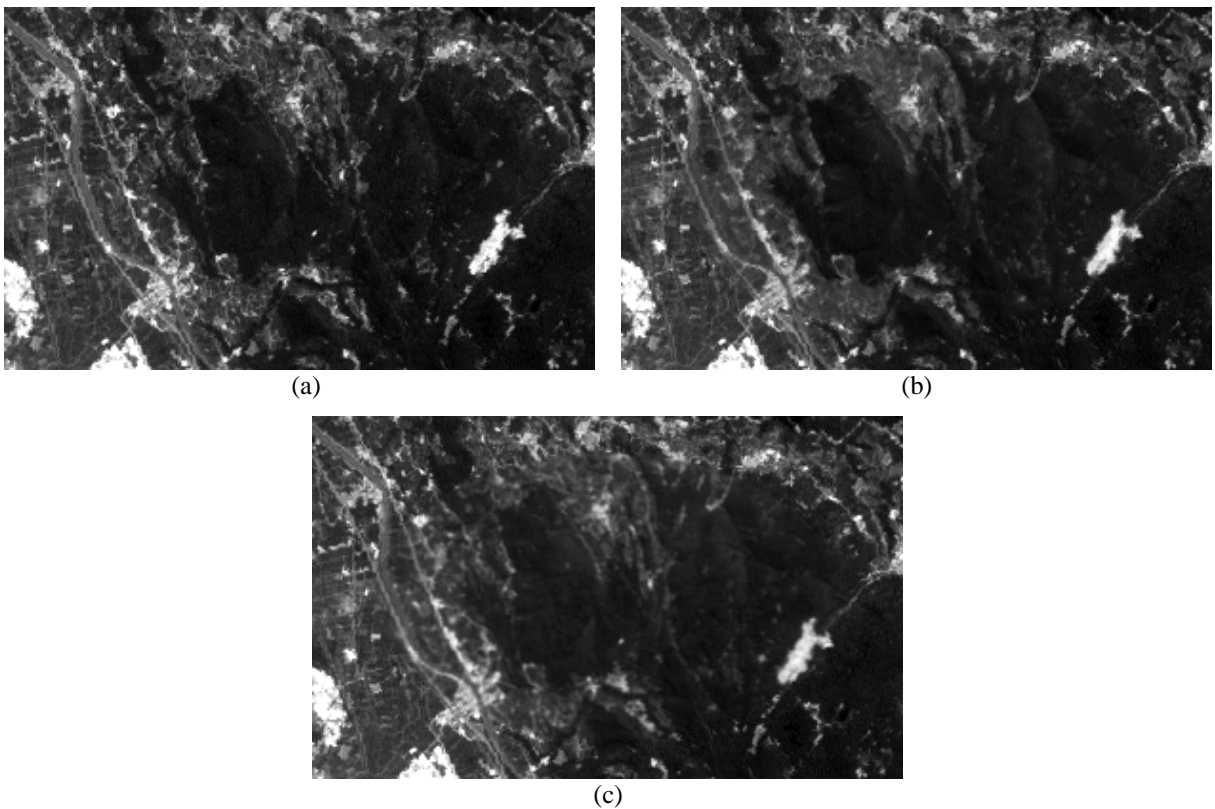


Fig.2.11: Linear multimodal prediction reconstruction results obtained after contamination with the largest simulated cloud  $C_D$  of channel 3 of the July image using both spectral and spatial information sources. a) Original subimage. b) CMLP reconstructed image (MSE = 331.24). c) LMP reconstructed image (MSE = 274.39).

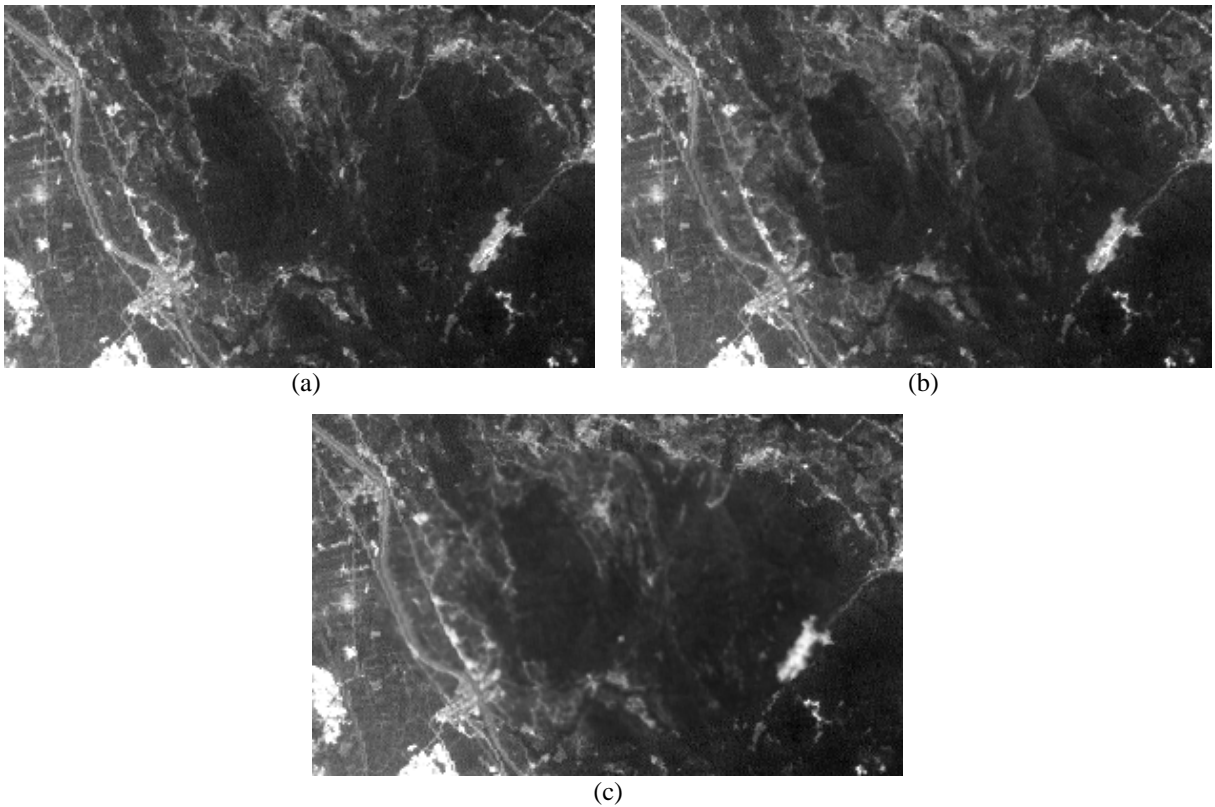


Fig.2.12: Nonlinear multimodal prediction reconstruction results obtained after contamination with the largest simulated cloud  $C_D$  of channel 1 of the July image using both spectral and spatial information sources. a) Original subimage. b) CNP reconstructed image (MSE = 252.59). c) NMP reconstructed image (MSE = 197.64).

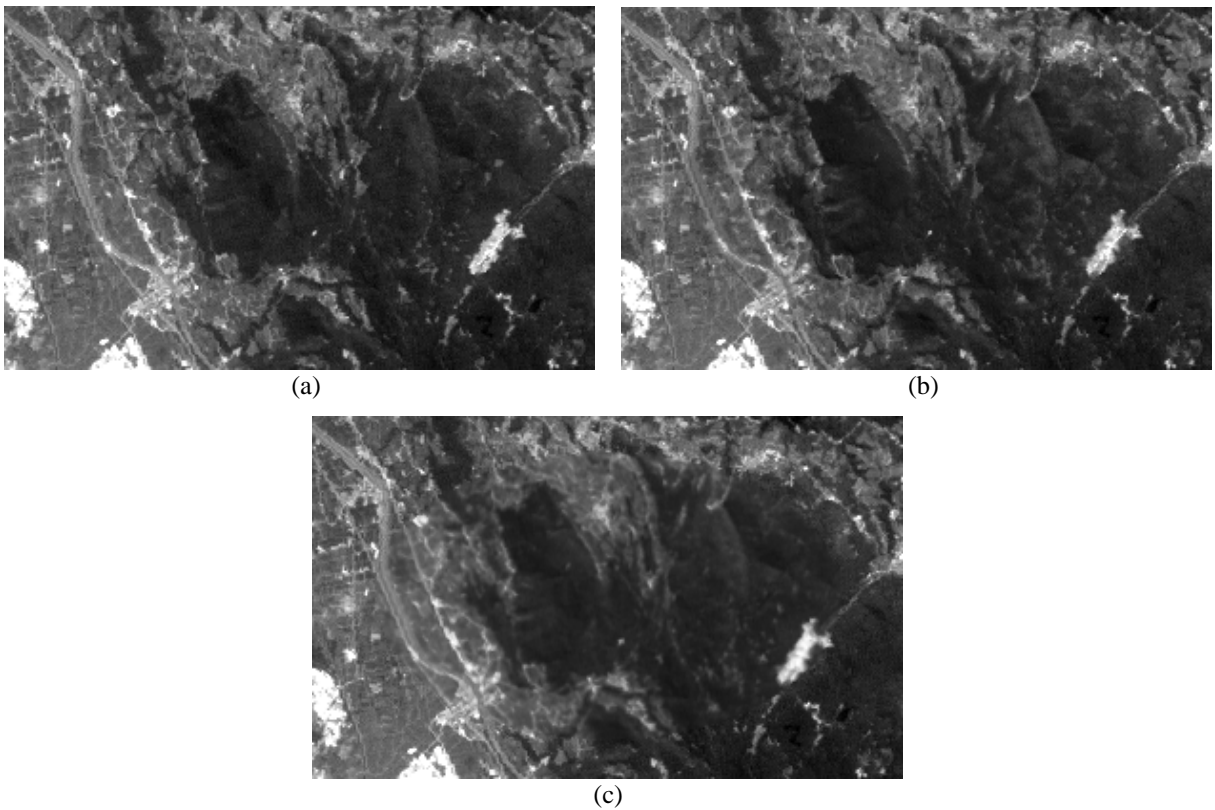


Fig.2.13: Nonlinear multimodal prediction reconstruction results obtained after contamination with the largest simulated cloud  $C_D$  of channel 2 of the July image using both spectral and spatial information sources. a) Original subimage. b) CNP reconstructed image (MSE = 289.0). c) NMP reconstructed image (MSE = 197.41).

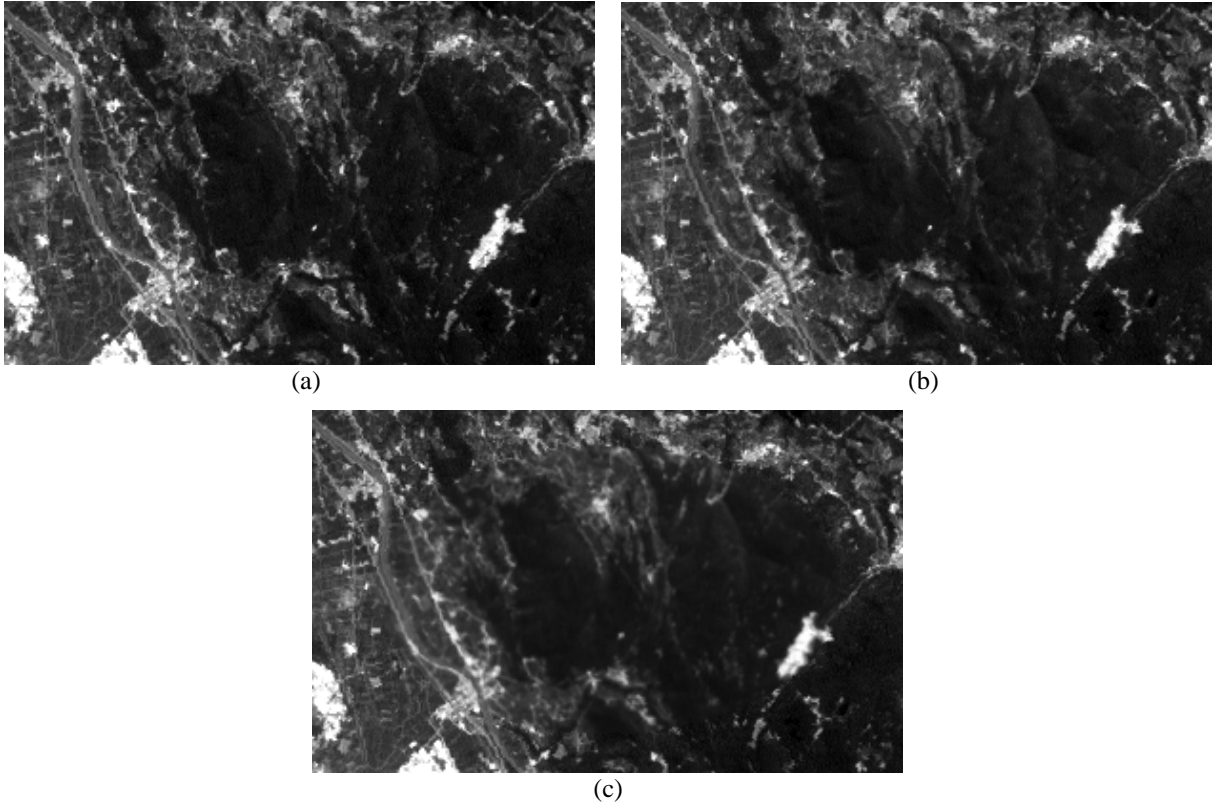


Fig.2.14: Nonlinear multimodal prediction reconstruction results obtained after contamination with the largest simulated cloud  $C_D$  of channel 3 of the July image using both spectral and spatial information sources. a) Original subimage. b) CNP reconstructed image (MSE = 341.74). c) NMP reconstructed image (MSE = 276.19).

## 2.8.4. RESIDUAL-BASED PREDICTION SIMULATIONS

### 2.8.4.1 Sequential Residual-Based Predictor Results

Table 2.3 shows the quantitative results obtained by the linear sequential residual-based predictor (LSRP) on channels 1, 2 and 3. We recall that we have applied the similar experiment tests as in the multimodal predictor, which attempt to assess for the accuracy evaluation of the method for a given image channel subject to a same cloud contamination conditions; the largest cloud cover mask  $C_D$  in our case. The obtained gains of MSE and bias are reported with respect to the CMLP method. In other words, the functional estimator used is simply the CMLP predictor. Also here, the results vary depending on the kind of used information sources. Indeed, the lowest gains in terms of MSE are those obtained when exploiting only the spectral information (0.5% for band 1, 2.0% for band 2 and 0.6% for Band 3). In comparison, the gains are considerably higher when using the spatial information (10.8% for band 13.4% for band 2 and 11.3% for Band 3). The gains in terms of bias, however, seem to be constant for both information sources (56.5% against 54.7% for band 1, 95.2% against 94.15% for band 2 and 68.03% against 66.7% for Band 3). Figs. 2.15-2.17 display an example of achieved reconstruction of channels 1, 2 and 3.

In Table 2.4, are reported the quantitative results obtained by the nonlinear sequential residual-based predictor (NSRP) on channel 2 with respect to the CNP regression method on which is based the functional estimator. As expected, the obtained gains on the MSE and bias values with the use of the spatial information are slightly higher than those obtained with the spectral information (5.7%, 32.8%) against (0.56%, 9%).

Band	Method		MSE	MSE-Gain [%]	Bias	Bias Gain [%]
1	<b>CMLP</b>		<b>238.78</b>	-	<b>1.88</b>	-
	LSRP	Spectral	237.46	0.5	0.09	95.2
		Spatial	SM1	213.06	10.8	0.11
2	<b>CMLP</b>		<b>259.2</b>	-	<b>1.7</b>	-
	LSRP	Spectral	254.05	2.0	0.74	56.5
		Spatial	SM1	224.57	13.4	0.77
3	<b>CMLP</b>		<b>331.24</b>	-	<b>1.47</b>	-
	LSRP	Spectral	329.14	0.6	0.47	68.03
		Spatial	SM1	294.72	11.03	0.49

TABLE 2.3. QUANTITATIVE RESULTS OBTAINED BY THE LSRP.

Band	Method		MSE	MSE-Gain [%]	Bias	Bias Gain [%]
2	<b>CNP</b>		<b>289.0</b>	-	<b>2.9</b>	-
	NSRP	Spectral	287.37	0.56	2.64	9.0
		Spatial	SM1	272.66	5.7	1.95

TABLE 2.4. QUANTITATIVE RESULTS OBTAINED BY THE NSRP.

#### 2.8.4.2 Parallel Residual-Based Predictor Results

Similarly, Table 2.5 shows the quantitative results obtained by the linear parallel residual-based predictor (LPRP) on channels 1, 2 and 3 for the same cloud contamination conditions. The functional estimator is based on the CMLP regression approach and the obtained gains of MSE and bias are reported with respect to this method. We note that the LPRP scheme was first applied only by exploiting the temporal data used in the CMLP process such that each contaminated pixel is estimated by the corresponding cloud-free pixels in the temporal images. The MSE gains obtained are significantly low (0.11% for band 1, 1.5% for band 2 and 0.5% for Band 3). The results are not improved any more with the incorporation of the spectral information (-0.3% for band 1, 4.9% for band 2 and 0.22% for Band 3). The gains, however, increase with the incorporation of the spatial information source and vary slowly with the use of both information sources further (11.9% against 15.5% for band 1, 13.4% against 17.3% for band 2 and 12.9% against 13.2% for Band 3). The bias gains vary proportionately to the MSE gains such that they are the lowest when using the simple temporal data and increase with the incorporation of the spectral and the spatial information respectively. Also here, the fusion of the two information sources does not provide any improvement on the gains of bias. Figs. 2.18-2.20 display an example of achieved reconstruction of channels 1, 2 and 3.

Finally, Table 2.6 shows the quantitative results obtained by the nonlinear parallel residual-based predictor (NPRP) on channel 2 for the same cloud contamination conditions. Also here, the functional estimator is based on the CMLP regression approach and the obtained gains of MSE and bias are reported with respect to this method. As for the linear model, the gain on MSE obtained is significantly low when neither the spectral information nor the spatial information is used (0.66%). The gain, however, increases slightly with the incorporation of the spatial information source (5.82%) and is significantly improved further with the use of both information sources (22.9%). The gain on bias varies proportionately to the MSE gain; it is the lowest when using the simple temporal data and increase with the incorporation of the spatial and spectral information. Unlike the linear model, the fusion of the two information sources in the NPRP appears to be the best way to get higher accuracies.

Band	Method		MSE	MSE Gain [%]	Bias	Bias Gain [%]	
1	<b>CMLP</b>		<b>238.78</b>	<b>-</b>	<b>1.88</b>	<b>-</b>	
	LPRP	temporal		238.52	0.11	0.97	48.4
		Spectral		239.56	-0.3	0.31	83.5
		Spatial	SM1	210.47	11.9	0.2	89.4
		Spatial + spectral	SM1	201.75	15.5	0.25	86.7
2	<b>CMLP</b>		<b>259.2</b>	<b>-</b>	<b>1.7</b>	<b>-</b>	
	LPRP	Temporal		255.43	1.5	1.54	9.41
		Spectral		246.49	4.9	1.85	-8.8
		Spatial	SM1	224.43	13.4	0.93	45.3
		Spatial + spectral	SM1	214.46	17.3	1.39	18.2
3	<b>CMLP</b>		<b>331.24</b>	<b>-</b>	<b>1.47</b>	<b>-</b>	
	LPRP	Temporal		329.66	0.5	1.3	11.6
		Spectral		330.50	0.22	0.84	42.9
		Spatial	SM1	288.6	12.9	0.4	72.8
		Spatial + spectral	SM1	287.47	13.2	0.69	53.06

TABLE 2.5. QUANTITATIVE RESULTS OBTAINED BY THE LPRP.

Band	Method		MSE	MSE Gain [%]	Bias	Bias Gain [%]	
2	<b>CMLP</b>		<b>259.2</b>	<b>-</b>	<b>1.7</b>	<b>-</b>	
	NPRP	Temporal		257.55	0.66	1.2	29.4
		Spatial	SM1	244.09	5.82	0.7	58.8
		Spatial + spectral	SM1	199.89	22.9	1.5	11.8

TABLE 2.6. QUANTITATIVE RESULTS OBTAINED BY THE NPRP.

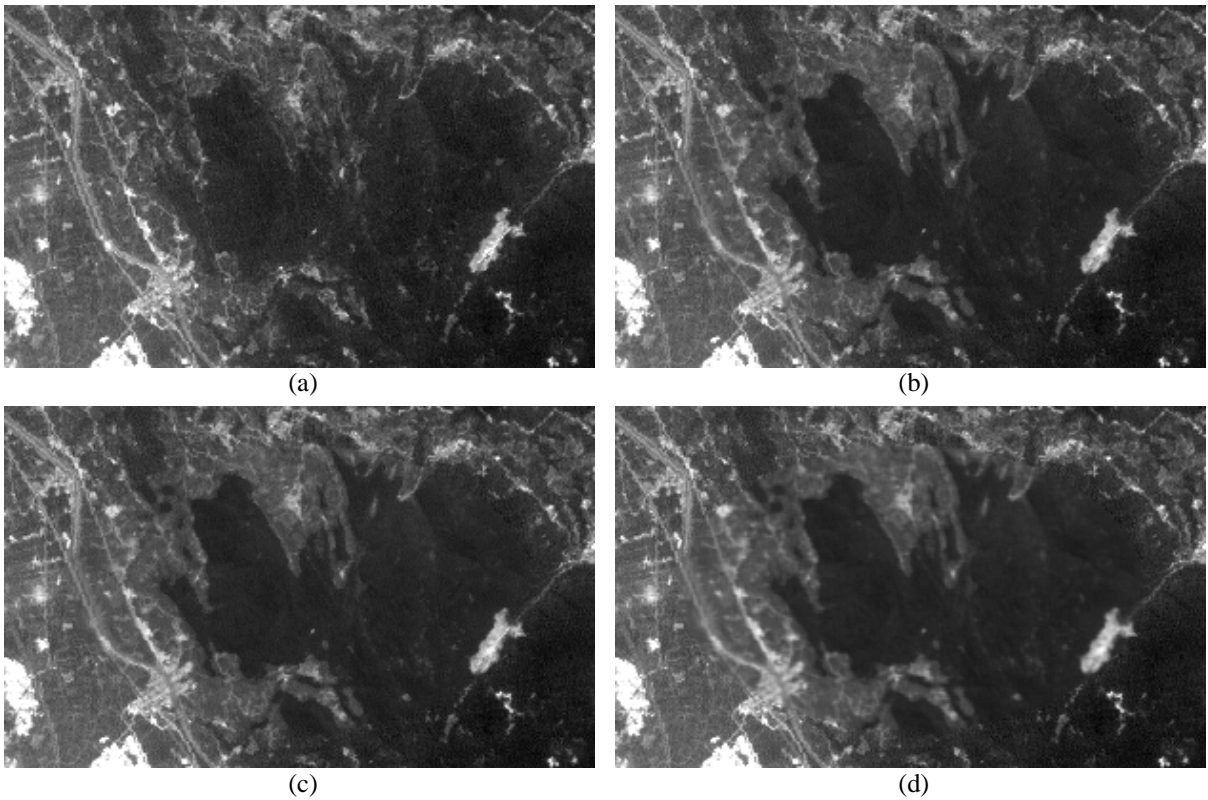


Fig.2.15: Linear sequential residual-based prediction results obtained after contamination with the largest simulated cloud  $C_D$  of channel 1 of the July image. a) Original subimage. b) CMLP reconstructed image (MSE = 238.78). c) LSRP reconstructed image using the spectral information (MSE = 237.46). d) LSRP reconstructed image using the spatial information (MSE = 213.06).

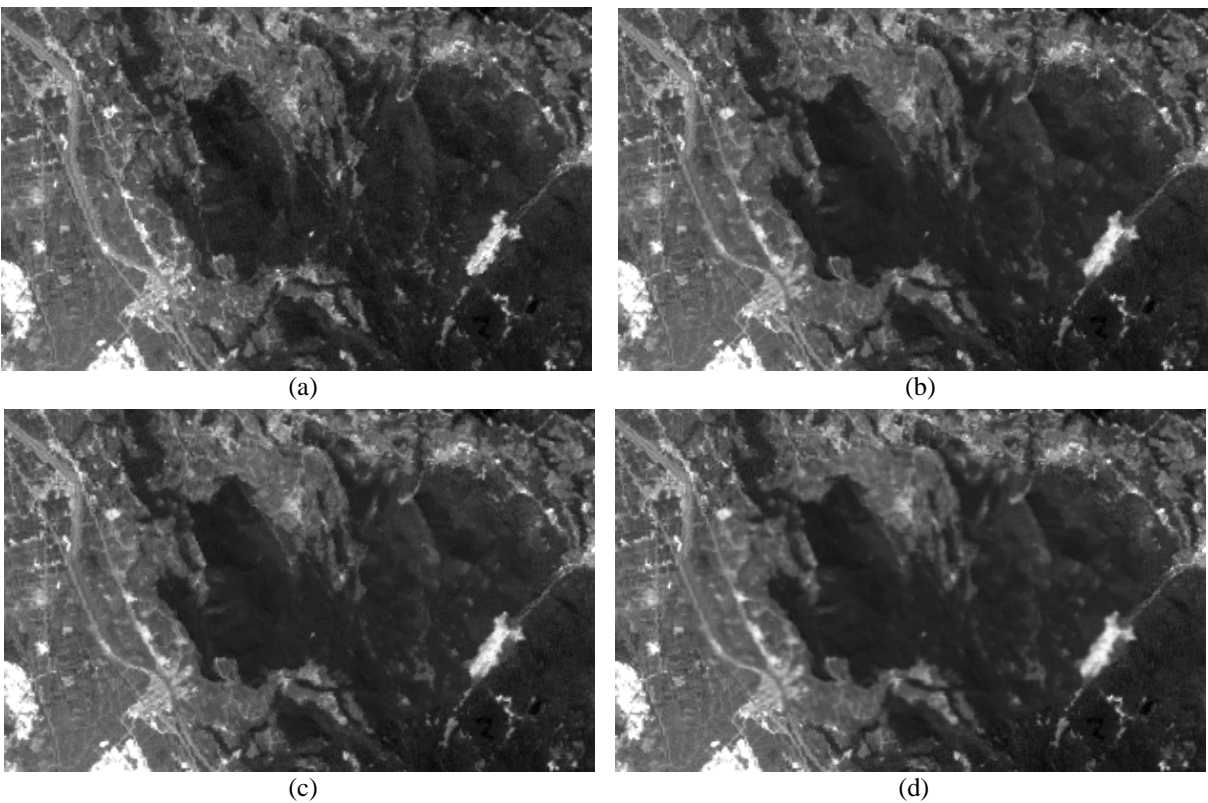


Fig.2.16: Linear sequential residual-based prediction results obtained after contamination with the largest simulated cloud  $C_D$  of channel 2 of the July image. a) Original subimage. b) CMLP reconstructed image (MSE = 259.2). c) LSRP reconstructed image using the spectral information (MSE = 254.05). d) LSRP reconstructed image using the spatial information (MSE = 224.57).

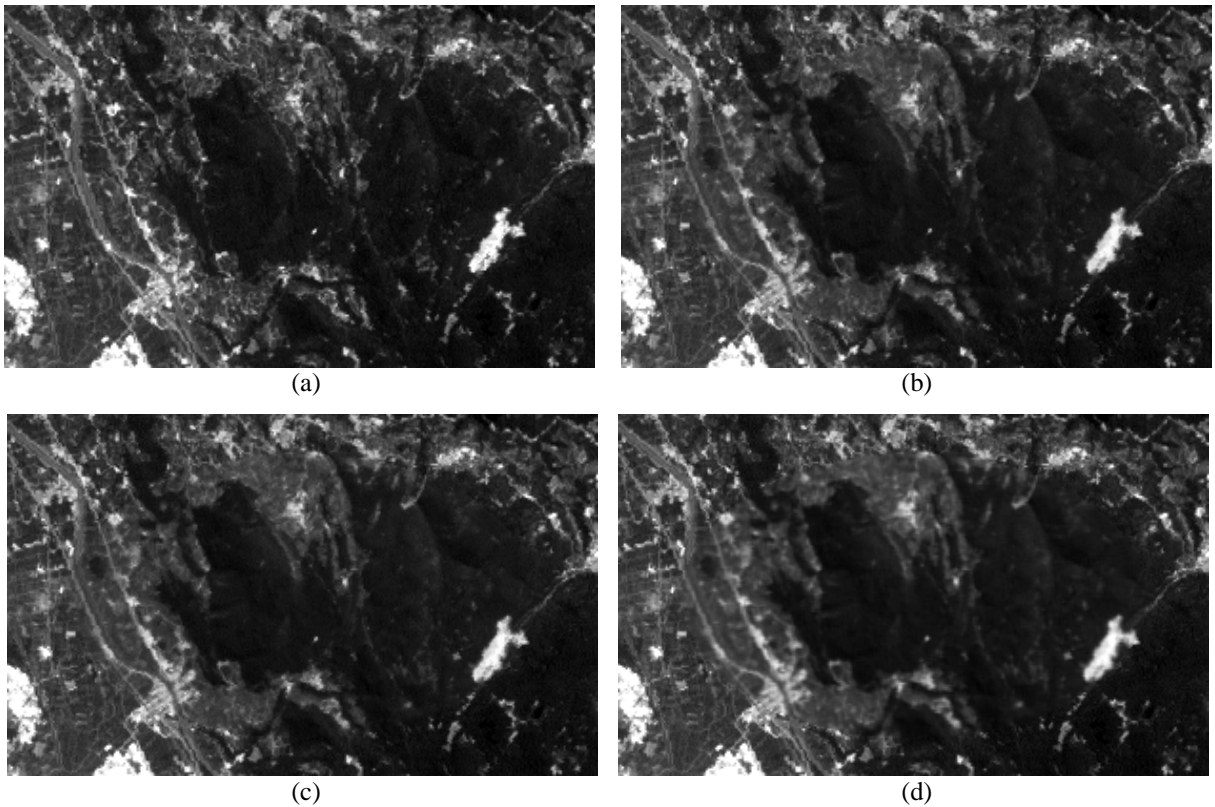


Fig.2.17: Linear sequential residual-based prediction results obtained after contamination with the largest simulated cloud  $C_D$  of channel 3 of the July image. a) Original subimage. b) CMLP reconstructed image (MSE = 331.24). c) LSRP reconstructed image using the spectral information (MSE = 329.14). d) LSRP reconstructed image using the spatial information (MSE = 294.72).

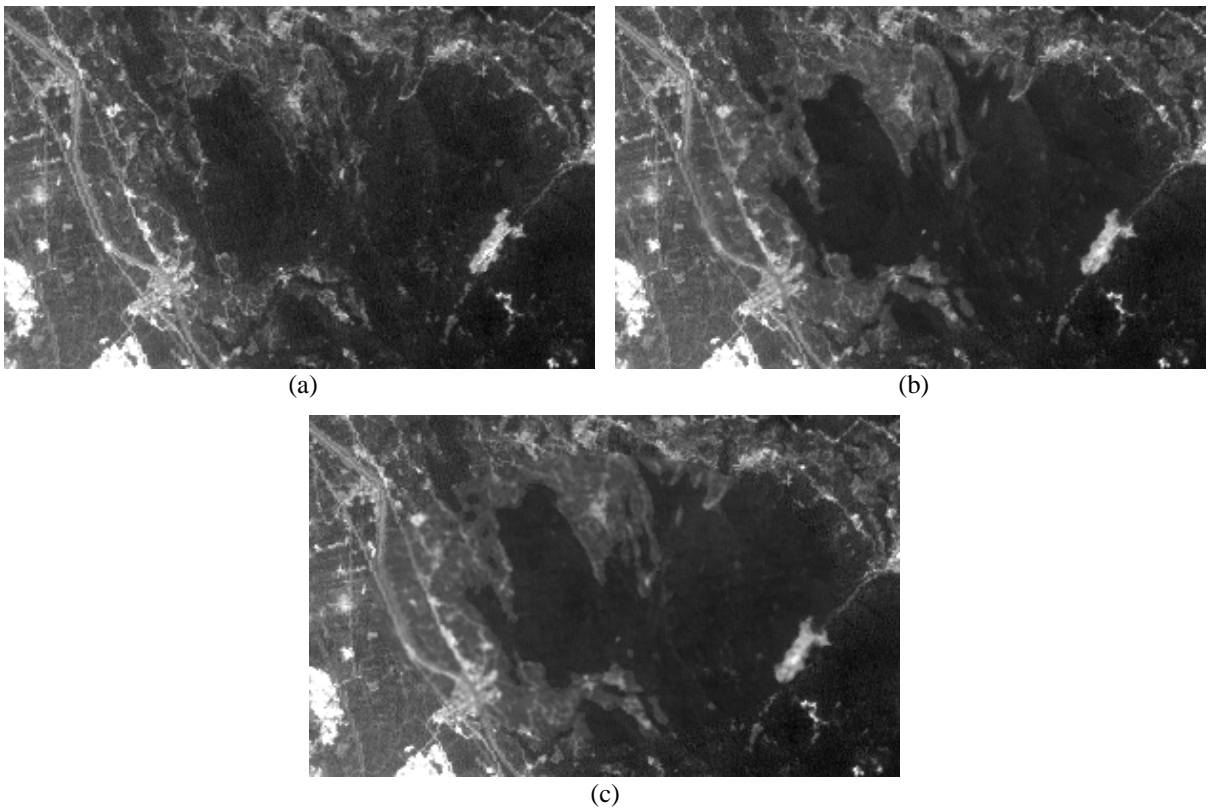


Fig.2.18: Linear parallel residual-based prediction results obtained after contamination with the largest simulated cloud  $C_D$  of channel 1 of the July image using both spectral and spatial information sources. a) Original subimage. b) CMLP reconstructed image (MSE = 238.78). c) LPRP reconstructed image (MSE = 201.75).

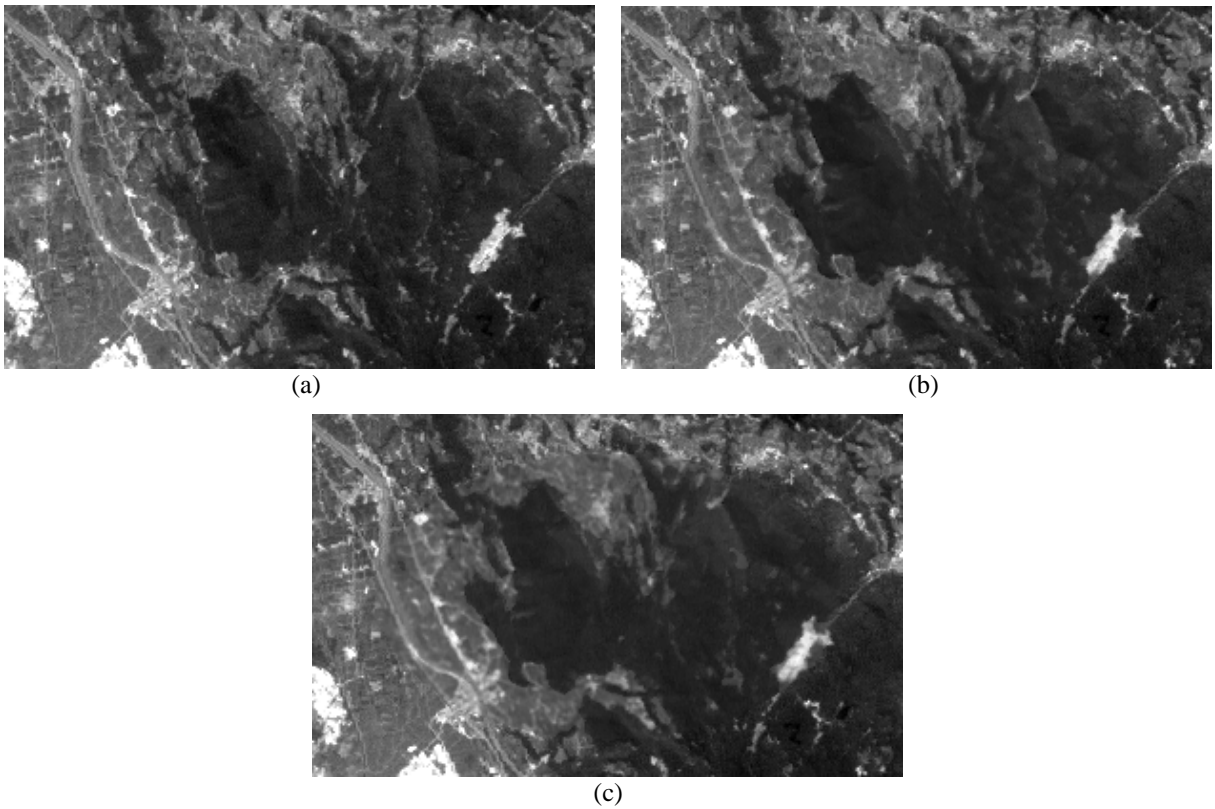


Fig.2.19: Linear parallel residual-based prediction results obtained after contamination with the largest simulated cloud  $C_D$  of channel 2 of the July image using both spectral and spatial information sources. a) Original subimage. b) CMLP reconstructed image (MSE = 259.2). c) LPRP reconstructed image (MSE = 214.46).

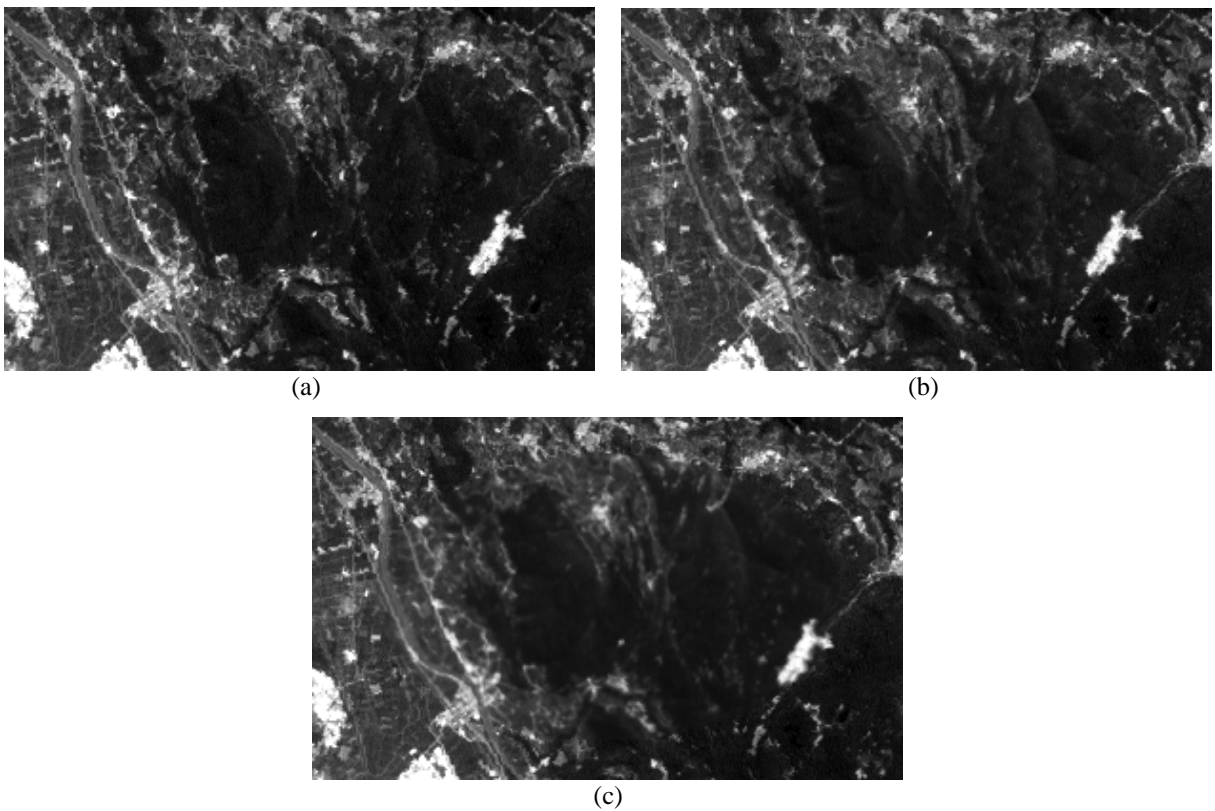


Fig.2.20: Linear parallel residual-based prediction results obtained after contamination with the largest simulated cloud  $C_D$  of channel 3 of the July image using both spectral and spatial information sources. a) Original subimage. b) CMLP reconstructed image (MSE = 331.24). c) LPRP reconstructed image (MSE = 287.47).

## 2.8.5. CSSPR SIMULATIONS

### 2.8.5.1 Sensitivity to Cloud-Contamination Conditions

Unlike the previous methods, the CSSPR process attempts, in a first step, to assess the post-reconstruction quality for a given image channel subject to different cloud contamination conditions that have been carried out by adopting the groups of masks ( $C_{1,2,3,4}$ ) and ( $C_{A,B,C,D}$ ) displayed in Fig.2.7. For each mask we ran the proposed approach starting from the reconstruction results achieved with the CMLP method.

Table 2.7.a shows the quantitative results obtained on channel 2 and averaged over the eight masks. In particular, we report the averaged gains of MSE and bias with respect to the CMLP method. In general, as can be seen, the results vary from one source of information to another and from one spatial model to another. In more detail the lowest gains in terms of MSE and bias are those obtained when exploiting only the spatial information. For this information source, the best spatial model appears to be SM1 with gains of MSE and bias of 5.7% and 3.1%, respectively. The gains are higher when adopting all available spectral information (8.1% and 44.9%, respectively). The fusion of both information sources allows improving the post-reconstruction results further. In particular when SM1 is adopted, the averaged gains of MSE and bias reach values of 9.8% and 37.7%, respectively.

The assessment of the post-reconstruction quality was also evaluated in terms of preservation capability of the information content for classification purposes. To do so, a classification map was first generated by means of the EM-based classifier [151] for the original cloud-free July image to serve as reference classification map. For each post-reconstruction simulation, the impact on the classification process was assessed by comparing, inside and outside the contaminated area, the classification map produced from the post-reconstructed image with the reference classification map. The differences between the overall errors achieved by the CMLP and the CSSPR methods inside and outside the contaminated area (OE-C and OE-U, respectively) are listed in Table 2.7.a. We recall that the reported numbers are averaged over the eight masks. This quality criterion confirms that the best improvements are achieved by exploiting both spatial and spectral information sources.

### 2.8.5.2 Multichannel Post-Reconstruction

As mentioned above, this experiment was aimed at evaluating the post-reconstruction performances over all channels of the image for a given cloud-contamination simulation that is the largest cloud cover mask  $C_D$ . As in the first set of experiments, the different CSSPR variants were applied to reconstruct each of the six available image channels (i.e., channels 1-5 and 7). Concerning the impact on the classification process, note that this time we adopted the standard k-means classification algorithm for a simultaneous classification of all post-reconstructed channels. The obtained results in terms of MSE and bias averaged over the six channels and the classification error rates (OE-C and OE-U) are reported in Table 2.7.b. They all confirm the benefit of the post-reconstruction process in improving reconstruction quality. An illustration of reconstructed images for channel 4, for which very significant improvements were obtained, is given in Fig. 2.21. In Fig. 2.22 we illustrate a color composite image for the reconstructed bands 4, 3, and 2. A visual inspection of the resulting image confirms the usefulness of the PCSSR process to enhance the reconstruction quality. In Fig. 2.23, we illustrate the plotting graphs of the original channel 4 subimage pixels inside the contaminated area against the corresponding pixels in the reconstructed images with the CMLP method and the different CSSPR variants. In Fig. 2.24, we represent the multiband classification maps obtained by the K-means algorithm with three data classes.

### 2.8.5.3 Error Map Generation

As an example of error map generation, we still shall consider the post-reconstruction simulation with the largest cloud cover mask  $C_D$ . In particular, we shall start from the results provided by the CSSPR process implemented with both spectral and spatial information sources. For the latter, we adopted the SM1 model as it appears to perform best.

As described above, we first post-reconstructed the July image outside  $C_D$ . Then by comparing the post-predicted and the cloud-free images, we generated a contextual error map (outside  $C_D$ ) for each channel and afterwards a single contextual  $L_2$ -norm error map. Next we trained an SVM predictor 1) in order to model the relationship between the post-reconstructed image channels and the contextual  $L_2$ -norm errors (outside  $C_D$ ); and thus 2) to estimate errors inside the contaminated area ( $C_D$ ). The obtained error map is shown in Fig. 2.25 together with the true error map. The correlation coefficient between the two maps is equal to 0.53, indicating that a moderate but useful prediction capability was inferred from the context (i.e., outside  $C_D$ ). Indeed, though the obtained map cannot be used to know the exact error value for each post-reconstructed pixel, it allows identifying satisfactorily the areas with low, medium and high error content.

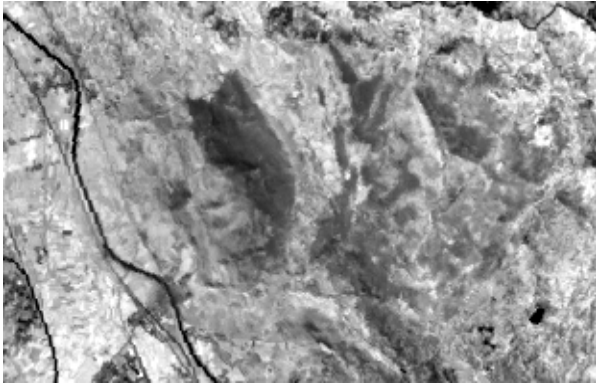
Method		MSE Gain [%]	Bias Gain [%]	OE-C [%]	OE-U [%]	
CSSPR	Spectral (M1)	8.1	44.9	0.9	0.3	
	Spatial	SM1 (M2)	5.7	3.1	0.2	-0.5
		SM2 (M3)	3.8	-25.5	0.0	-0.4
		SM3 (M4)	3.8	-3.9	0.2	-0.2
	Spatial + Spectral	SM1 (M5)	9.8	37.7	1.0	0.2
		SM2 (M6)	9.2	22.8	0.9	0.1
		SM3 (M7)	9.2	50.4	1.0	0.2

(a)

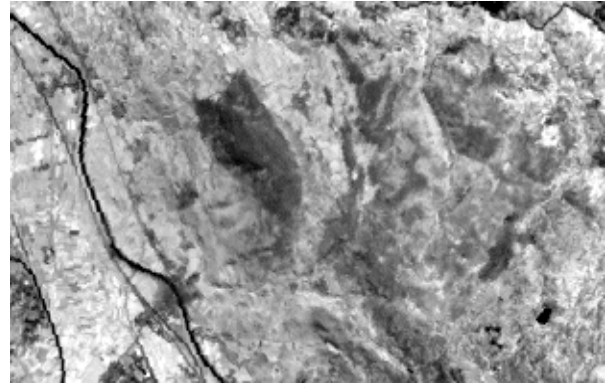
Method		MSE	MSE Gain [%]	Bias	Bias Gain [%]	OE-C [%]	OE-U [%]	
CMLP		451.8	-	1.7	-	11.1	1.8	
CSSPR	Spectral (M1)	408.5	9.6	0.5	70.8	10.4	2.4	
	Spatial	SM1 (M2)	389.0	13.9	1.0	43.5	10.4	1.1
		SM2 (M3)	414.8	8.2	1.0	39.9	10.9	1.1
		SM3 (M4)	414.0	8.4	0.9	49.4	10.8	0.9
	Spatial + Spectral	SM1 (M5)	368.9	18.3	0.5	72.0	9.5	1.5
		SM2 (M6)	390.0	13.7	0.9	48.8	10.3	1.9
		SM3 (M7)	385.6	14.6	0.5	70.2	10.1	2.4

(b)

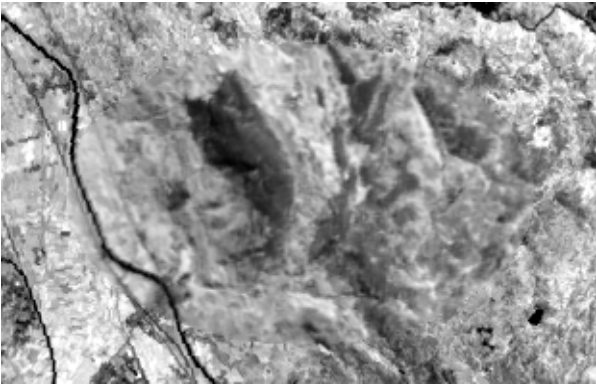
TABLE 2.7. QUANTITATIVE RESULTS OBTAINED BY THE CSSPR METHOD FOR (a) THE FIRST AND (b) THE SECOND SIMULATION EXPERIMENTS



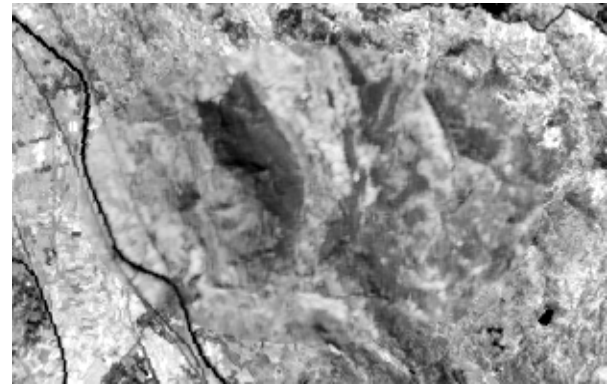
(a)



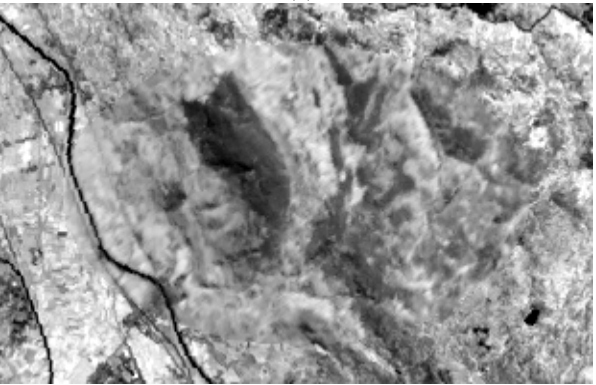
(b)



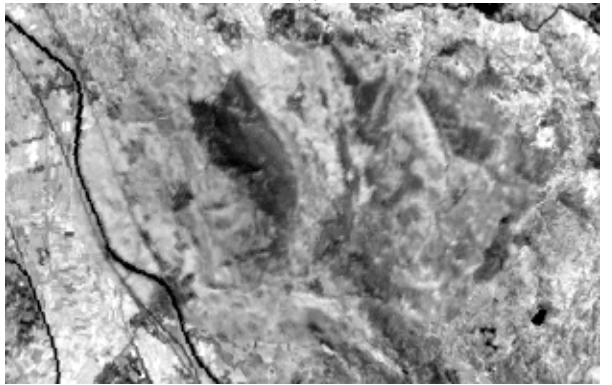
(c)



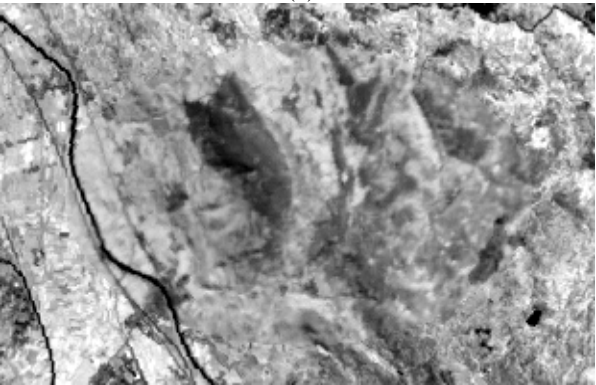
(d)



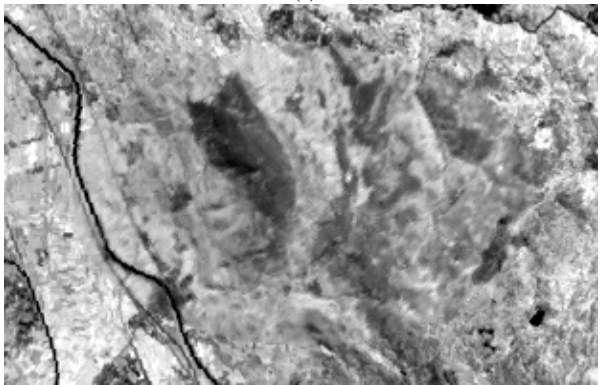
(e)



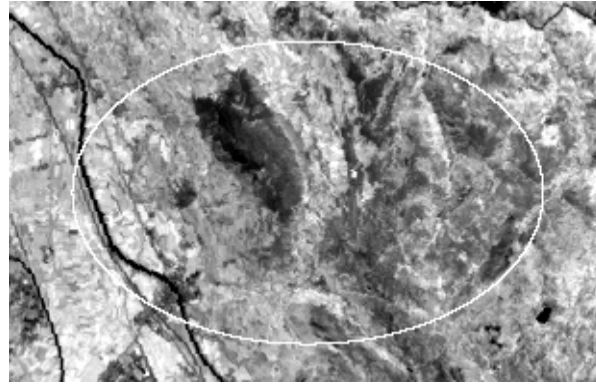
(f)



(g)

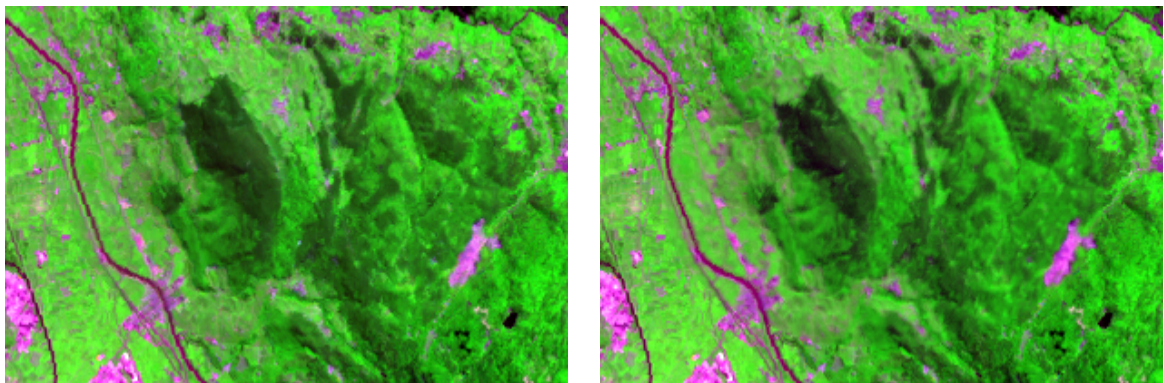


(h)



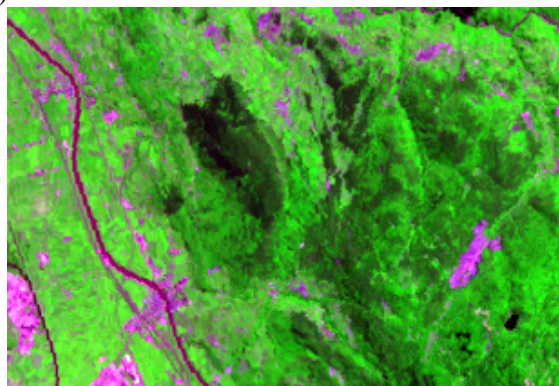
(i)

Fig.2.21: Reconstruction results obtained after contamination with the largest simulated cloud  $C_D$  (which covers 48.6% of the entire image) of channel 4 of the July image by (a) the CMLP method (MSE=790.7), (b) the CSSPR (M1) (MSE=669.6), (c) the CSSPR (M2) (MSE=674.44), (d) the CSSPR (M3) (MSE=739.33), (e) the CSSPR (M4) (MSE=739.44), (f) the CSSPR (M5) (MSE=612.8), (g) the CSSPR (M6) (MSE=653.55) and (h) the CSSPR (M7) (MSE=638.73) compared to (i) the original cloud-free image. The white marker in (i) shows the area that has been completely obscured by cloud  $C_D$  before reconstruction (i.e., all data within the marker were assumed to be missing).



(a)

(b)



(c)

Fig.2.22: Color composite (bands 4, 3 and 2) of the July subimage by (a) the CMLP method, (b) the CSSPR (M5) compared to (c) the original cloud-free image.

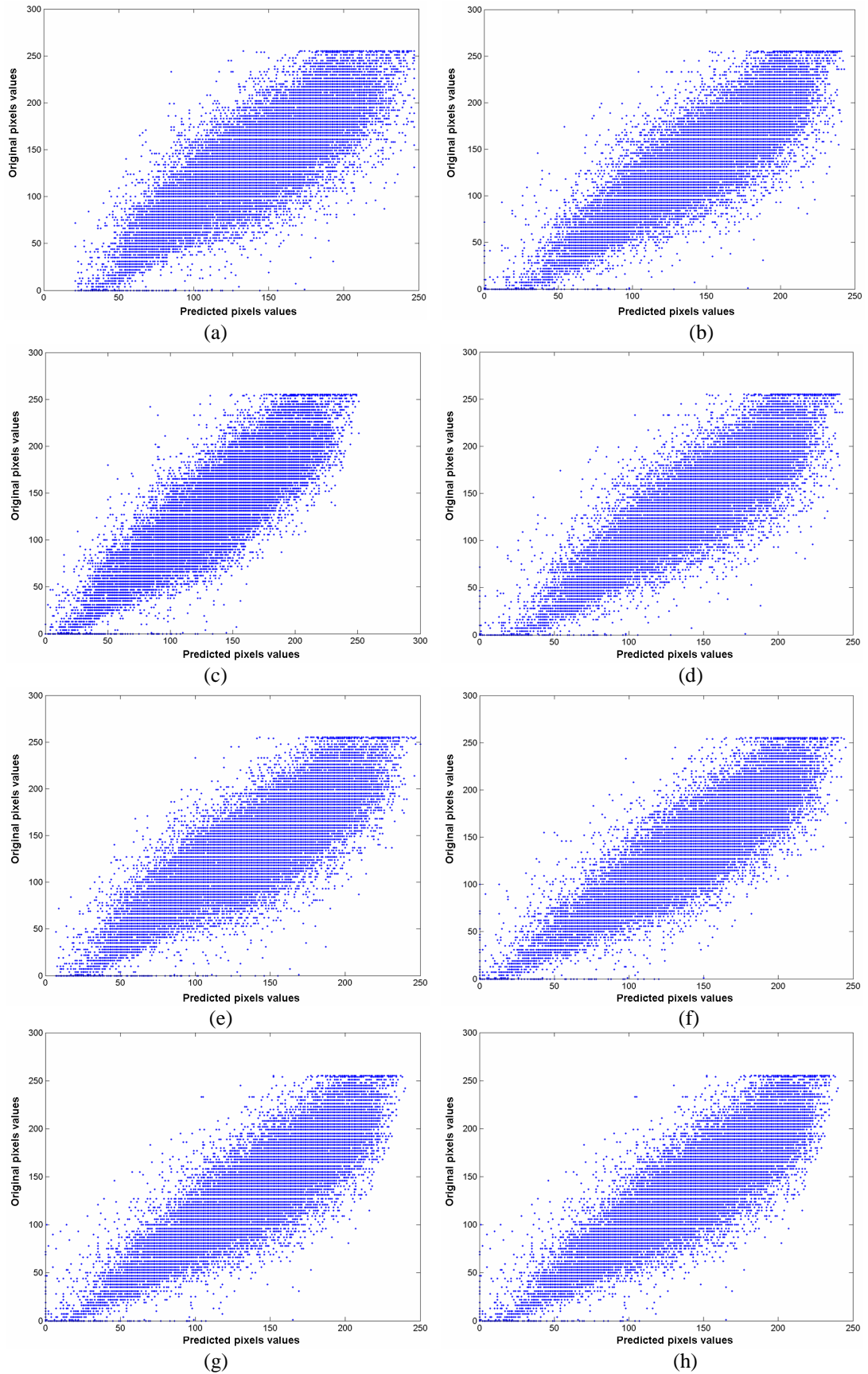


Fig.2.23: Plotting graphs of the original channel 4 subimage pixels inside the contaminated area against the corresponding pixels in the reconstructed images by (a) CMLP method, (b) CSSPR M1, (c) CSSPR M2, (d) CSSPR M3, (e) CSSPR M4, (f) CSSPR M5, (g) CSSPR M6, (h) CSSPR M7.

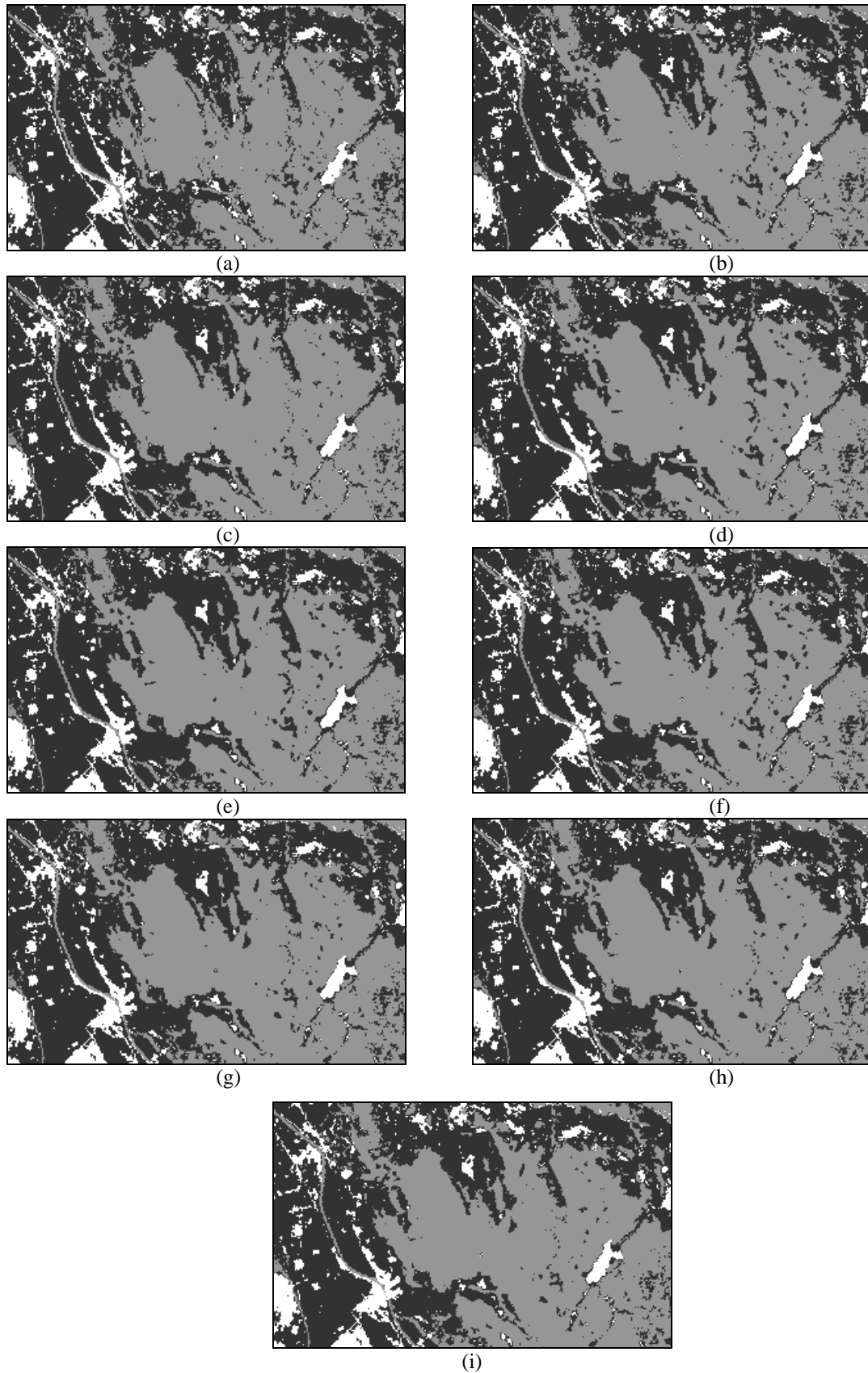


Fig.2.24: Multichannel classification maps obtained by the K-means algorithm with three data classes. (a) for the original multichannel July subimages and the same subimages reconstructed with the largest simulated cloud  $C_D$  by (b) CMLP method, (c) CSSPR (M1), (d) CSSPR (M2), (e) CSSPR (M3), (f) CSSPR (M4), (g) CSSPR (M5), (h) CSSPR (M6), (i) CSSPR (M7).

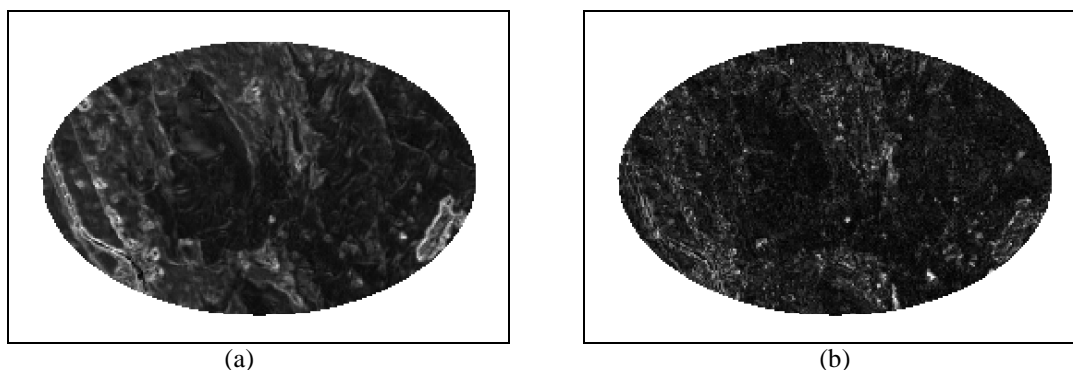


Fig.2.25: Reconstruction  $L_2$ -norm error maps associated with the CSSPR process applied to all channels of the July image after contamination with cloud  $C_D$ : (a) map estimated with the proposed procedure and (b) map representing the true value of the committed errors.

## 2.9. SUMMARY

Three methods have been proposed for use in the post-reconstruction of cloud contaminated areas from remote sensing images. The first method uses a multimodal prediction, the second is based on the exploitation of the residuals generated by an estimator for further improvements, and the last method consists in a contextual spatio-spectral post-reconstruction scheme (CSSPR). In all the methods, we have investigated the suitability of incorporating spatial and spectral information sources. In particular, the first two methods consider solely the common second order spatial neighborhood system, while three different spatial models were investigated in the CSSPR method.

In general, post-reconstruction is useful to boost the reconstruction quality depending on the contamination scenario, either the spectral or the spatial information may appear more valuable. However their fusion is the best way to get higher accuracies.

# Chapter 3

## HISTOGRAM MODIFICATION

### 3.1. INTRODUCTION

Images captured in an excessively dark or bright environment are less contrasted. As a consequence, the image is inappropriate for visual inspection or simple observation. The aim of image enhancement is to improve the interpretability or perception of information in images for human viewers, or to provide *better* input for other automated image processing techniques [1],[7],[278].

We note that there is no general theory of image enhancement. When an image is processed for visual interpretation, the viewer is the ultimate judge of how well a particular method works. Visual evaluation of image quality is a highly subjective process, thus making the definition of a *good image* an elusive standard by which to compare algorithm performance. However, when image enhancement techniques are used as pre-processing tools for other image processing techniques, then quantitative measures can determine which techniques are most appropriate.

Image enhancement approaches fall into two broad categories: 1) spatial domain methods, which operate directly on pixels, and 2) frequency domain methods, which operate on the Fourier transform and more recently on the wavelet transform of an image. Enhancement techniques based on various combinations of methods from these two categories exist as well.

Histogram modification for contrast enhancement in the spatial domain is the topic for the remaining sections. In particular, a technique which is based upon a mapping of the grey levels to achieve a uniform distribution is considered, that is histogram equalization.

## 3.2. HISTOGRAM MODIFICATION

### 3.2.1. CONTRAST OF AN IMAGE

Contrast generally refers to a difference in luminance or grey level values in some particular region of an image  $\mathbf{X}$ . For any given imaging system, only a finite luminance or optical density range will be available. If we assume that the values of  $X(i,j)$  correspond to luminance values at the point  $(i,j)$ , then  $X(i,j)$  would have a finite maximum and minimum, ie,  $[m,M]$ , and large values of  $X(i,j)$  will correspond to bright points.

The difference between the maximum and the minimum values of  $X(i,j)$  is called the *contrast range* and is an important parameter for any imaging system. The ratio of the maximum to the minimum values is called the *contrast ratio* and is also a commonly used parameter.

### 3.2.2. IMAGE TRANSFORMATION

We may alter the grey level values and thus change the contrast of the information in an image by effecting a linear or non linear transformation, i.e., by forming a new image function  $Y(i,j)$  for each  $(i,j)$ . In the spatial domain such a function may be expressed as:

$$Y(i, j) = T[X(i, j)] \quad (3.1)$$

where  $X(i,j)$  is the input image,  $Y(i,j)$  is the processed image, and  $T$  is an operator (some mapping) on  $\mathbf{X}$  defined over some neighborhood of  $(i,j)$ .

The simplest form of  $T$  is when the neighborhood is  $1 \times 1$ . In this case,  $\mathbf{Y}$  depends only on the value of  $\mathbf{X}$  at  $(i,j)$ , and  $T$  becomes a grey-level transformation function of the form:

$$s = T(r) \quad (3.2)$$

where  $r$  and  $s$  are variables denoting the grey level of  $X(i,j)$  and  $Y(i,j)$  at any point  $(i,j)$ . Because enhancement at any point in an image depends only on the grey level at that point, techniques in this category often are referred to as point processing.

Larger neighborhoods allow a variety of processing functions that go beyond just image enhancement. Some grey scale transformations are outlined in Fig. 3.1.

### 3.2.3. HISTOGRAM PROCESSING

For a given image  $\mathbf{X}$  with grey levels in the range  $[0, L - 1]$ , the histogram of the image represents the number of pixels that have a specific intensity  $X_k$ . It is associated with the probability density function defined as:

$$p(x_k) = \frac{n_k}{n} \quad k = 0, 1, \dots, L-1 \quad (3.3)$$

where  $n_k$  represents the number of times that the level  $X_k$  appears in the image  $\mathbf{X}$  and  $n$  is the total number of samples in the image.  $p(X_k)$  gives an estimate of the probability of occurrence of grey level  $X_k$ . A plot of this function for all  $k$  or  $n_k$  vs  $X_k$  provides a global description of the appearance of an image. Although it says nothing specific about image content, the shape of the histogram of an image does give useful information about the possibility for contrast enhancement (Fig. 3.2).

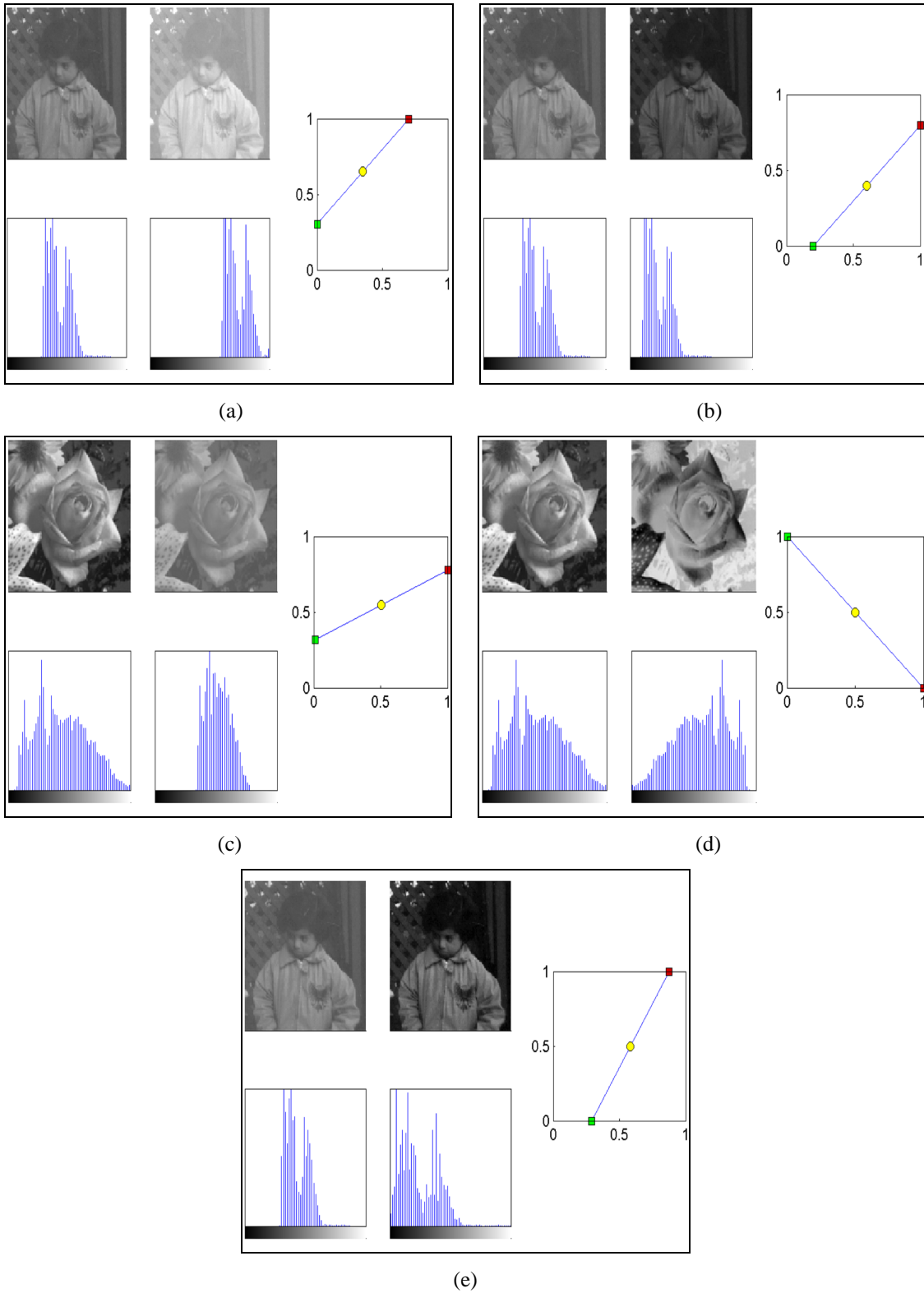


Fig. 3.1 [279]: Examples of some point processing transformations. (a) Image lighting. (b) Image darkening. (c) Compression of dynamic range. (d) Image inversion. (e) Contrast stretching.

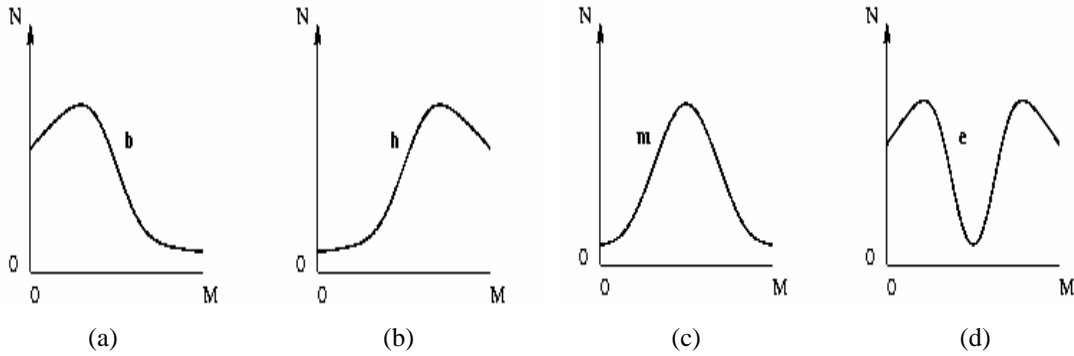


Fig. 3.2 [279]: Histograms corresponding to four basic image types. (a) Dark image. (b) Bright image. (c) Low-contrast image. (d) Low shading between shadows and lights.

### 3.2.3.1. Histogram Equalization (HE)

For many classes of images, the *ideal* distribution of grey levels is a perfectly flat histogram which makes use of every available grey value in the image format and tends to enhance low-contrast information. The following steps show us how to obtain a uniform distribution with a grey level transformation [1],[7],[278]:

1. Compute the histogram of the image grey level values,
2. Add up the histogram values to obtain a distribution curve, and
3. Use this distribution curve for the grey level transformation  $s = T(r)$ .

Given an image  $\mathbf{X}$  with grey levels in the range  $[0, L - 1]$ , the transformation function  $T(r)$  is essentially the cumulative density function defined by:

$$Y_k = c(x) = \sum_{j=0}^k p(X_j) = \sum_{j=0}^k \frac{n_j}{n} \quad (3.4)$$

where  $X_k = x$ , for  $k = 0, 1, \dots, L-1$ . Note that  $c(X_{L-1}) = 1$ , by definition. *HE* is the scheme that maps the input image into the entire dynamic range,  $(X_0, X_{L-1})$  by using the cumulative density function as a transform function. If we define a transform function  $f(x)$  based on the cumulative density function such as:

$$f(x) = X_0 + (X_{L-1} - X_0)c(x) \quad (3.5)$$

Then the output image of the *HE*,  $\mathbf{Y} = \{Y(i, j)\}$  can be expressed as.

$$\begin{aligned} \mathbf{Y} &= f(\mathbf{X}) \\ &= \{f(\mathbf{X}(i, j), \forall \mathbf{X}(i, j) \in \mathbf{X})\} \end{aligned} \quad (3.6)$$

A numerical example is given in Table 3.1 to illustrate the computational procedure for histogram equalization of the image shown in Fig. 3.3a.

*HE* flattens a histogram. Based on information theory, entropy of a message source will get the maximum value when the message has uniform distribution property. In spite of its high performance in enhancing contrasts of a given image, however, the straight use of *HE* may introduce a significant change in the original brightness of an input image.

0	0	0	1	2
2	3	0	1	1
3	3	5	0	1
7	6	7	1	2
7	7	7	0	0
5	6	0	0	0

2	2	2	3	4
4	5	2	3	3
5	5	5	2	3
7	6	7	3	4
7	7	7	2	2
5	6	2	2	2

(a) (b)  
 Fig. 3.3: Histogram equalization example. (a) Original image having 8 grey levels.  
 (b) Histogram equalized image.

<i>I</i>	$x_j = 1/7$	$n_j$	$p(x_j) = p(I)$	$y_j = c(x_j)$	<i>J</i>
0	0.000	10	0.333	0.333	2
1	0.143	5	0.167	0.500	3
2	0.286	3	0.100	0.600	4
3	0.429	3	0.100	0.700	5
4	0.571	0	0.000	0.700	5
5	0.714	2	0.067	0.767	5
6	0.857	2	0.067	0.834	6
7	1.000	5	0.167	1.000	7

TABLE 3.1. HISTOGRAM EQUALIZATION PROCEDURE. C1: ORIGINAL GREY LEVEL VALUES. C2: SCALED VALUES. C3: NUMBER OF OCCURRENCES. C4: RELATIVE FREQUENCIES. C5: DISTRIBUTION FUNCTION. C6: SCALED OUTPUT GREY LEVELS.

Suppose that the input image  $\mathbf{X}$  is a continuous random variable, ie.  $L = \infty$ , then the output of the HE,  $\mathbf{Y}$  is also regarded as a random variable. HE produces an image whose grey levels have a uniform density, that is:

$$p(x) = 1/(X_{L-1} - X_0) \tag{3.7}$$

for  $X_0 \leq x \leq X_{L-1}$ . Thus the mean brightness of the output image of the HE is:

$$\begin{aligned}
 E(\mathbf{Y}) &= \int_{X_0}^{X_{L-1}} x p(x) dx \\
 &= \int_{X_0}^{X_{L-1}} \frac{x}{X_{L-1} - X_0} dx \\
 &= \frac{X_{L-1} + X_0}{2}
 \end{aligned} \tag{3.8}$$

where  $E(\cdot)$  denotes a statistical expectation. Clearly, the output mean of the HE is always the middle grey level regardless of the input mean.

Some pictorial examples of HE are outlined in Fig. 3.4.

### 3.2.3.2. Histogram Specification

Sometimes, it is desirable to specify particular histogram shapes capable of highlighting certain grey-level ranges in an image. This can be achieved by using a powerful scheme called histogram specification (HS). The procedure can be summarized as follows [1],[7],[278]:

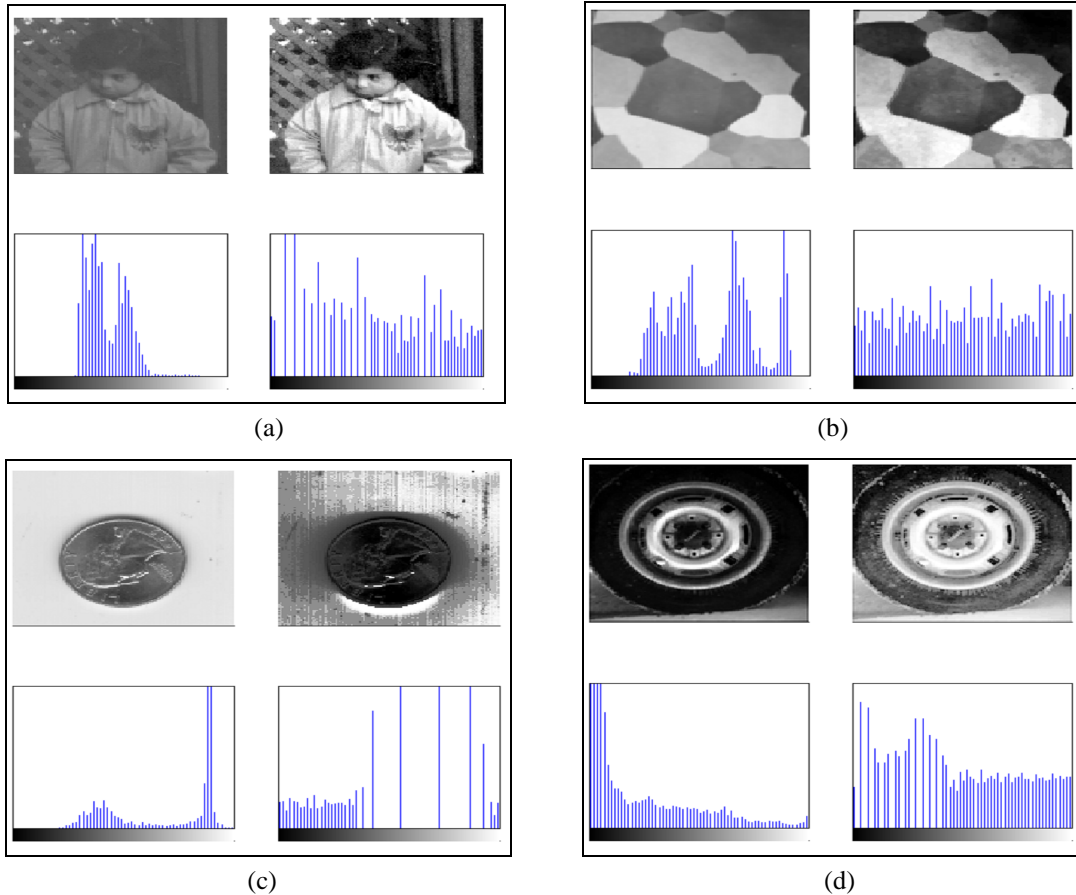


Fig. 3.4 [279]: Illustration of some histogram equalization examples. (a) Contrast enhancement. (b) Modes suppression. (c) Image degradation. (d) Details highlighting.

1. Histogram-equalize the original image  $\mathbf{X}$  ( $s = T(x)$ ), using Eq. (3.4).
2. Specify the desired density function  $p_y(y)$ , (corresponding to the desired image  $\mathbf{Y}$ ) and obtain the equalizing transformation  $v = U(y)$ .
3. Apply the inverse transformation  $y = U^{-1}(s)$  to the previously equalized image  $s$  obtained in step (1).

Step 3 is justified by the following assumption: the inverse process,  $y = U^{-1}(v)$ , would give back the levels,  $y$ , of the desired image. This formulation is hypothetical because the  $y$  levels are precisely what is being sought. However,  $p_s(s)$  and  $p_v(v)$  would be identical uniform densities. Thus, we use the uniform levels  $s$ , obtained from the original image, instead of using  $v$  in the inverse process  $U^{-1}$ . The resulting levels  $y = U^{-1}(s)$  would have the desired probability density function  $p_y(y)$ .

The above three steps process may be compressed into a simple but powerful enhancement procedure by combining the transformations

$$y = U^{-1}[T(x)] \quad (3.9)$$

### 3.3. QUALITY MEASURES

As stated before, when image enhancement methods are used as pre-processing tools for other image processing techniques, then quantitative measures can determine which techniques are most appropriate. In the following, we will define three different quality measures.

#### 3.3.1. ABSOLUTE MEAN BRIGHTNESS ERROR

The brightness preservation is based on an objective measurement referred as Absolute Mean Brightness Error (*AMBE*) [280]. It is defined as the absolute difference between the input and the output mean as follows:

$$AMBE = |E(X) - E(Y)| \quad (3.10)$$

Lower *AMBE* implies better brightness preservation.

#### 3.3.2. CONTRAST-PER-PIXEL

We define contrast-per-pixel *C* of an image as the average difference in grey level between adjacent pixels [281]:

$$C = \frac{\sum_{i=0}^N \sum_{j=0}^M (\sum_{(m,n) \in V(i,j)} |X(i,j) - X(m,n)|)}{MN} \quad (3.11)$$

#### 3.3.3. IMAGE DISTORTION

To measure the dissimilarity or distortion of the structure between two images with grey functions  $g_1$  and  $g_2$  defined over  $[0, L-1] \times [0, L-1]$ , we compute the standard deviation of the ratios of pixel grey levels pairwise in  $g_1$  and  $g_2$  [281]. This measure can be thought of as the standard deviation of local change in contrast. Formally, it is defined as:

$$\delta = \frac{1}{M \cdot N} \sum_{i,j} \left( \frac{g_1(i,j)}{g_2(i,j)} - \mu_{ij} \right)^2 \quad (3.12)$$

where the quantity  $\mu_{ij} = \frac{1}{M \cdot N} \sum_{i,j} \frac{g_1(i,j)}{g_2(i,j)}$  is the mean ratio. If  $g_2(i,j) = 0$ , then pixel  $(i,j)$  is excluded from the sums.

### 3.4. LITTERATURE SURVEY

Enhancing the contrast of images is one of the major issues in image processing. Contrast enhancement techniques are encountered in many applications including medical image processing, radar image processing, remote sensing, analysis of reconnaissance images and industrial inspection...

There are many algorithms for contrast enhancement and among these, histogram equalization (*HE*) is the most common method used due to its simplicity and effectiveness.

*HE* can be categorized into two approaches: global and local *HE* [1]. Global *HE* uses the histogram information of the whole input image as its transformation function. This method is simple and powerful, but it can not adapt to local brightness features of the input image. This fact causes significant contrast losses in the background and other small regions. To overcome

this limitation, a local *HE* method has been developed, which can also be termed block-overlapped *HE* [282]. The procedure is to define first a rectangular neighborhood and move the center of this area from pixel to pixel. A histogram of that region is computed and then its *HE* function is determined. Thereafter, the center pixel of the region is histogram equalized using this function. The center of the neighborhood region is then moved to an adjacent pixel location and the procedure is repeated pixel by pixel for all input pixels. This method obviously allows each pixel to adapt to its neighboring region, so that high contrast can be obtained for all locations in the image. However, its computation complexity is very high. In [283], the computation is reduced with the use of a more effective and much faster contrast enhancement algorithm, which is based on partially overlapped sub-block *HE* transformation.

Another approach of contrast enhancement achieved by means of a local *HE* is that proposed in [284]. The scheme preserves the family of level-sets of the image by equalizing the histogram in all the connected components of the image. A variation of *HE* which uses both local and global information is described in [281]. The method presents a refinement of *HE* by using local image properties, generally called neighborhood metrics to subdivide histogram bins that would be otherwise indivisible in classical *HE*.

As said previously, the mean brightness of the histogram equalized image is always the middle grey level no matter how much the input image is bright or dark. This is not a desirable property in some applications where brightness preservation is necessary.

Mean preserving Bi-brightness equalization (BBHE) has been proposed then to overcome the aforementioned problem [285]. BBHE firstly separates the input image's histogram into two based on its mean: one having range from minimum grey level to mean and the other ranges from mean to the maximum grey level. Next, it equalizes the two histograms independently. It has been analyzed both mathematically and experimentally that this technique is to preserve the original brightness to a certain extent. Later, Equal Area Dualistic Sub-Image HE (DSIHE) [286] has been proposed and claimed to outperform BBHE both in term of brightness and also image content (entropy) preservation. Both BBHE and DSIHE is similar except that DSIHE choose to separate the histogram based on grey level with cumulative probability density equal to 0.5 instead of the mean as in BBHE. A novel extension of BBHE referred as the Minimum Mean Brightness Error Bi-Histogram Equalization with better brightness preservation is proposed in [280]. The main idea lies on separating the histogram using the threshold level that would yield minimum Absolute Mean Brightness Error. Variational perspectives of BBHE for brightness preserving *HE* can be found in [287], [288].

An extension of a typical histogram equalization, which utilizes cumulative density function of a quantized image and performs independent *HE* over two sub images obtained by decomposing the input image based on its mean is proposed in [289].

The representation and handling of the histogram is easy and straightforward in most of the cases. But when it comes to multicomponent image processing, the memory space required for the storage of classical multidimensional image histograms increases dramatically, which prevents the use of the exact vector histogram in most of the applications [290]. As a consequence, two strategies are commonly used:

1. A monodimensional histogram of each spectral component is handled separately. Although easy to do, this method does not take into account the cross-correlation between the different components.

2. A multivariate histogram processing with the re-quantization of each spectral component on a lower number of levels. Although this method enables the reduction of the memory size, it induces a loss of information.

More recently, the histogram explosion technique that performs full 3-D processing for, color images, and produces output images whose histograms approach the full display gamut was proposed in [291]. Although the method produces more useful results, the multivariate nature of histogram explosion requires much more computation than earlier color enhancement approaches. Therefore, for these images, there is more than one way to equalize the histogram. There is no obvious method of equalization as there is with single-channel images.

### 3.5. SUMMARY

Contrast enhancement is a common technique for revealing subtle details in grey level images as well as in color images. There exist a number of techniques for contrast enhancement and among them histogram equalization is the most popular. It expands the contrast between widely varying intensities. The algorithm attempts to equalize the number of pixels at every intensity level. This is usually accomplished by producing a cumulative histogram for the image and making it conform as closely as possible to the cumulative histogram of an image with all grey levels equally probable.

In the rapid and inevitably superficial survey of the previous section, we have seen that with a monochrome image of a single channel there is only one way to alter the histogram in this process. Many extensions to this technique have been developed to improve perceived performance. For multichannel and true-color images, there is more than one way to equalize the histogram. However, there is no obvious method of equalization for multichannel images as there is for single channel images.

Finally, we should emphasize that histogram equalization is one of those enhancement techniques that *work well* as judged by human observers even though the mathematical criteria are not completely understood.

# Chapter 4

## CONTRAST ENHANCEMENT OF SATELLITE IMAGES BASED SPATIAL CONTEXT

### 4.1. INTRODUCTION

Remote sensing image data typically contain an enormous amount of information. The answer to "*how can be this information extracted?*" constitutes a critical issue. From the field of digital image processing and computer vision, image interpretation is often greatly assisted by first applying histogram modification techniques to improve contrast and feature visibility.

The intent of this chapter is to propose two variational perspectives for contrast enhancement. These are essentially a refinement of histogram equalization (*HE*) which uses local relationships to remap the image gray levels. For multispectral images, the procedures are independent processing approaches.

In the first method, local image properties are deduced, firstly, by the use of a two level thresholding of a fuzzy 2-partition. Then, the spatial correlation in a predefined neighborhood is modeled using a local measure of spatial activity within the data, which we shall call a neighborhood metric. We formulate the second method as *HE* using a novel contextual spatial histogram.

### 4.2. CONTRAST ENHANCEMENT BASED THRESHOLDING

Brightness preservation is a desirable property in some applications. Brightness preserving Bi-Histogram Equalization (BBHE) has been proposed to overcome that problem [285]. The main idea of BBHE lies on separating the input image's histogram into two, using its mean as a threshold level. It has been analyzed that BBHE can preserve the original brightness to a

certain extent when the input histogram has a quasi-symmetrical distribution around its mean. Later, equal area Dualistic Sub-Image Histogram Equalization (DSIHE) has been proposed. It claims that if the separating level of histogram is the median of the input image's brightness, it will yield the maximum entropy after two independent sub-equalizations [286].

An alternative to the mean level and median level thresholding is to use a threshold value to create two sub-images in each of which pixels preserve similar properties. In image processing, thresholding is essentially a classification problem where one wishes to identify and extract object regions from their background on the basis of the similarity of brightness of image objects, for further processing.

Most of the proposed methods base the selection of suitable thresholds on the optimization of some criterion function which is related to the image and its properties. The fuzzy set theory has been successfully applied in several areas. With respect to automatic threshold selection the fuzzy methods lead to powerful and effective schema.

We propose a local contrast enhancement method based on the fuzzy 2-partition thresholding in the sense of both entropy maximization and between class variance maximization. The constraint of brightness preserving will not be explicitly expressed since it is implicit within the thresholding process. The local information is modeled to describe some spatial activity of the data in a predefined neighborhood system.

#### 4.2.1. BRIGHTNESS PRESERVING BI-HISTOGRAM EQUALIZATION

This section covers the essential of the Mean preserving Bi-Histogram Equalization (BBHE) algorithm proposed in [285].

We denote by  $X_m$  the mean of the image  $\mathbf{X}$  and assume that  $X_m \in \{X_0, X_1, \dots, X_{L-1}\}$ . Based on the mean, the input image is decomposed into two sub-images  $\mathbf{X}_L$  and  $\mathbf{X}_U$  such as:

$$\mathbf{X} = \mathbf{X}_L \cup \mathbf{X}_U \quad (4.1)$$

where

$$\mathbf{X}_L = \{\mathbf{X}(i, j) \mid \mathbf{X}(i, j) \leq X_m, \forall \mathbf{X}(i, j) \in \mathbf{X}\} \quad (4.2)$$

and

$$\mathbf{X}_U = \{\mathbf{X}(i, j) \mid \mathbf{X}(i, j) > X_m, \forall \mathbf{X}(i, j) \in \mathbf{X}\} \quad (4.3)$$

We define the respective probability density functions of the sub-images  $\mathbf{X}_L$  and  $\mathbf{X}_U$  as:

$$p_L(X_k) = \frac{n_L^k}{n_L} \quad k = 0, 1, \dots, m \quad (4.4)$$

and

$$p_U(X_k) = \frac{n_U^k}{n_U} \quad k = m+1, m+2, \dots, L-1 \quad (4.5)$$

$n_L^k$  and  $n_U^k$  stand for the respective numbers of  $X_k$  in  $\mathbf{X}_L$  and  $\mathbf{X}_U$ , and  $n_L$  and  $n_U$  are the total number of samples in  $\mathbf{X}_L$  and  $\mathbf{X}_U$ , respectively. The cumulative density functions for  $\mathbf{X}_L$  and  $\mathbf{X}_U$  are then defined as:

$$c_L(x) = \sum_{j=0}^k p_L(X_j) \quad k = 0, 1, \dots, m \quad (4.6)$$

and

$$c_U(x) = \sum_{j=m+1}^k p_U(X_j) \quad k = m+1, m+2, \dots, L-1 \quad (4.7)$$

where  $X_k = x$ . Note that  $c_L(X_m) = 1$  and  $c_U(X_{L-1}) = 1$  by definition.

Similar to the case of histogram equalization (*HE*), we define the partial transform functions exploiting the cumulative density functions such as:

$$f_L(x) = X_0 + (X_m - X_0)c_L(x) \quad (4.8)$$

$$f_U(x) = X_{m+1} + (X_{L-1} - X_{m+1})c_U(x) \quad (4.9)$$

Based on these transform functions, the decomposed sub-images are equalized independently and the composition of the resulting equalized sub-images constitute the output of BBHE that is  $\mathbf{Y}$ , expressed as:

$$\begin{aligned} \mathbf{Y} &= \{Y(i, j)\} \\ &= f_L(\mathbf{X}_L) \cup f_U(\mathbf{X}_U) \end{aligned} \quad (4.10)$$

where

$$f_L(\mathbf{X}_L) = \{f_L(X(i, j)) \mid \forall X(i, j) \in \mathbf{X}_L\} \quad (4.11)$$

and

$$f_U(\mathbf{X}_U) = \{f_U(X(i, j)) \mid \forall X(i, j) \in \mathbf{X}_U\} \quad (4.12)$$

Eqs. (4.11) and (4.12) show clearly that  $f_L(\mathbf{X}_L)$  equalizes the sub-image  $\mathbf{X}_L$  over  $(X_0, X_m)$  whereas  $f_U(\mathbf{X}_U)$  equalizes the sub-image  $\mathbf{X}_U$  over the range  $(X_{m+1}, X_{L-1})$ , and consequently the entire image is equalized over the entire range  $(X_0, X_{L-1})$  with the constraint that samples less than the input mean are mapped to  $(X_0, X_m)$  and samples greater than the mean are mapped to  $(X_{m+1}, X_{L-1})$ .

Concerning the mean brightness, suppose that  $\mathbf{X}$  is a random variable which has symmetric distribution around its mean  $X_m$ , ie.  $p(X \leq X_m) = p(X > X_m) = 1/2$ . When the sub-images are equalized independently, the mean brightness of the output of BBHE can be expressed as:

$$\begin{aligned} E(\mathbf{X}) &= E(\mathbf{Y} \mid X \leq X_m) p(X \leq X_m) + E(\mathbf{Y} \mid X > X_m) p(X > X_m) \\ &= 1/2 \{E(\mathbf{Y} \mid X \leq X_m) + E(\mathbf{Y} \mid X > X_m)\} \end{aligned} \quad (4.13)$$

It can be easily shown that:

$$E(\mathbf{Y} \mid X \leq X_m) = (X_0 + X_m) / 2 \quad (4.14)$$

and

$$E(\mathbf{Y} \mid X > X_m) = (X_m + X_{L-1}) / 2 \quad (4.15)$$

which results in:

$$E(\mathbf{Y}) = (X_m + X_G)/2 \quad (4.16)$$

where

$$X_G = (X_0 + X_{L-1})/2 \quad (4.17)$$

is the middle gray level. Eq. (4.16) shows that the output mean of BBHE is a function of the input mean brightness  $X_m$ , which indicates clearly that BBHE preserves the brightness, compared of the typical *HE* where output mean is always the middle gray level.

#### 4.2.2. DUALISTIC SUB-IMAGE HISTOGRAM EQUALIZATION

Dualistic Sub-Image Histogram Equalization (DSIHE) [285] is very similar to BBHE, except that the separating point  $X_D$  is selected as the median gray level of the input image, i.e.,  $X_D$  satisfies:

$$\int_0^D p_r(r) dr = 0.5 \quad (4.18)$$

The purpose of DSIHE is to find a separating point to yield the maximum entropy after two independent sub-equalizations. It is easy to p[rove that the brightness of the output image is :

$$E(\mathbf{Y}) = (X_D + X_G)/2 \quad (4.19)$$

where

$$X_G = (X_0 + X_{L-1})/2 \quad (4.20)$$

is the middle gray level of the input image. From (4.20), it is clear that DSIHE always pulls the output brightness toward the input middle level from the input median level.

#### 4.2.3. FUZZY 2-PARTITION THRESHOLDING

In this section, the fuzzy 2-partition entropy thresholding will be reviewed and the developed recursive version will be presented. Next, the 1-D Otsu method for two level thresholding will be quickly introduced, and the proposed extension of the scheme to the fuzzy domain with the recursive fast version will be presented.

##### 4.2.3.1. Probability Partition

Let  $D = \{(i, j) : i=0,1,\dots,M-1; j=0,1,\dots,N-1\}$  the domain on which an image  $\mathbf{X}$  with  $(L-1)$  gray level is defined. A pixel  $(i, j)$  with gray level  $X(i, j) = 0$  is **black** and is assumed to belong to the **object** class, while a pixel  $(i, j)$  with gray level  $X(i, j) = 255$  is **white** and is assumed to belong to the **background** class. For pixels  $(i, j)$  with other gray levels, i.e.  $0 < X(i, j) < 255$ , are assumed to be in the gray area between these two classes. In other words, we can say they partly belong to the **object** and partly belong to the **background** [297].

Having a threshold  $T$ , we define the two partitions of  $\mathbf{X}$  generated by  $T$  as:

$$D_d = \{(i, j) : X(i, j) \leq T, (i, j) \in D\} \quad (4.21)$$

and

$$D_b = \{(i, j) : X(i, j) > T, (i, j) \in D\} \quad (4.22)$$

with probability distributions of the pixels of  $D$  belonging to classes *object* and *background*, respectively:

$$P(D_d) = \sum_{k=0}^T P(x_k) \quad (4.23)$$

and

$$P(D_b) = \sum_{k=T}^{L-1} P(x_k) \quad (4.24)$$

#### 4.2.3.2. Fuzzy Probability

The fuzzy probability of class A is defined as:

$$p_A = \mu_A \cdot P(A) \quad (4.25)$$

where  $\mu_A$  is the characteristic function of A referred to as fuzzy *membership* function, and  $P(A)$  is the probability of class A.

#### 4.2.3.3. Fuzzy 2-Parttion Entropy For Two-Level Thresholding

- **Basic Algorithm**

In the approach proposed in [298], an image is modeled with two fuzzy sets; dark and bright (object class and background). For two-level thresholding, the pixels with gray level  $k$  can belong partially to the background class and the object. The probability of the pixels with gray level  $k$  belonging to a certain class is represented by its fuzzy membership function  $\mu$ . The membership function can have different shapes, but for simplicity it is usually assumed to be a function as shown in Fig. 4.1. The fuzzy membership functions of the two classes, object  $\mu_d(k)$  and background  $\mu_b(k)$  are defined as below:

$$\mu_d(k) = \begin{cases} 1, & k \leq a \\ \frac{k-c}{a-c}, & a < k < c \\ 0, & k \geq c \end{cases} \quad (4.26)$$

$$\mu_b(k) = \begin{cases} 0, & k \leq a \\ \frac{k-a}{c-a}, & a < k < c \\ 1, & k \geq c \end{cases} \quad (4.27)$$

where  $a$  and  $c$  are parameters determining the shape of the above two membership functions.

Based on the fuzzy set model of an image and the maximum entropy principle, an exhaustive search is used to find the pair  $a_{opt}$  and  $c_{opt}$  which forms a fuzzy 2-partition that has the maximum entropy.

For an 8-bit image with 256 gray levels ranging from 0 to 255, the entropy of this fuzzy 2-partition is given by:

$$H = -P(dark) \cdot \log(P(dark)) - P(bright) \cdot \log(P(bright)) \quad (4.28)$$

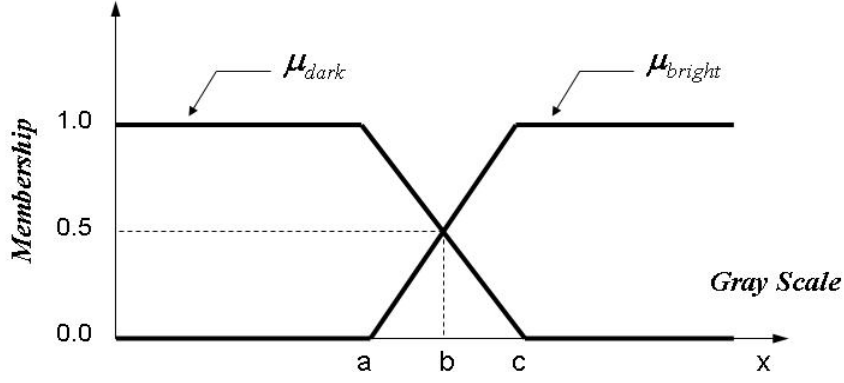


Fig.4.1: Fuzzy membership functions.

where

$$P(dark) = \sum_{i=0}^{255} \mu_d(i) P(i) \quad (4.29)$$

$$P(bright) = \sum_{i=0}^{255} \mu_b(i) P(i) \quad (4.30)$$

stand for the probabilities of the fuzzy sets dark and bright, respectively.

The optimal threshold value  $T$  is the crossover point of the fuzzy sets

$$T = \frac{(a_{opt} + c_{opt})}{2} \quad (4.31)$$

that satisfies

$$H(T) = \max (H(t)) \quad t = 0, \dots, L-1 \quad (4.32)$$

#### • Recursive Algorithm

The recursive algorithm proposed in [237] reduces the computation complexity of the basic algorithm bounded by  $O(L^3)$  to  $O(L^2)$ .

According to Eq. (4.26), the formula for calculating  $\mu_d(i)$  can be rewritten as:

$$\mu_d(i) = 1 - \mu_b(i) \quad (4.33)$$

The probability of the fuzzy dark set is thus defined as:

$$P(dark) = 1 - P(bright) \quad (4.34)$$

The entropy of the fuzzy 2-partition can be obtained as:

$$H = -\log (1 - P(bright)) + P(bright) \cdot \log \left( \frac{1 - P(bright)}{P(bright)} \right) \quad (4.35)$$

where  $P(bright)$  is subdivided such as:

$$P(\text{bright}) = \sum_{g=a+1}^{c-1} \frac{g-a}{c-a} \cdot P(g) + \sum_{g=c}^{255} P(g) \quad (4.36)$$

In the method we propose, only the probability of the bright fuzzy set will be computed recursively and then used to compute the entire entropy of the fuzzy 2-partition according to Eq. (4.35). There is no need to compute the membership function of for any fuzzy set.

The recursive algorithm is implemented as follows:

For  $a = 0$  to 254

For  $c = (a+1)$  to 255

1. Compute the probability vector  $P_c$  such that

$$P_c = \sum_{g=c}^{255} p(g) \quad ; \quad c = 1, \dots, 255 \quad (4.37)$$

and recursively

$$P_c = P_{c-1} - p(c-1); \quad c=2, \dots, 255; \quad (4.38)$$

2. Compute the probability matrix  $P_{a,c}$  such that:

$$\begin{cases} P_{a,c} = \sum_{g=a+1}^{c-1} (g-a)P(g) & (a=0, \dots, 255); (c=a+2, \dots, 255) \\ P_{a, a+1} = 0 \end{cases} \quad (4.39)$$

and recursively

$$P_{a,c} = P_{a,c-1} + (c-a-1) \cdot p(c-1) \quad (4.40)$$

3. Compute the total probability matrix  $P(\text{bright}), P_b$ , such that:

$$P_b(a, c) = P_{c-1} + \frac{1}{c-a} \cdot (P_{a,c-1} - p(c-1)) \quad (4.41)$$

4. Compute the entropy of this fuzzy 2-partition according to Eq. (4.35). The selected threshold value  $T_{\text{opt}}$  is the value that satisfies (4.31) and (4.32).

/\* End c \*/

/\* End a \*/

#### 4.2.3.4. Maximization of the Between-Class Variance of A Fuzzy 2-Parttion

##### • Basic Algorithm

The 1-D Otsu method for two level thresholding is based on the maximization of the between-class variance criterion [299]. It is formally defined by the following procedures:

1. Calculate the size  $t_i$  for each of the class  $C_i, i = 0, 1$ , according to

$$t_i = \sum_{D_j} h(j) \quad (4.42)$$

2. Calculate the size  $m_i$  for each of the class  $C_i$ ,  $i = 0, 1$ , according to

$$m_i = \sum_{D_j} j \cdot h(j) / t_i \quad (4.43)$$

Where  $h$  is the histogram and  $D_j$  is the set of gray levels belonging to the class  $C_i$ . The optimal threshold value,  $T$ , is selected so that to maximize the between-class variance

$$B = t_0 \cdot t_1 \cdot (m_0 - m_1)^2 \quad (4.44)$$

- **Fuzzy 2-Partition Algorithm**

The purpose of the fuzzy version of the 1-D Otsu method is to take an effective use of both the power of fuzzy set theory and the efficiency of the maximization of the between-class variance matrix criterion to improve the performance of the basic method.

**i) Definitions**

For an 8-bit image with 256 gray levels ranging from 0 to 255, modeled by two fuzzy sets; dark and bright (object class and background), whose membership functions are those defined by (4.26) and (4.27), we define the size of the fuzzy events dark and bright as:

$$t(\text{bright}) = t_b = \sum_{i=0}^{255} \mu_b(i) \cdot h(i) \quad (4.45)$$

$$t(\text{dark}) = t_d = \sum_{i=0}^{255} \mu_d(i) \cdot h(i) \quad (4.46)$$

and the corresponding mean levels:

$$m(\text{bright}) = m_b = \sum_{i=0}^{255} i \cdot \mu_b(i) \cdot h(i) / t_b \quad (4.47)$$

$$m(\text{dark}) = m_d = \sum_{i=0}^{255} i \cdot \mu_d(i) \cdot h(i) / t_d \quad (4.48)$$

Using (4.33), Eqs. (4.46) and (4.48) can be rewritten as follows:

$$t_d = H_t - t_b \quad (4.49)$$

and

$$m_d = \frac{H_t \cdot m_t - m_b \cdot t_b}{H_t - t_b} \quad (4.50)$$

where

$$H_t = \sum_{i=0}^{255} h(i) \quad (4.51)$$

and

$$m_t = \sum_{i=0}^{255} i \cdot h(i) / H_t \quad (4.52)$$

$H_t$  is the total number making up the image and  $m_t$  is its expected value. The between class variance matrix B is given by:

$$B = (H_t - tb) \cdot tb \cdot \left( \frac{H_t \cdot (m_t - mb)}{H_t - tb} \right)^2 \quad (4.53)$$

## ii) Recursive Method

The proposed recursive method performs into two steps, and needs only the calculation of the size and the mean level value of the bright event.

**1) Computation of the Size:** the procedure of calculating the size of the bright event is summarized as follows.

For  $a = 0$  to 254

For  $c = (a+1)$  to 255

1. Compute the frequency vector  $H_c$  such that

$$H_c = \sum_{g=c}^{255} h(g) \quad c=1, \dots, 255 \quad (4.54)$$

and recursively

$$H_c = H_{c-1} - h(c-1); \quad c=2, \dots, 255 \quad (4.55)$$

2. Compute the frequency matrix  $H_{a,c}$  such that:

$$\begin{cases} H_{a,c} = \sum_{g=a+1}^{c-1} (g-a) \cdot h(g) & (a=0, \dots, 254); (c=a+2, \dots, 255) \\ H_{a,a+1} = 0 \end{cases} \quad (4.56)$$

and recursively

$$H_{a,c} = H_{a,c-1} + (c-a-1) \cdot h(c-1) \quad (4.57)$$

3. Compute the total matrix size  $t_b$  of the bright event such that:

$$t_b(a,c) = H_{c-1} + \frac{1}{c-a} \cdot [H_{a,c-1} - h(c-1)] \quad (4.58)$$

/\* End c \*/

/\* End a \*/

**2) Computation of the Mean Value:** Similarly, the recursive calculation of the mean of the bright event is outlined below.

For  $a = 0$  to 254

For  $c = (a+1)$  to 255

1. Compute the mean vector  $M_c$  such that

$$M_c = \sum_{g=c}^{255} g \cdot h(g) \quad c = 1, \dots, 255 \quad (4.59)$$

and recursively

$$M_c = M_{c-1} - (c-1) \cdot h(c-1) \quad c = 2, \dots, 255 \quad (4.60)$$

2. Compute the mean values matrix  $M_{a,c}$  such that:

$$M_{a,c} = \sum_{g=a+1}^{c-1} g \cdot (g-a) \cdot h(g) \quad (4.61)$$

and recursively

$$M_{a,c} = M_{a,c-1} + (c-a-1) \cdot (c-1) \cdot h(c-1) \quad (4.62)$$

3. Compute the total mean values matrix size  $m_b$  of the bright event such that:

$$m_b(a,c) = \frac{1}{tb} \cdot \left[ M_c + \frac{1}{c-a} \cdot M_{a,c} \right] \quad (4.63)$$

/\* End c \*/

/\* End a \*/

The selected threshold value  $T_{opt}$  is the mid-point of  $a_{opt}$  and  $c_{opt}$  that maximizes the between class variance  $B(T_{opt})$  given by (4.53).

#### 4.2.4 FUZZY 2-PARTITION THRESHOLDING FOR LOCAL CONTRAST ENHANCEMENT

As has been said above, the Local Fuzzy 2-Partition Thresholding for Contrast Enhancement (LFPTCE) is a novel alternative to the brightness preserving contrast enhancement scheme without any mathematical formulation of some constraints of brightness. Inspired by the work in [281], we formulate our solution as histogram equalization using a specific neighborhood metric as sorting function to subdivide large bins in the original histogram.

##### 4.2.4.1. Sorting Function

In the classical *HE* algorithm, the original histogram is subdivided into bins where pixels have the same gray level. The use of the sorting function will have the effect of subdividing the original histogram bins into sub-bins where pixels in each sub-bin share the same gray level and neighborhood metric value.

##### 4.2.4.2. Neighborhood Metric

We now consider in detail the neighborhood metric used to model the spatial correlation between pixels in a local neighborhood of the input image.

- **Spatial Neighborhood Definition**

Let  $D = \{(i, j): i=0,1,\dots,M-1; j=0,1,\dots,N-1\}$  the domain on which an image  $\mathbf{X}$  with  $(L-1)$  gray level is defined. The spatial neighborhood model used is that of the common second

order neighborhood shown in Fig. 2.1b (chapter 2), and defined as a simple stacked vector of the neighboring pixels:

$$N^{(u,v)} = [(p,q) : p \in \{u-1, u, u+1\}, q \in \{v-1, v, v+1\}, (p,q) \neq (u,v)] \quad (4.64)$$

- **Neighborhood Metric Definition**

We define our metric as the *second order derivative metric* given by the following four differences:

$$\begin{aligned} d_{i,j}^1(x) &= X(i, j+1) - 2 * X(i, j) + X(i, j-1) \\ d_{i,j}^2(x) &= X(i-1, j) - 2 * X(i, j) + X(i+1, j) \\ d_{i,j}^3(x) &= 1/2 [X(i-1, j+1) - 2 * X(i, j) + X(i+1, j-1)] \\ d_{i,j}^4(x) &= 1/2 [X(i-1, j-1) - 2 * X(i, j) + X(i+1, j+1)] \end{aligned} \quad (4.65)$$

The quantity  $d_{i,j}^k(x)$ , for  $k = 1, 2, 3, 4$ , provides a local measure of spatial activity within the data. In smooth image regions,  $d_{i,j}^k(x)$  is a small value, while at edges  $d_{i,j}^k(x)$  is large.

We associate to the derivative metric  $d_{i,j}^k(x)$  the following *voting* function:

$$V(d_{i,j}^k) = \begin{cases} 0, & |d_{i,j}^k| \leq \beta \\ 1, & d_{i,j}^k > \beta \\ -1, & d_{i,j}^k < -\beta \end{cases} \quad (4.66)$$

$V(d_{i,j}^k)$  is defined in the spirit of the Huber-Markov edge-preserving function used effectively to preserve discontinuities in image restoration applications.  $V(d_{i,j}^k)$  serves to penalize discontinuities within the data dependent upon a free positive parameter  $\beta$ .

#### 4.2.4.3. Algorithm

The contextual spatial algorithm, LFPTCE is summarized through the following key steps:

1. Compute the derivative metric for each pixel in the input image.
2. Subdivide the original histogram into sub-bins using the gray level as the primary sort key and the voting function  $V(d_{i,j}^k)$  as the secondary sort key.
3. Find the threshold  $X_T$  that yields a two-level thresholding with maximum entropy or maximum between-class variance, either the entropic criterion or cross-variance criterion is used.
4. Separate the sorted histogram obtained in step 2 into two, based on the threshold  $X_T$  found in step 3 and equalize them independently.

### 4.3. CONTEXTUAL SPATIAL HISTOGRAM FOR CONTRAST ENHANCEMENT

The basic thought of the Contextual Spatial Histogram for Contrast Enhancement (CSHCE) is to achieve a contrast enhancement which preserves the brightness of the input

image and employs a contextual bi-dimensional histogram to characterize the spatial relationships.

#### 4.3.1. CONTEXTUAL SPATIAL NEIGHBORHOOD

In the basic *HE* scheme, pixels are modified by a transformation function based on the gray level distribution over an entire image. In the method at hand, we propose a transformation function based on a joint gray level distribution in a local neighborhood,  $N_{ij}$ , of every pixel  $(i,j)$  (Fig. 4.2b), defined over a predefined area,  $C$ , in the image (Fig. 4.2a). In other words, we consider  $C$  as the area in the neighborhood of the area  $\bar{C}$  over the entire image, i.e.,  $C \cup \bar{C} = D$ . The transformation function will be defined using the area  $C$ , and then will be applied to the entire image for the purpose of contrast enhancement.

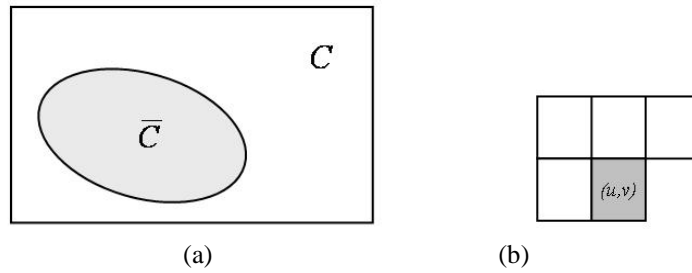


Fig. 4.2: Contextual spatial neighborhood system. (a) Contextual area for transformation function definition. (b) Local neighborhood system  $N_{ij}$  for every pixel  $(i,j)$ .

#### 4.3.2. CONTEXTUAL SPATIAL HISTOGRAM

Let  $\mathbf{X}$  be an image defined on  $D = \{(i, j): i=0,1,\dots,M-1; j=0,1,\dots,N-1\}$ , with gray levels in the range  $[0, L-1]$ . Let  $X(i, j) = X_r$  and  $X(k, l) = X_s$ , where  $(k, l) \in N_{ij}$  and  $N_{ij} \in C$ . The contextual spatial histogram defined on  $N_{ij}$ , over the area  $C$  is given by:

$$H_c = \left\{ p_{rs} = \frac{n_{rs}}{L^2}, \quad r, s = 0, 1, \dots, L-1 \right\} \quad (4.67)$$

where  $n_{rs}$  represents the number of times that the level  $X_r$  appears having the level  $X_s$  in his neighborhood such as  $X_r$  represents the pixel  $(i,j)$  whilst  $X_s$  represents the pixel  $(k,l)$ .

#### 4.3.3. CONTEXTUAL CUMULATIVE DENSITY FUNCTION

We define the contextual cumulative density function as:

$$Y_k = c_c(x) = \sum_{i=0}^k \sum_{j=0}^{L-1} p_{ij} = \sum_{i=0}^k \sum_{j=0}^{L-1} (n_{ij}/L^2) \quad (4.68)$$

where  $X_k = x$ , for  $k = 0, 1, \dots, L-1$ . Note that  $c_c(X_{L-1}) = 1$ , by definition. If we define a transform function  $f_c(x)$  based on the cumulative density function such as:

$$f_c(x) = X_0 + (X_{L-1} - X_0)c_c(x) \quad (4.69)$$

Then the output image of the CSHCE method,  $\mathbf{Y} = \{Y(i, j), (i, j) \in D\}$  can be expressed as:

$$\begin{aligned} \mathbf{Y} &= f_c(\mathbf{X}) \\ &= \{f_c(X(i, j), \forall X(i, j) \in \mathbf{X}, (i, j) \in D\} \end{aligned} \quad (4.70)$$

#### 4.3.4. ALGORITHM

The CSHCE brightness preserving algorithm is summarized through the following key steps:

1. Define the areas  $C$  and  $\bar{C}$  in the image such as  $C \cup \bar{C} = D$ .
2. Compute the contextual spatial histogram  $H_c$  for every pixel  $(i, j) \in C$ .
3. Find the threshold  $X_T$  that yields a two-level thresholding with maximum between-class variance criterion for the entire image.
4. Separate the sorted histogram obtained in step 2 into two, based on the threshold  $X_T$  found in step 3 and equalize them independently, using (4.68).

#### 4.4. EXPERIMENTAL RESULTS

The proposed algorithms, LFPTCE and CSHCE, besides *HE*, BBHE and DSIHE methods are simulated on the remote sensing images described in chapter 2 (section 2.8.1). The comparison was made using three quality metrics: the Absolute Mean Brightness Error (*AMBE*), the contrast-per-pixel  $C$ , and the distortion. We note that contrast and distortion are competing measures, since increased contrast also increases distortion. The best result is one that increases contrast significantly while increasing distortion only slightly.

##### 4.4.1 LOCAL CONTRAST ENHANCEMENT BASED THRESHOLDING SIMULATIONS

###### 4.4.1.1 Thresholding Results

The BBHE, DSIHE and LFPTCE algorithms are based on the use of a threshold level to preserve the brightness. The corresponding two-level images of Channels 1-5 and 7 are represented in Figs. 4.3-4.8. As can be seen in Figs. 4.3d-4.5d and in Fig. 4.8d, the main components of the image are well segmented and the main features are preserved, whilst in Figs. 4.3a,b,c-4.5a,b,c some contours disappear and some false contours appear. In Figs. 4.7a,b,c-4.8a,b,c, the contours in some regions are slightly more preserved than in Fig. 4.7d-4.8d. Clearly, the proposed Otsu method for fuzzy 2-partition thresholding behaves better with images in the Visible (Vis) channel (Bands 1,2, 3) than with Infra Red (IR) images (Bands 4, 5 and 7). Note that the Otsu method for fuzzy 2-partition thresholding has been developed initially for single channel gray level images.

###### 4.4.1.2 Contrast Enhancement Results

Table 4.1 shows the quantitative results of the LFPTCE algorithm obtained on channels 1-5 and 7 of the September sub-image, together with HE, BBHE and DSIHE for comparison. The obtained gains of *AMBE* and contrast  $C$  and distortion are reported with respect to the HE method. From the results, we see that the LFPTCE-ME (Local Fuzzy 2-Partition for Contrast Enhancement with the Maximum Entropy criterion) and the DSIHE produce in average the less contrasted images with distortion and absolute mean brightness values fairly high ( $G-C = -7.54\%$ ,  $G- = -2.52\%$ ) and ( $G-C = -2.52\%$ ,  $G- = -5.74\%$ ) respectively. The gains are gradually enhanced with the BBHE ( $G-C = 0.12\%$ ,  $G- = 12.76\%$ ). However, the best results are those obtained with the proposed LFPTCE-MV (Local Fuzzy 2-Partition for Contrast Enhancement with the Maximum Between-Variance criterion) method ( $G-C = 12.11\%$ ,  $G- = 42.53\%$ ). Concerning the brightness, clearly the proposed LFPTCE-MV has increased the brightness preservation ( $G-AMBE = 81.73\%$ ) and yielded a more natural enhancement than LFPTCE-ME ( $G-AMBE = 66.93\%$ ), BBHE ( $G-AMBE = 66.19\%$ ) and DSIHE ( $G-AMBE = 55.83\%$ ). Note that the LFPTCE-MV provides better results for images

the Vis channel than for images in the IR Channel. Finally, we should mention that values ranging from 0 to 4 of the free parameter  $\alpha$  in (4.66) yielded similar quality of contrast enhancement, thus simulations were conducted with the value  $\alpha = 0$ . Figs. 4.9-4.14 display the results of achieved contrast enhancement of the channels 1-5 and 7 of the September sub-image.

#### 4.4.2 CONTEXTUAL SPATIAL HISTOGRAM FOR CONTRAST ENHANCEMENT RESULTS

The main idea behind the development of the CSHCE method for remote sensing images is to reproduce the brightness property of the input image by means of a local enhancement process in which the spatial relationships between neighboring pixels are exploited, besides the spatial relationships between neighboring areas where various land cover classes can be found in each area.

To verify the effectiveness of the proposed method different locations and sizes of the area  $C$  have been adopted with the use of the same groups of masks used in chapter 2, besides the mask  $C_E$  in Fig. 4.15b. For each mask, the CSHCE algorithm was tested in two ways.

First, we consider the area  $C$  outside the mask. The results for Band 1 in the Vis channel and Band 4 in the IR channel of the September sub-image are shown in Table 4.2 and Figs. 4.16-4.17. The table shows that the results are highly related to the spectral channel of the image, the land cover, the dimension and location of the area  $C$ . The area outside the largest mask  $C_D$  produces the best combination of results comparing to LFPTCE-MV: contrast enhancement is better of 51% for Band 1 and 90.84% for Band4, brightness is better of 9.07% for Band 1 and 18.32% for Band 4 and no more distortion is introduced in excess. The results decrease gradually with masks  $C_{C,B,A}$ , but contrast enhancement remain better than LFPTCE-MV with less distortion and comparable values of brightness preserving. The brightness preservation decreases slightly with the use of masks  $C_{I,2,3,4,E}$ , however, contrast enhancement remain better than LFPTCE-MV with less distortion in Band 1. For Band 4, the results obtained still outperform LFPTCE-MV results.

Secondly, we consider the area  $C$  inside the mask. The results for Band 1 and Band 4 are shown in Table 4.3 and Figs.4.18-4.19. The choice of such areas decreases notably the brightness preservation in Band 1, but the images remain less distorted with better contrast enhancement than LFPTCE-MV. In Band 4, however, the CSHCE algorithm improves the brightness preservation and contrast enhancement with less distortion.

#### 4.5. SUMMARY

We presented two novel extensions of brightness preserving contrast enhancement techniques. Both of the two methods use a fuzzy 2-partition thresholding scheme for brightness preserving. The first method models the spatial relationships with the use of a neighborhood metric which provides a local measure of spatial activity within the data. The second method uses a contextual spatial joint probability within a local neighborhood system, over a local area to remap the gray levels of the pixels in the entire image. Accordingly, our methods are able to achieve better contrast enhancement and brightness preservation with less distortion than some popular brightness preserving techniques.

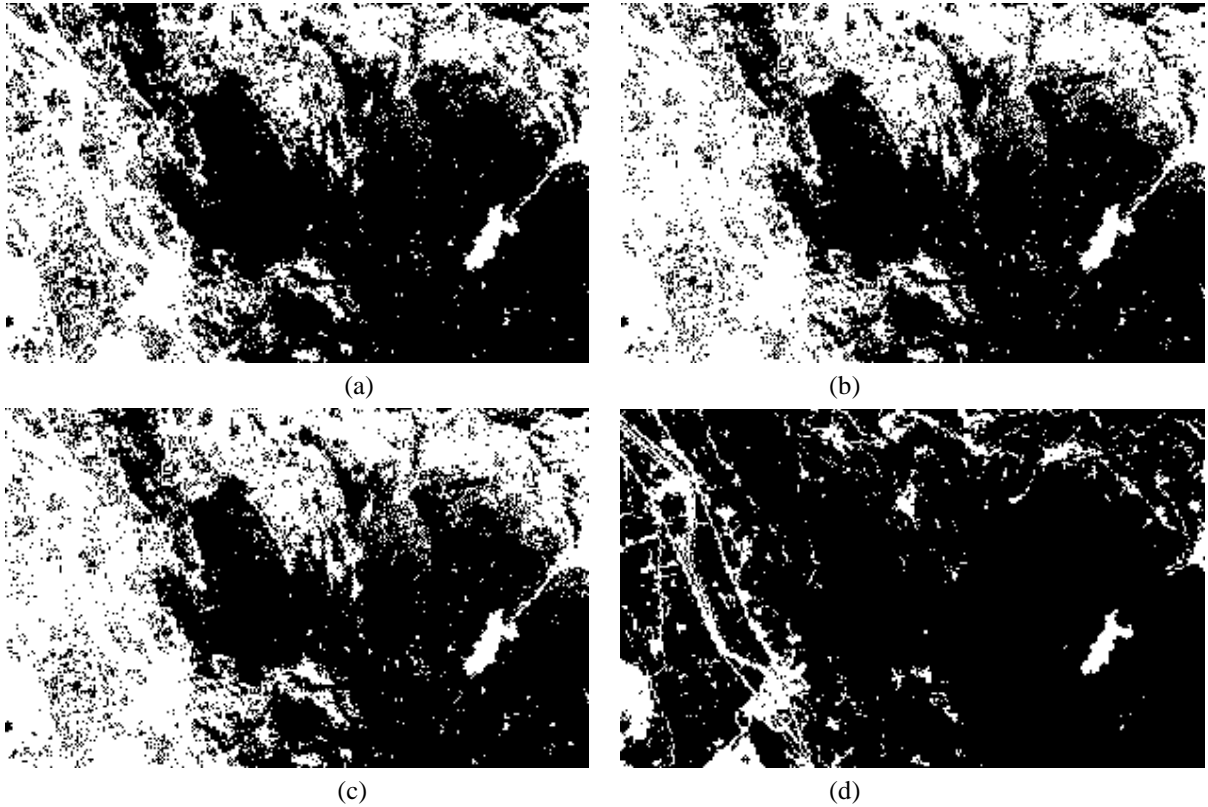


Fig. 4.3: Two level thresholding of channel 1 of the September sub-image with (a) BBHE. ( $T = 65$ ).  
 (b) DSIHE ( $T = 59$ ). (c) Fuzzy 2-partition maximum entropy criterion ( $T = 57$ ).  
 (d) Fuzzy 2-partition maximum between-variance criterion ( $T = 105$ ).

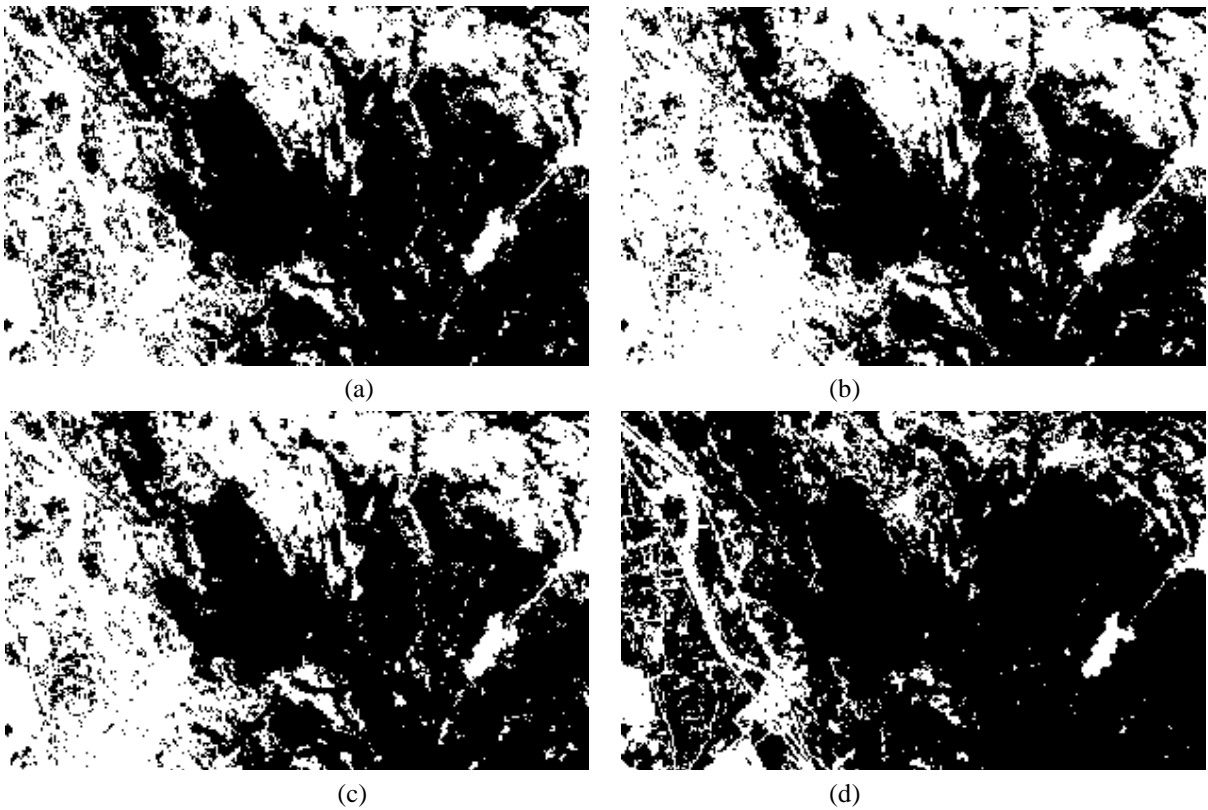


Fig. 4.4: Two level thresholding of channel 2 of the September sub-image with (a) BBHE. ( $T = 78$ ).  
 (b) DSIHE ( $T = 71$ ). (c) Fuzzy 2-partition maximum entropy criterion ( $T = 75$ ).  
 (d) Fuzzy 2-partition maximum between-variance criterion ( $T = 101$ ).

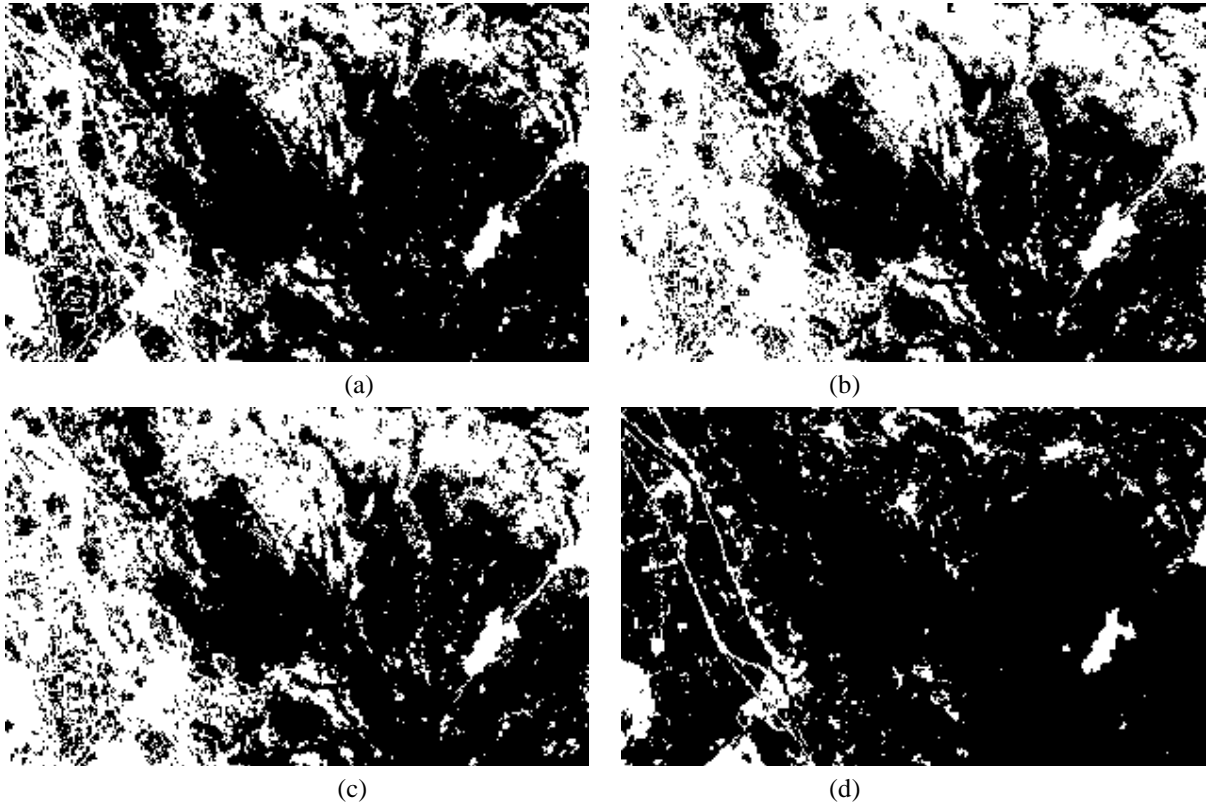


Fig. 4.5: Two level thresholding of channel 3 of the September sub-image with (a) BBHE. ( $T = 57$ ).  
 (b) DSIHE ( $T = 45$ ). (c) Fuzzy 2-partition maximum entropy criterion ( $T = 48$ ).  
 (d) Fuzzy 2-partition maximum between-variance criterion ( $T = 106$ ).

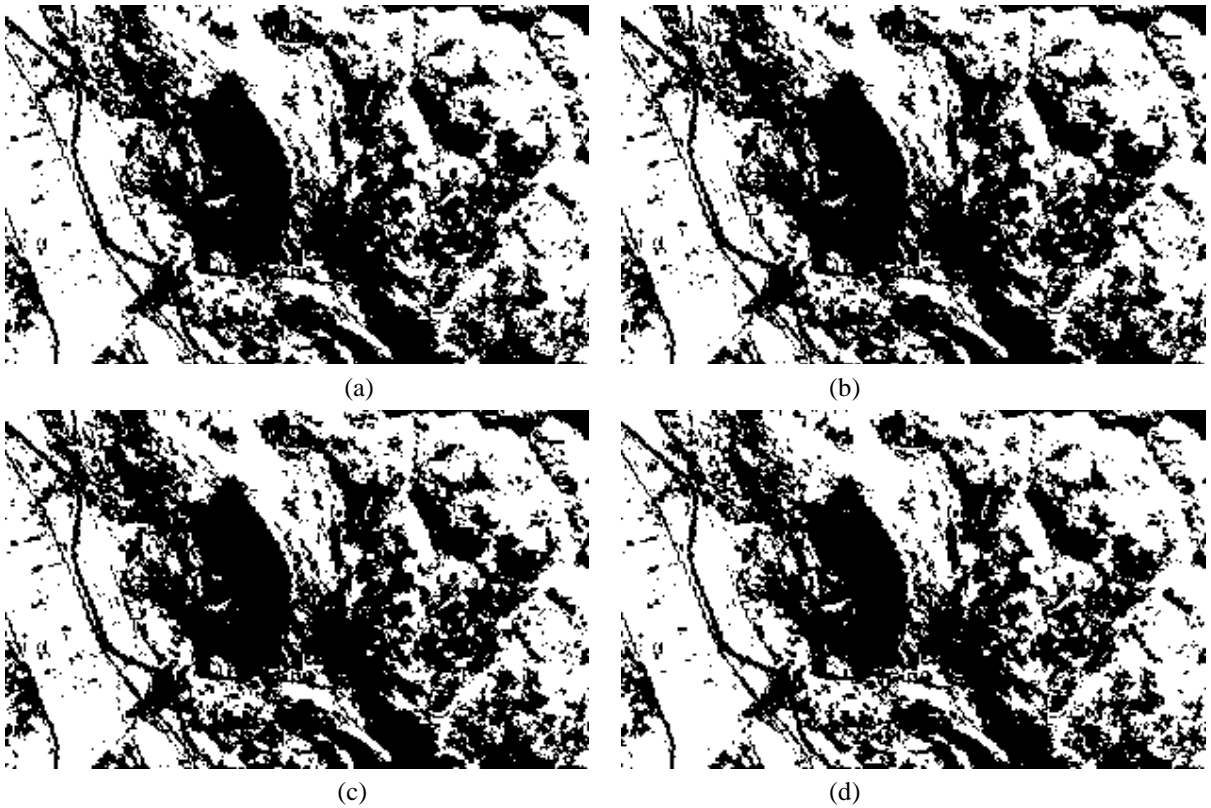


Fig. 4.6: Two level thresholding of channel 4 of the September sub-image with (a) BBHE. ( $T = 154$ ).  
 (b) DSIHE ( $T = 157$ ). (c) Fuzzy 2-partition maximum entropy criterion ( $T = 157$ ).  
 (d) Fuzzy 2-partition maximum between-variance criterion ( $T = 150$ ).

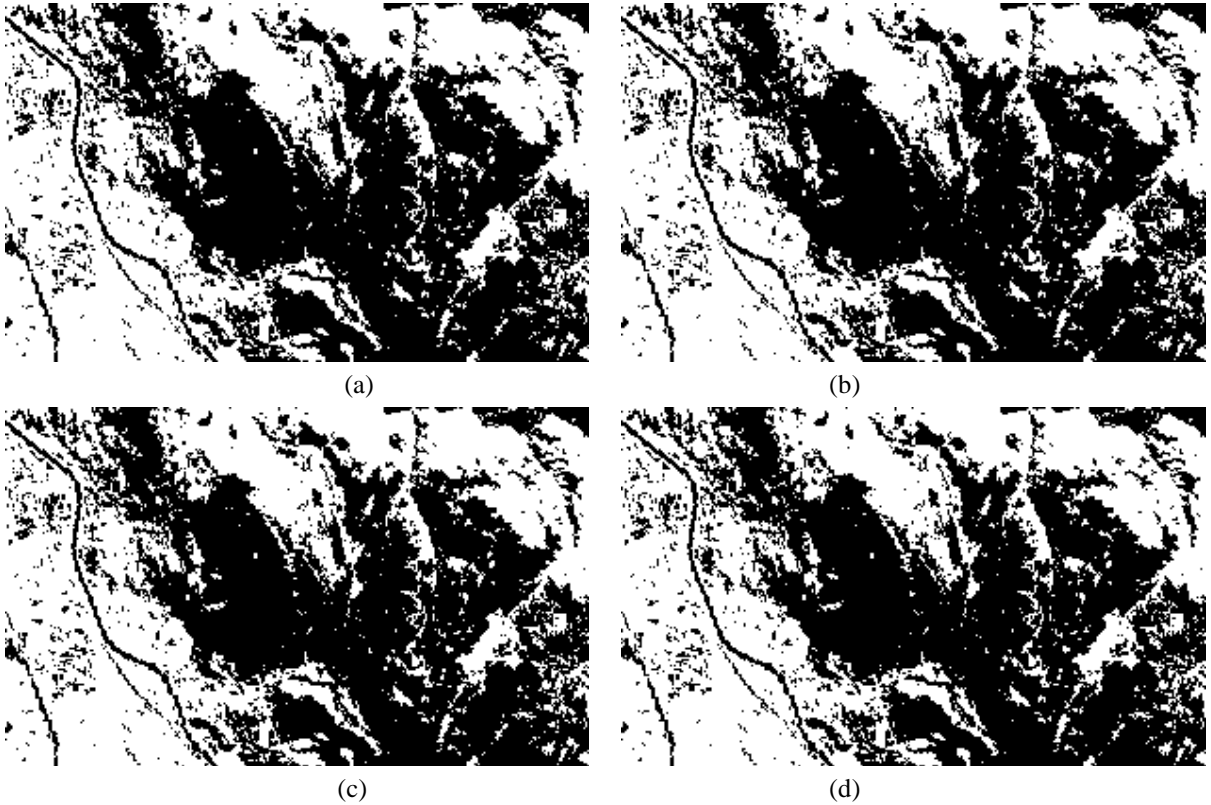


Fig. 4.7: Two level thresholding of channel 5 of the September sub-image with (a) BBHE. ( $T = 110$ ).  
 (b) DSIHE ( $T = 112$ ). (c) Fuzzy 2-partition maximum entropy criterion ( $T = 110$ ).  
 (d) Fuzzy 2-partition maximum between-variance criterion ( $T = 110$ ).

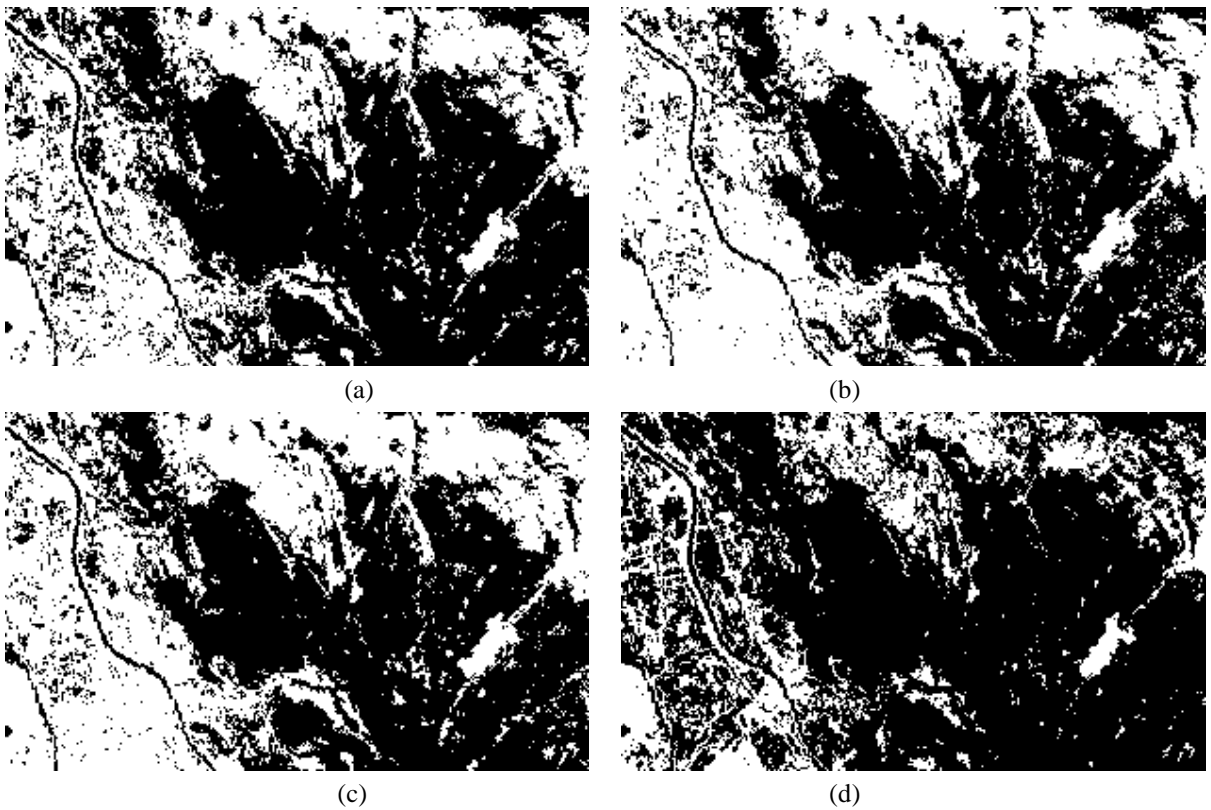


Fig. 4.8: Two level thresholding of channel 7 of the September sub-image with (a) BBHE. ( $T = 77$ ).  
 (b) DSIHE ( $T = 69$ ). (c) Fuzzy 2-partition maximum entropy criterion ( $T = 72$ ).  
 (d) Fuzzy 2-partition maximum between-variance criterion ( $T = 96$ ).

Band	Method	$T$	G-AMBE (%)	G-C (%)	G- (%)
<b>B1</b>	HE	-	<b>69.83</b>	<b>240.10</b>	<b>0.29</b>
	BBHE	65	69.18	00.47	17.24
	DSIHE	59	58.34	- 02.18	- 03.45
	LFPTCE-ME	57	64.60	-12.18	- 06.90
	LFPTCE-MV	105	93.41	24.7	75.86
<b>B2</b>	HE	-	<b>54.91</b>	<b>206.03</b>	<b>0.20</b>
	BBHE	78	67.26	- 04.48	05.00
	DSIHE	71	54.67	- 05.26	- 15.00
	LFPTCE-ME	75	67.47	- 14.20	- 05.00
	LFPTCE-MV	101	97.63	19.72	65.00
<b>B3</b>	HE	-	<b>75.6</b>	<b>232.28</b>	<b>0.47</b>
	BBHE	57	78.27	07.15	59.57
	DSIHE	45	58.15	- 03.31	12.77
	LFPTCE-ME	48	67.83	- 07.36	25.53
	LFPTCE-MV	106	86.81	30.57	82.98
<b>B4</b>	HE	-	<b>23.73</b>	<b>237.78</b>	<b>0.07</b>
	BBHE	154	66.20	01.12	00.00
	DSIHE	157	59.80	00.74	00.00
	LFPTCE-ME	157	52.30	- 03.16	00.00
	LFPTCE-MV	150	64.56	- 01.83	00.00
<b>B5</b>	HE	-	<b>19.76</b>	<b>231.02</b>	<b>0.09</b>
	BBHE	110	48.89	- 01.37	- 11.11
	DSIHE	112	48.89	- 01.72	- 11.11
	LFPTCE-ME	110	55.82	- 04.83	- 11.11
	LFPTCE-MV	110	55.82	- 04.83	- 11.11
<b>B6</b>	HE	-	<b>53.34</b>	<b>240.89</b>	<b>0.17</b>
	BBHE	77	67.34	- 02.13	05.88
	DSIHE	69	55.17	- 03.43	- 17.65
	LFPTCE-ME	72	63.42	- 07.61	- 17.65
	LFPTCE-MV	96	92.18	04.38	41.18

(a)

Method	G-AMBE (%)	G-C (%)	G- (%)
HE	<b>49.52</b>	<b>231.35</b>	<b>0.21</b>
BBHE	66.19	00.12	12.76
DSIHE	55.83	- 02.52	- 05.74
LFPTCE-ME	66.93	- 07.54	- 02.52
LFPTCE-MV	81.73	12.11	42.31

(b)

TABLE 4.1. QUANTITATIVE RESULTS OBTAINED FOR LOCAL FUZZY 2-PARTITION FOR CONTRAST ENHANCEMENT. (A) INDIVIDUAL RESULTS OF THE SEPTEMBER SUB-IMAGE. (B) AVERAGED VALUES ON THE SIX CHANNELS OF THE SEPTEMBER SUB-IMAGE.

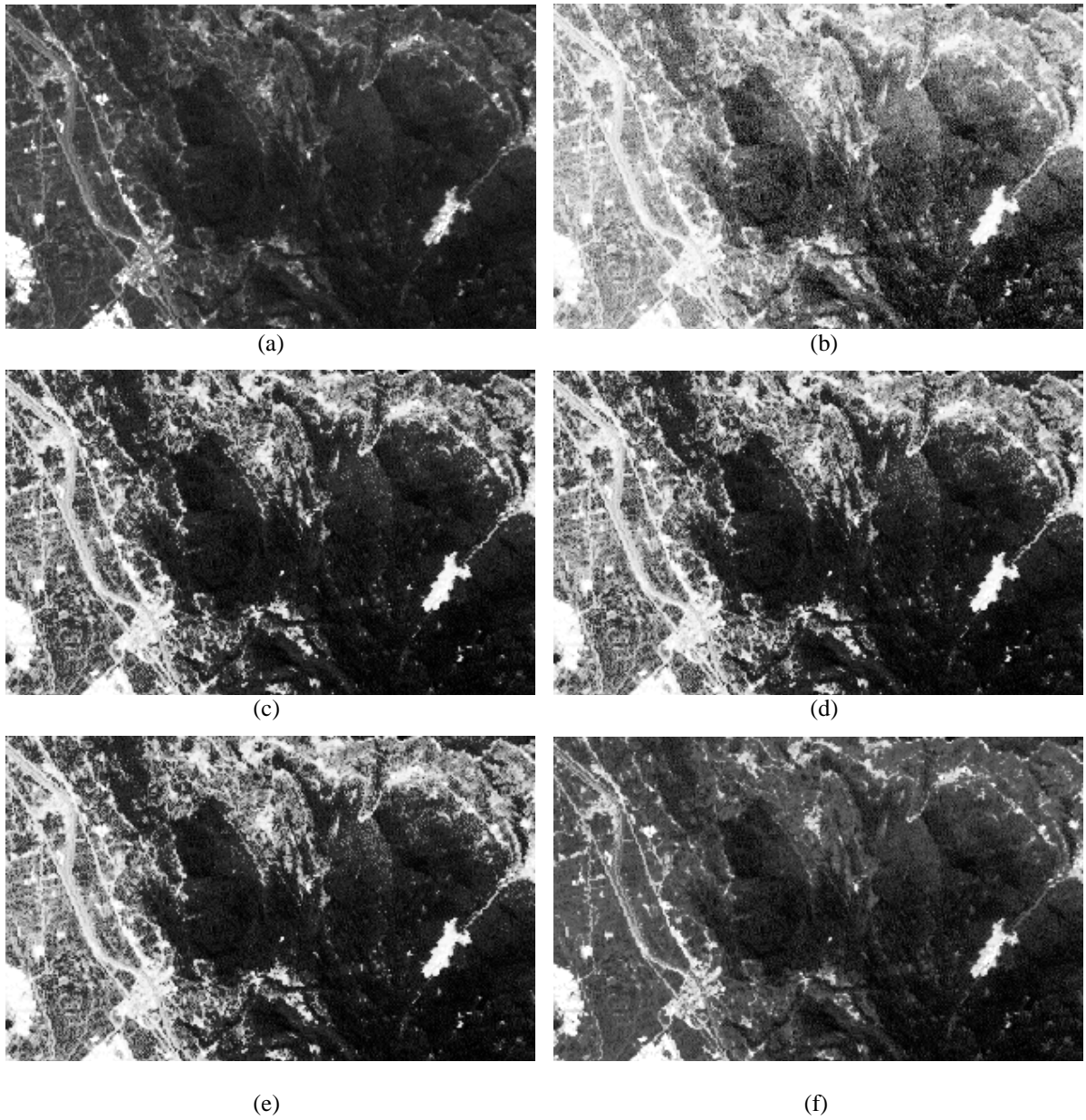


Fig.4.9: Histogram equalization results obtained for channel 1 of the September sub-image. a) Original sub-image. b) HE method. c) BBHE method. d) DSIHE method. e) LFPTCE-ME method. f) LFPTCE-MV method.

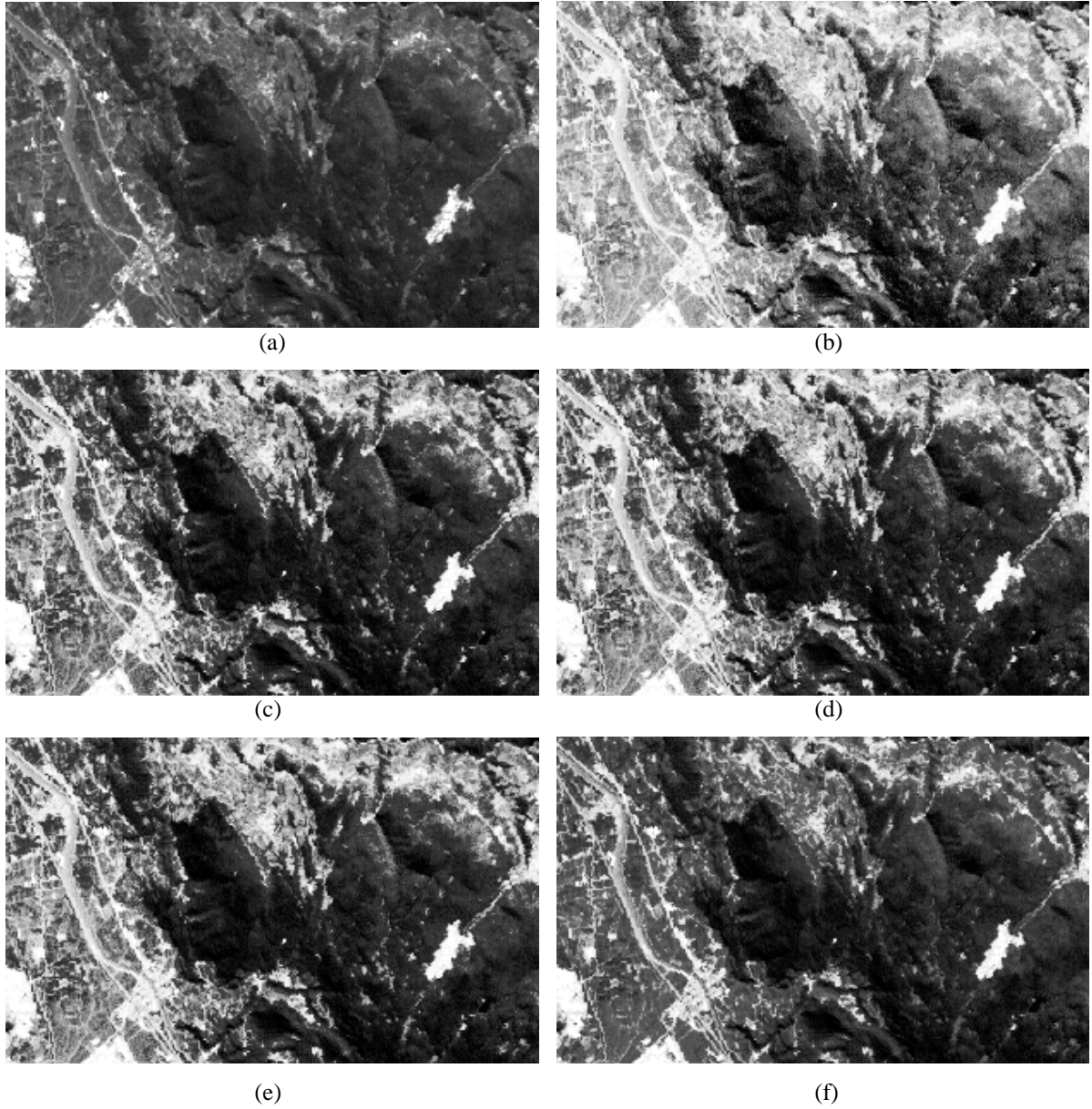


Fig.4.10: Histogram equalization results obtained for channel 2 of the September sub-image. a) Original sub-image. b) HE method. c) BBHE method. d) DSIHE method. e) LFPTCE-ME method. f) LFPTCE-MV method.

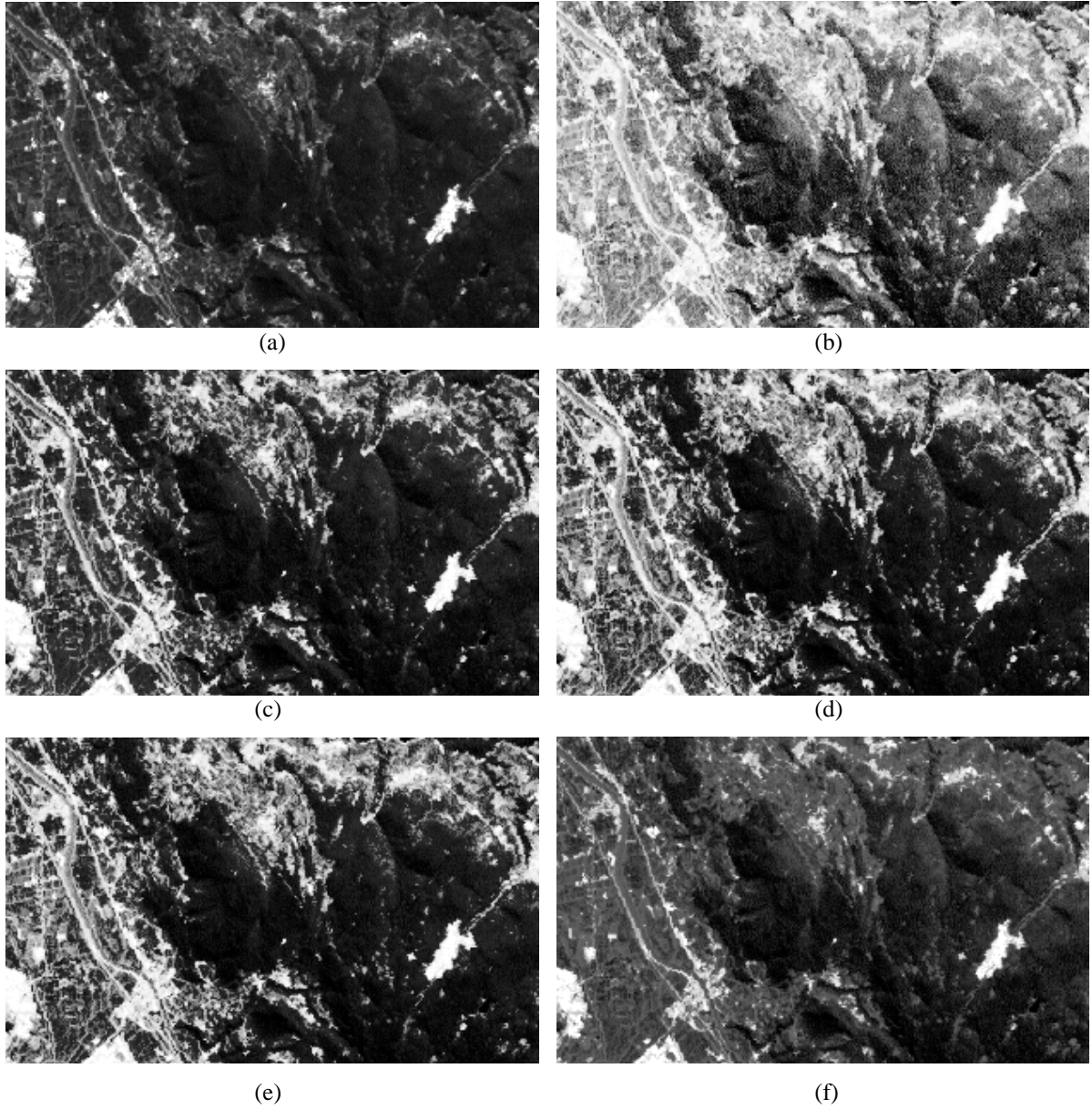


Fig.4.11: Histogram equalization results obtained for channel 3 of the September sub-image. a) Original sub-image. b) HE method. c) BBHE method. d) DSIHE method. e) LFPTCE-ME method. f) LFPTCE-MV method.

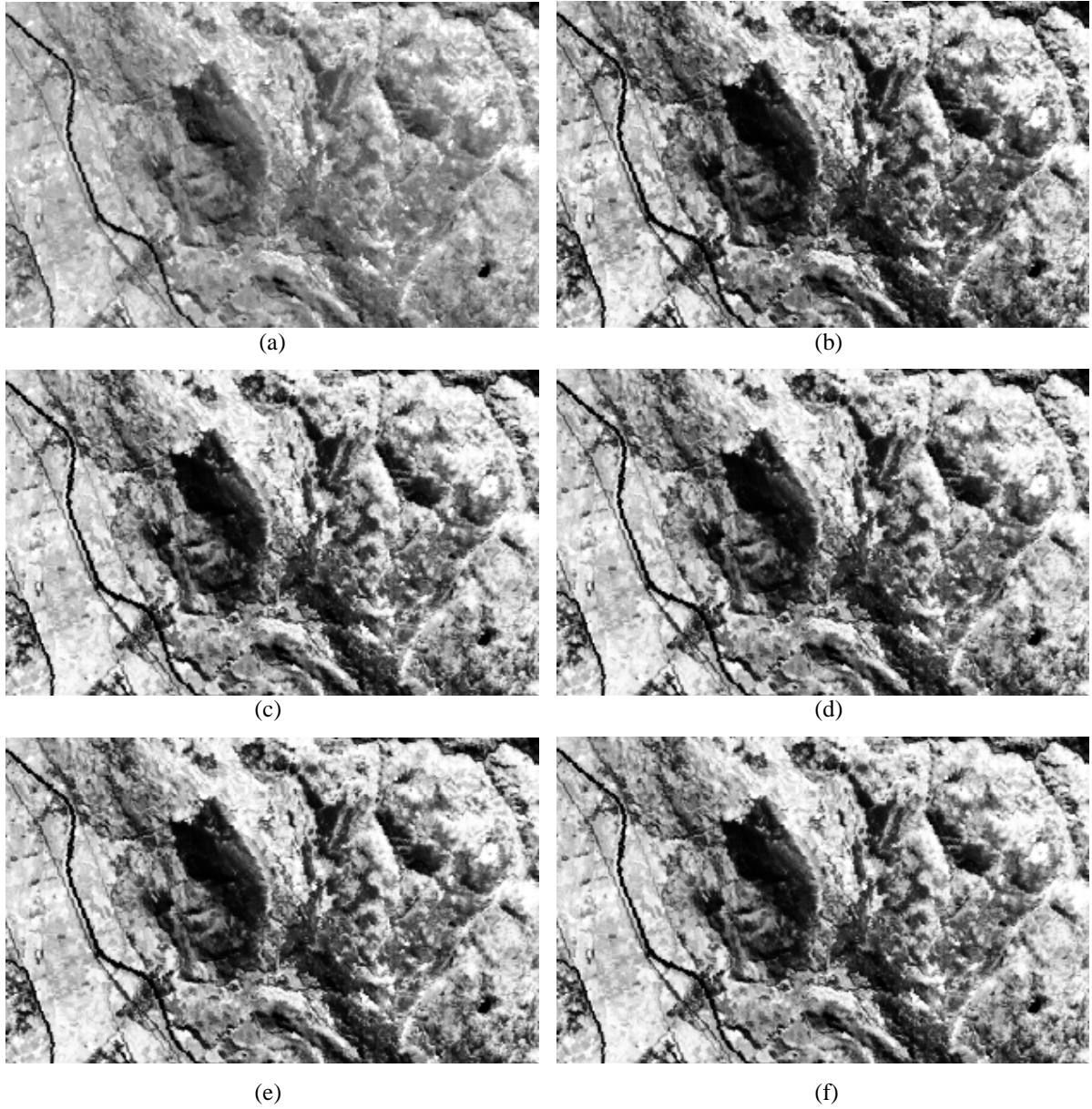


Fig.4.12: Histogram equalization results obtained for channel 4 of the September sub-image. a) Original sub-image. b) HE method. c) BBHE method. d) DSIHE method. e) LFPTCE-ME method. f) LFPTCE-MV method.

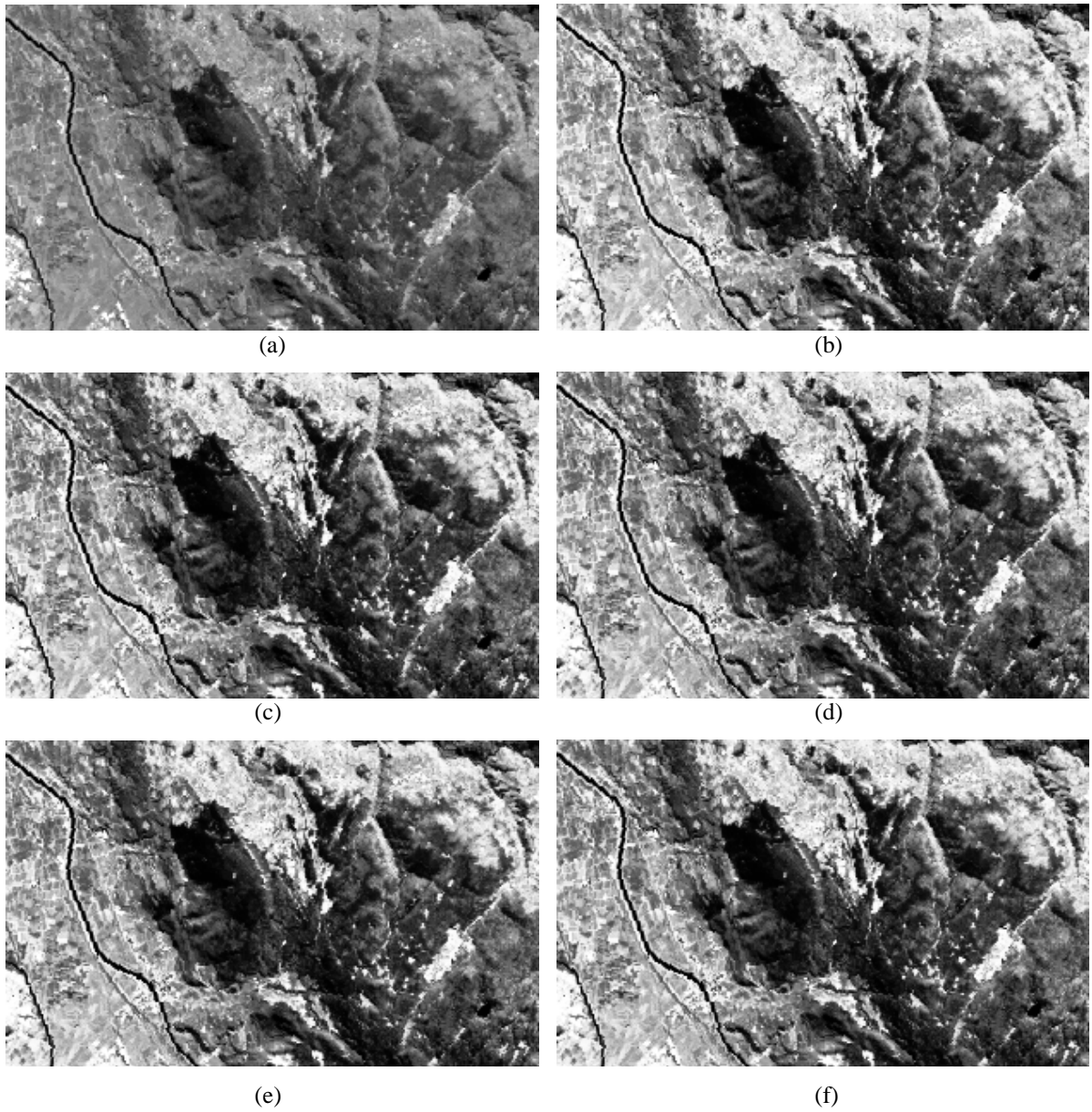


Fig.4.13: Histogram equalization results obtained for channel 5 of the September sub-image. a) Original sub-image. b) HE method. c) BBHE method. d) DSIHE method. e) LFPTCE-ME method. f) LFPTCE-MV method.

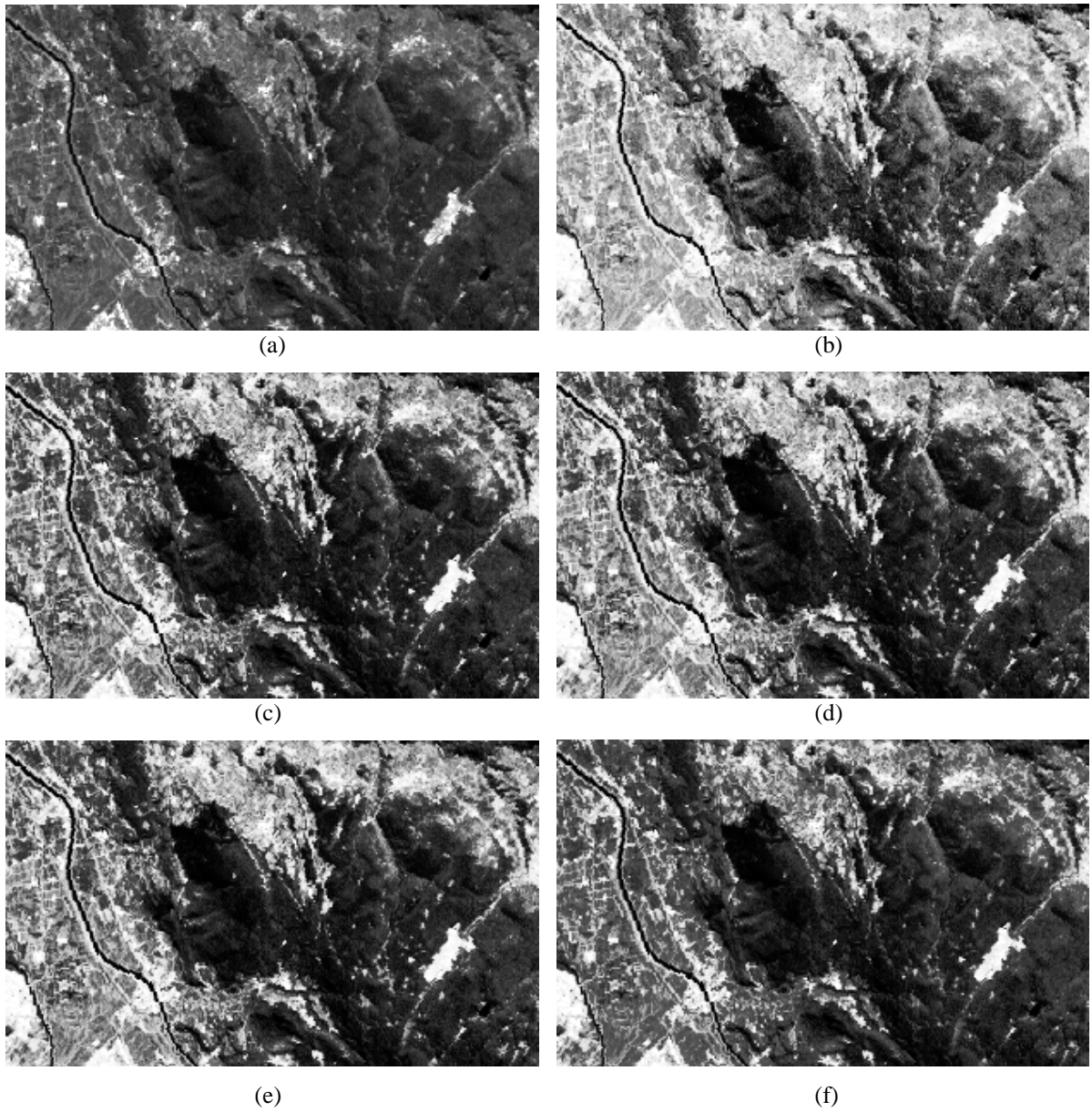


Fig.4.14: Histogram equalization results obtained for channel 7 of the September sub-image. a) Original sub-image. b) HE method. c) BBHE method. d) DSIHE method. e) LFPTCE-ME method. f) LFPTCE-MV method.

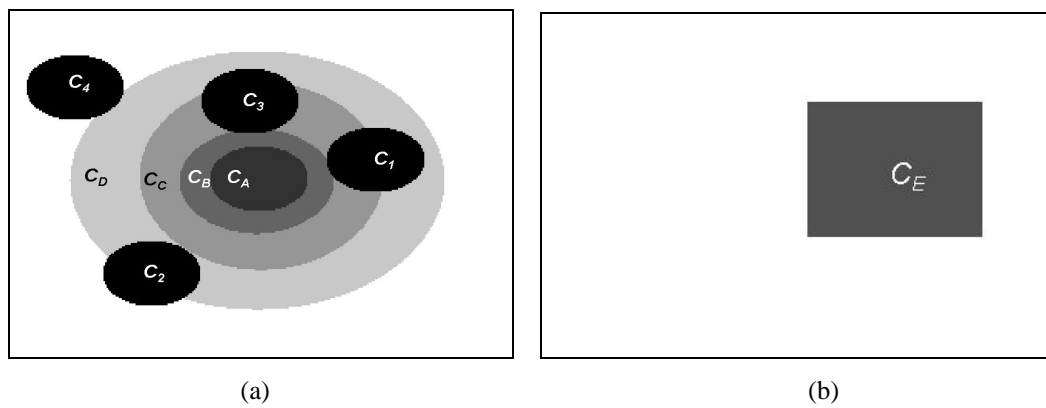


Fig.4.15: Masks adopted to simulate different locations of area C.

Band	Mask	AMBE	Contrast C	Distortion
<b>B1</b>	$C_D$	2.22	164.39	0.04
	$C_C$	3.57	165.60	0.05
	$C_B$	5.80	165.80	0.05
	$C_A$	6.82	165.41	0.06
	$C_I$	6.84	165.43	0.05
	$C_2$	8.11	165.34	0.05
	$C_3$	7.96	164.50	0.05
	$C_4$	7.97	164.55	0.05
	$C_E$	5.39	185.36	0.05

(a)

Band	Mask	AMBE	Contrast C	Distortion
<b>B4</b>	$C_D$	0.77	197.78	0.03
	$C_C$	3.85	200.02	0.03
	$C_B$	5.85	199.61	0.03
	$C_A$	6.69	199.73	0.03
	$C_I$	6.69	233.05	0.07
	$C_2$	6.71	232.89	0.07
	$C_3$	6.39	233.59	0.07
	$C_4$	6.73	232.03	0.07
	$C_E$	6.28	231.14	0.07

(b)

TABLE 4.2. QUANTITATIVE RESULTS OBTAINED FOR CONTEXTUAL SPATIAL HISTOGRAM FOR CONTRAST ENHANCEMENT: AREA C OUTSIDE THE MASKS. (A) RESULTS OF CHANNEL 1. (B) RESULTS OF CHANNEL 4.

Band	Mask	AMBE	Contrast C	Distortion
<b>B1</b>	$C_D$	12.77	166.16	0.09
	$C_C$	20.45	172.92	0.12
	$C_B$	26.36	171.75	0.15
	$C_A$	27.85	167.53	0.15
	$C_I$	4.46	169.32	0.42
	$C_2$	15.29	174.02	0.18
	$C_3$	7.12	188.83	0.19
	$C_4$	14.20	180.33	0.20
	$C_E$	19.22	155.08	0.15

(a)

Band	Mask	AMBE	Contrast C	Distortion
<b>B4</b>	$C_D$	1.68	232.00	0.07
	$C_C$	2.62	220.42	0.05
	$C_B$	4.37	221.15	0.05
	$C_A$	5.52	214.26	0.04
	$C_I$	5.33	237.26	0.08
	$C_2$	4.42	237.49	0.07
	$C_3$	10.57	221.46	0.06
	$C_4$	3.61	261.16	0.12
	$C_E$	7.92	242.59	0.11

(b)

TABLE 4.3. QUANTITATIVE RESULTS OBTAINED FOR CONTEXTUAL SPATIAL HISTOGRAM FOR CONTRAST ENHANCEMENT: AREA C INSIDE THE MASKS. (A) RESULTS OF CHANNEL 1. (B) RESULTS OF CHANNEL 4.

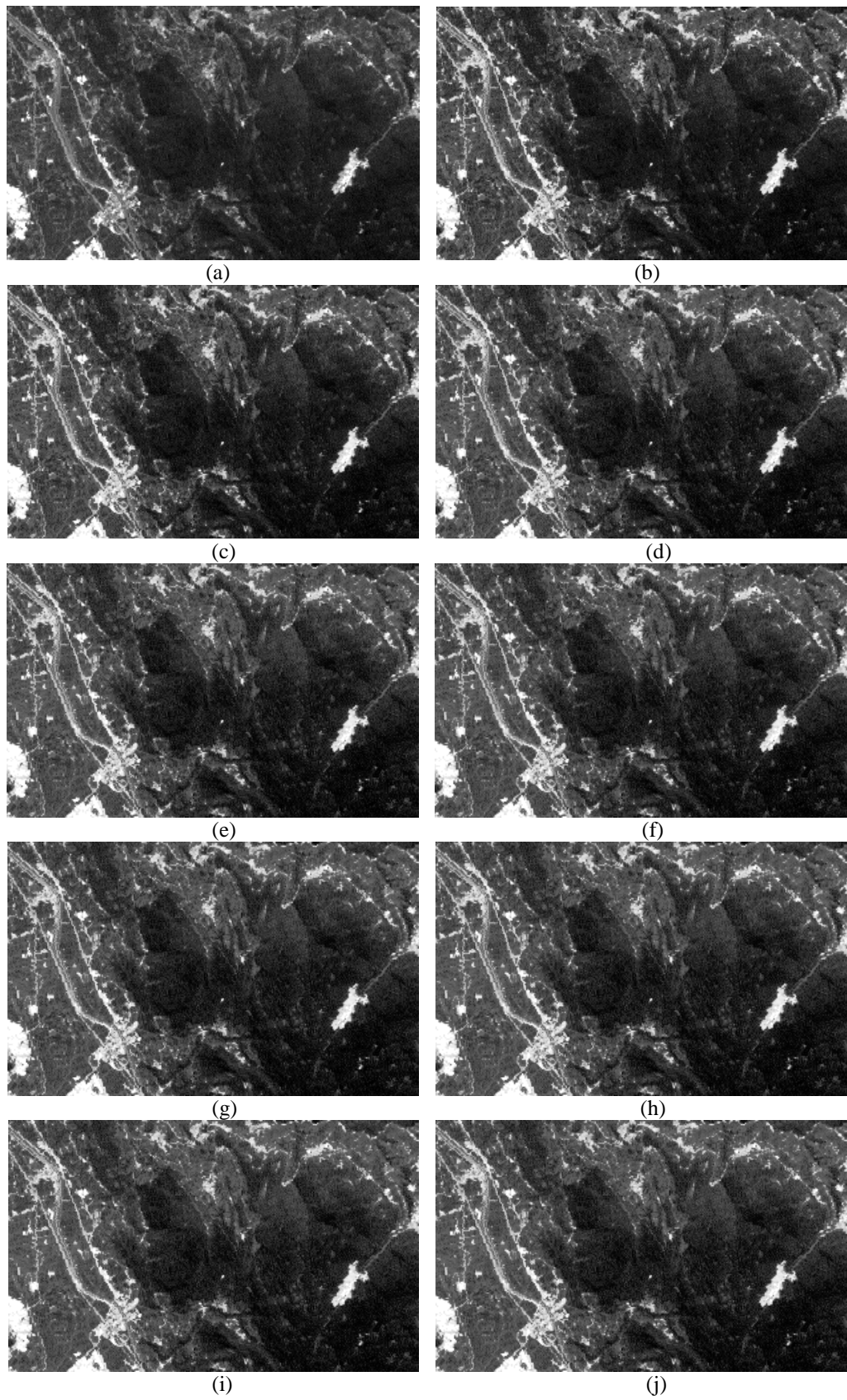


Fig.4.16: Histogram equalization results obtained for channel 1 of the September sub-image with the CSHCE method: Area  $C$  outside the mask. a) Original sub-image. b) Mask  $C_D$ . c) Mask  $C_C$ . d) Mask  $C_B$ . e) Mask  $C_A$ . f) Mask  $C_J$ . g) Mask  $C_2$ . h) Mask  $C_3$ . i) Mask  $C_4$ . j) Mask  $C_E$ .

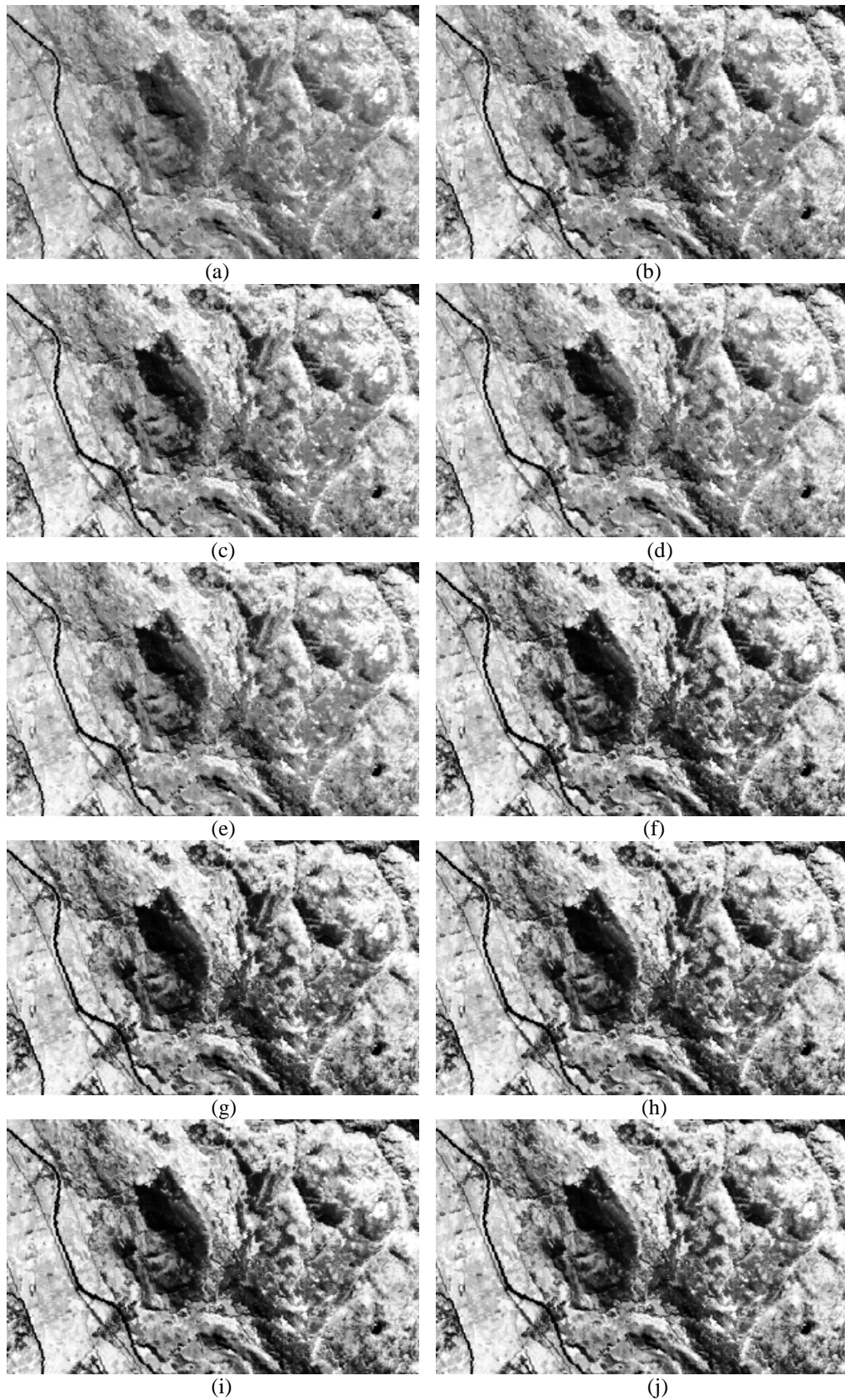


Fig.4.17: Histogram equalization results obtained for channel 4 of the September sub-image with the CSHCE method: Area  $C$  outside the mask. a) Original sub-image. b) Mask  $C_D$ . c) Mask  $C_C$ . d) Mask  $C_B$ . e) Mask  $C_A$ . f) Mask  $C_I$ . g) Mask  $C_2$ . h) Mask  $C_3$ . i) Mask  $C_4$ . j) Mask  $C_E$ .

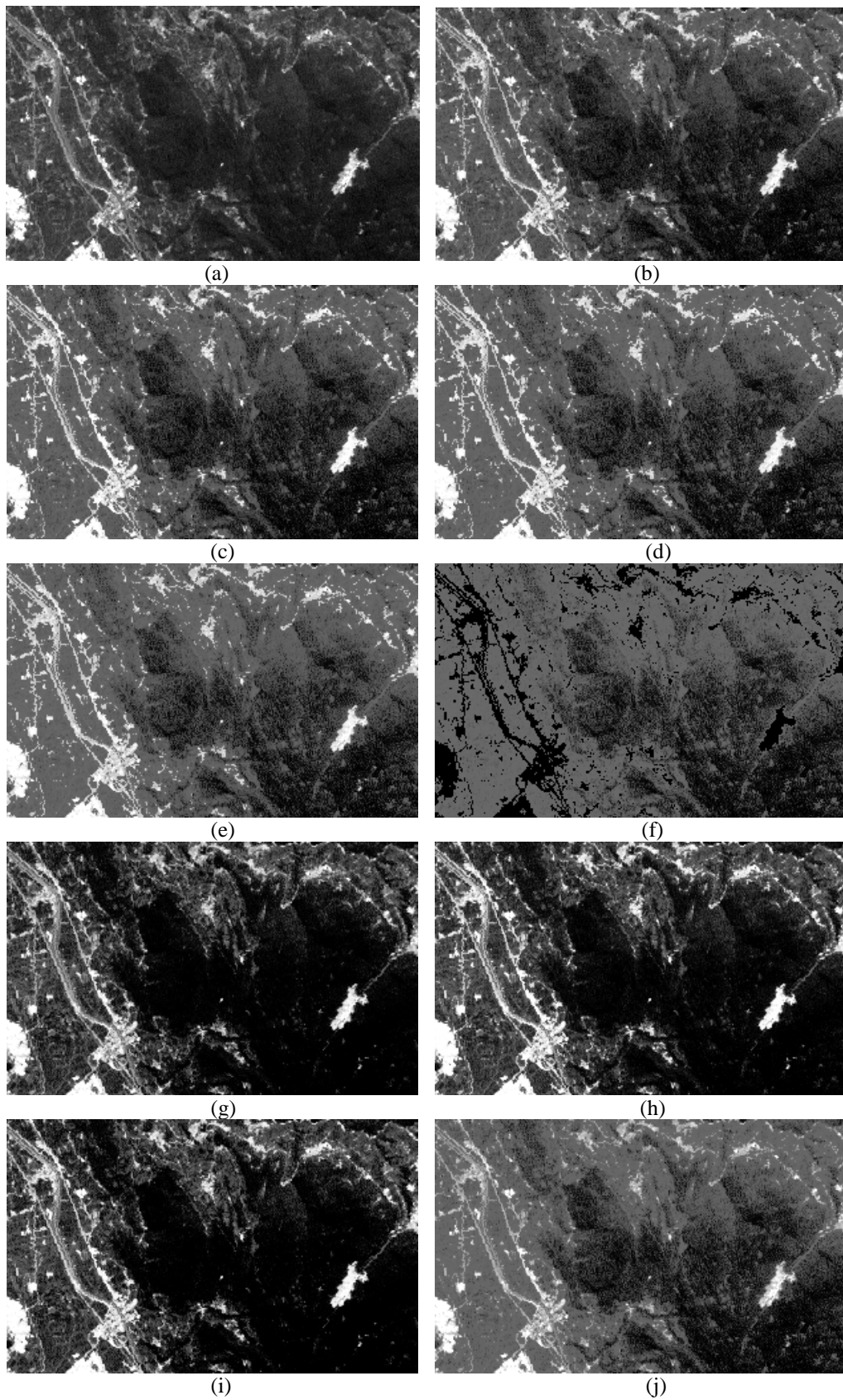


Fig.4.18: Histogram equalization results obtained for channel 1 of the September sub-image with the CSHCE method: Area  $C$  inside the mask. a) Original sub-image. b) Mask  $C_D$ . c) Mask  $C_C$ . d) Mask  $C_B$ . e) Mask  $C_A$ . f) Mask  $C_J$ . g) Mask  $C_2$ . h) Mask  $C_3$ . i) Mask  $C_4$ . j) Mask  $C_E$ .

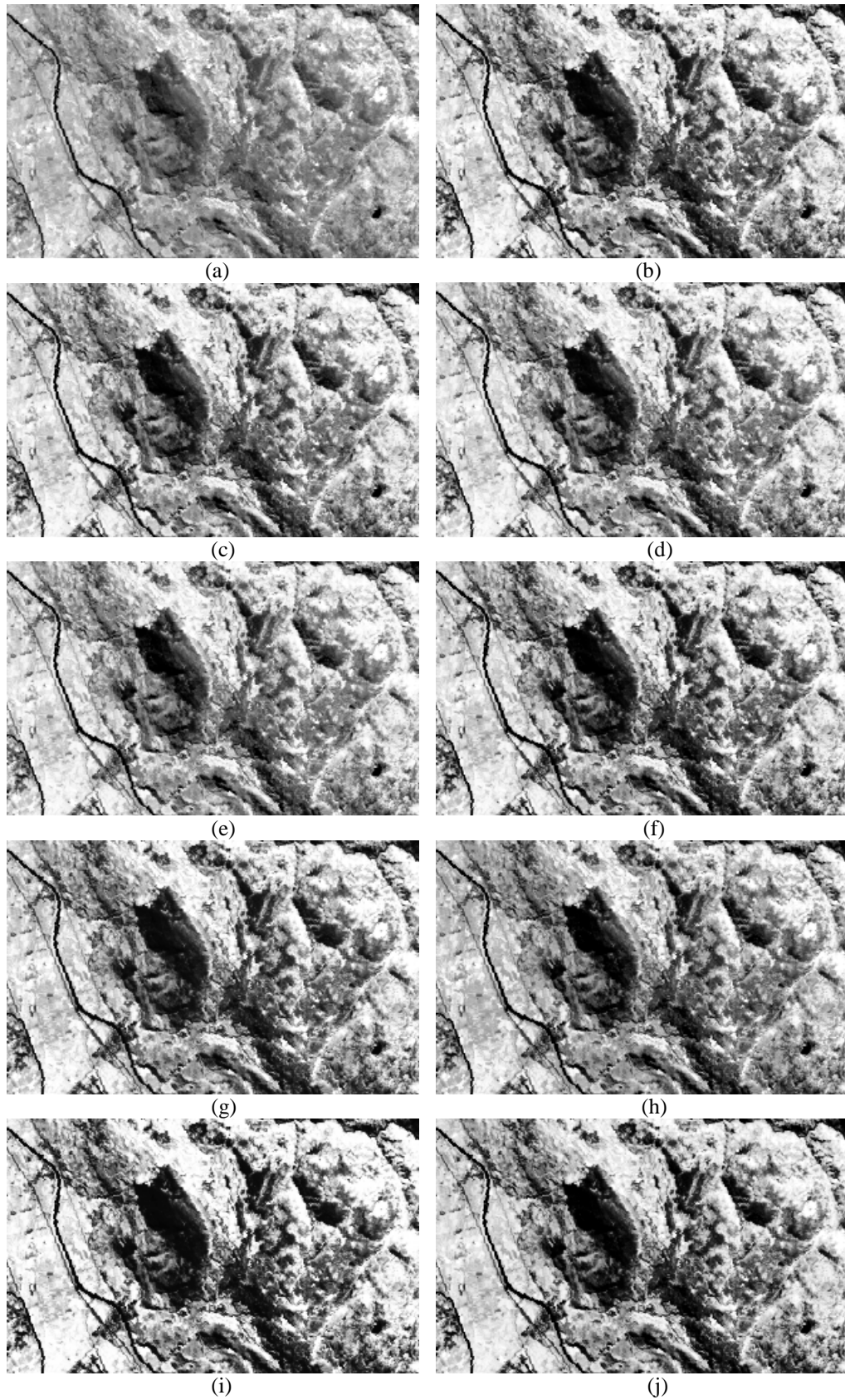


Fig.4.19: Histogram equalization results obtained for channel 4 of the September sub-image with the CSHCE method: Area C inside the mask. a) Original sub-image. b) Mask  $C_D$ . c) Mask  $C_C$ . d) Mask  $C_B$ . e) Mask  $C_A$ . f) Mask  $C_I$ . g) Mask  $C_2$ . h) Mask  $C_3$ . i) Mask  $C_4$ . j) Mask  $C_E$ .

# CONCLUSION

We have addressed two principal applications for remote sensing:

1. The post restoration of cloud-contaminated areas in remote sensing images
2. A contextual spatial contrast enhancement of satellite images.

For the purpose of post-restoration, three methods have been explored. The first uses a multimodal predictor. The second is based on the exploitation of residuals generated by an estimator, and the last one consists in a contextual spatio-spectral post-reconstruction scheme (CSSPR). In all the methods, we have investigated the opportunity of using both spatial and spectral information.

Three different spatial models have been introduced to analyze which of is better adapted to our post-restoration problem. The first model is the common second order neighborhood system. The second is derived from the autobinomial model originally used in the restoration based Markov Random Fields. On the one hand, this model presents the advantage that is more compact than the first model. On the other hand, it raises a weight estimation problem. Finally, the third spatial model is based on the median-type predictor used for isolating transmission errors in predictive coding. This model presents the advantage to be compact and parameters free. The compactness of the second and the third model allowed limiting the dimensionality of the space where the prediction problem was defined.

The following general conclusions can be drawn from the experimental results:

1. Depending on the contamination scenario, either the spectral or the spatial information may appear more valuable;
2. However their fusion is the best way to get higher accuracies, especially when adopting the simple first spatial model.

Nevertheless, when examining each method along with the remaining two others, the residual-based prediction method seems to be the weakest:

1. The gains on MSE are almost low when using the spectral information separately in both sequential and parallel systems;
2. The parallel residual-based system exhibits better gains than the sequential residual-based system when taking into account the spatial information or the fusion of the two information sources;
3. However, the obtained gains with the residual correction process, in the latter case, are comparable to those obtained by the CSSPR and the multimodal predictor. The residual correction process is unable to refine more the results because the generated errors by the CMLP or CNP methods are not systematic.
4. The CSSPR and multimodal predictor show comparable accuracies, however the CSSPR is more tractable since it is modeled more in the spirit of multispectral reconstruction.

5. Finally, the contextual generation of error maps in the CSSPR method provides a mean to deduce helpful indications on the spatial structure of errors and their magnitude.

Post-reconstruction is useful to boost the reconstruction quality. However, the above two steps process may be compressed into a simple but powerful restoration procedure by using more complete models, in particular wavelets and MRFs to allow an improvement in the description of remote sensing images.

For the purpose of contrast enhancement, two novel alternatives to bright preserving contrast enhancement schema have been proposed, namely the LFPTCE and the CSHCE method. The basic thought of our proposed algorithms have been met.

First, the brightness preserving constraint is expressed elegantly and implicitly in the thresholding process, where object regions are extracted from their background on the basis of the similarity of brightness of image objects.

With respect to automatic threshold selection, the fuzzy thresholding method, we have initially developed for single channel gray level images, has proven to be powerful and effective for multispectral images.

The proposed methods increase the brightness preservation and yield a more natural enhancement. They are able to amplify edge contrast without explicitly detecting edge pixels. This is due essentially to the models used by each method to describe the spatial relationships between neighboring pixels and neighboring areas for the CSHCE method.

In the LFPTCE algorithm, the second order derivative metric defined in the spirit of an edge preserving function, provides a local measure of spatial activity within the data and tries to preserve discontinuities. The sorting function enables to preserve image structure by not overly-enhancing image contrast.

In the CSHCE algorithm, the contextual spatial histogram represents a refinement of the histogram in which local information about pixels as well as global histogram information is combined. The introduction of the area neighborhood seems to be attractive for remote sensing images since it is highly related to the land cover and spectral properties of this kind of images.

Both of the two methods, however, suffer from some limitations and give rise to further improvements that can be summarized in:

1. The methods are single channel processing and do not take advantage of the inter-correlation between the different spectral components. One alternative is to consider a multispectral thresholding. Another interesting alternative is to achieve the multispectral contrast enhancement in the spirit of the multispectral restoration based on a Bayesian paradigm, in which spatial and spectral relationships are described using appropriate MRFs.
2. The area of transformation definition in the CSHCE algorithm is determined empirically. The addition of some constraints in the choice of such area would be more valuable.

## Bibliography

- [1] R.C Gonzalez and R.E.Woods, "Digital Image Processing", 2<sup>nd</sup> Ed., *Prentice-Hall, Inc.*, 2002.
- [2] G. Demoment, "Image reconstruction and restoration: overview of common estimation structures and Problems", *IEEE Trans. ASSP*, vol. 37, no. 12, pp. 2024-2036, Dec. 1989.
- [3] M. R. Banham and A. K. Katsaggelos, "Digital image restoration", *IEEE Signal Proces. Mag.*, vol. 4, no. 2, pp. 24-41, Mar. 1997.
- [4] Hadamard, "Lectures on the Cauchy problem in linear partial differential equations", *New Haven CT: Yale Univ. Press*, 1923.
- [5] A. Tikhonov and V. Arsenin, "Solutions of ill-posed problems", *Washington, DC: Winston*, 1977.
- [6] G. Wahba, "Ill-posed problems: numerical and statistical methods for mildly, moderately and severely ill-posed problems with noisy data", in *Proc. Int. Conf. Ill-Posed problems*, Newark, NJ, Oct. 1979.
- [7] H. C. Andrews and B. R. Hunt, "Digital Image Restoration", *Englewood Cliffs, NJ: Prentice-Hall*, 1977.
- [8] H. Chen and G. E. Ford, "Perceptual Wiener filtering for image restoration", *IEEE*, pp. 218-222, 1995.
- [9] C. M. Leung and W.-S. Lu, "A two-step regularization approach for image noise removal", *IEEE*, pp. 856-859, 1995.
- [10] A. Murli, L. D'Amore and V. De Simone, "The Wiener filter and regularization methods for image restoration problems",
- [11] K. J. Boo and N. K. Bose, "Multispectral Image Restoration with Multisensors", *IEEE Trans. on Geosc. Remote Sens.*, vol. 35, no. 5, pp. 1160-1170, Sep. 1997.
- [12] J. Liu, H. Yan, J. Sun and D. Li, "Super-Resolution Image Restoration by Cobining Incremental Wiener Filter and Space-Adaptive Regularization", *IEEE Int. Conf. Neural Networks & Sig. Proces.*, Nanjing, China, Dec. 14-17, pp. 998-1001, 2003.
- [13] W. Li, J. Meunier, and J.-P. Soucy, "A 3D Adaptive Wiener Filter for Restoration of SPECT Images Using MRI as Reference Images", *Proceed. of the 2005 IEEE Engineering in Medicine and Biology 27th Annual Conf.*, Shanghai, China, pp. 3100-3103, Sep. 1-4, 2005.
- [14] B. R. Hunt, "The application of constrained least squares to image restoration by digital computer", *IEEE Trans. Comp. C-22*, pp. 805-812, 1973.
- [15] N. P. Galatsanos and A. K. Katsaggelos, "Methods for choosing the regularization parameter and estimating the noise variance in image restoration and their relation", *IEEE Trans. Image Proc.*, vol. 1, pp. 322-336, 1992.
- [16] H. S. Hou and H. C. Andrews, "Least Squares Image Restoration Using Spline Basis Functions", *IEEE Trans. Comput.*, vol. C-26, no. 9, pp. 856-873, 1977.
- [17] A. Bovik, T. Huang and D. Jr. Munson, "Image restoration using order-constrained least-squares methods", *IEEE Int. Conf. Acous. Speech, and Sig. Proces. ICASSP '83*, vol. 8, pp. 828 – 831, 1983.

- [18] A. Bovik, T. Huang and D. Jr Munson, "Edge-sensitive image restoration using order-constrained least squares methods", *IEEE Trans. Acous., Speech, and Sig. Proc.*, vol. 33, no. 5, pp. 1253 – 1263, 1985.
- [19] N. B. Karayiannis and A. N. Venetsanopoulos, "Regularization theory in image restoration-the stabilizing functional approach", *IEEE Trans. Acous., Speech, and Sig. Proc.*, vol. 38, no. 7, pp. 1155-1179, 1990.
- [20] N. P. Galatsanos, A. K. Katsaggelos, R. T. Chin and A. D. Hillery, "Least squares restoration of multichannel images", *IEEE Trans. Acous., Speech, and Sig. Proc.*, vol. 39, no. 10, pp. 2222-2236, 1991.
- [21] T. Berger, J. O. Stromberg and T. Eltoft, "Adaptive regularized constrained least squares image restoration", *IEEE Trans. Image Proc.*, vol. 8, no. 9, pp. 1191-1203, 1999.
- [22] W.-S Yeoh and C. Zhang, "Constrained Least Squares Filtering Algorithm for Ultrasound Image Deconvolution", *IEEE Trans. Biomedical Engin.*, vol. 53, no. 10, pp. 2001-2007, 2006.
- [23] R. Gordon, R. Bender, and G. T. Herman, "Algebraic reconstruction techniques (ART) for three-dimensional electron microscopy and X-ray photography," *J. Theoret. Biol.*, vol. 29, pp. 471–582, 1970.
- [24] K. Tanabe, "Projection method for solving a singular system of linear equations and its applications," *Numer. Math.*, vol. 17, pp. 203–814, 1971.
- [25] P. P. B. Eggermont, G. T. Herman, and A. Lent, "Iterative algorithms for larger partitioned linear systems, with applications to image reconstruction", *Linear Algebra Appl.*, vol. 40, pp. 37–67, 1981.
- [26] A. H. Andersen and A. C. Kak, "Simultaneous algebraic reconstruction technique (SART): A superior implementation of the ART algorithm," *Ultrasonic Imag.*, vol. 6, pp. 81–94, Jan. 1984.
- [27] Y. Censor, D. Gordon, and R. Gordon, "Component averaging: An efficient iterative parallel algorithm for large and sparse unstructured problems", *Parallel Comput.*, vol. 27, pp. 777–808, 2001.
- [28] Y. Censor and T. Elfving, "Block-iterative algorithms with diagonally scaled oblique projections for the linear feasibility problem," *SIAM J. Matrix Anal. Appl.*, vol. 24, pp. 40–58, 2002.
- [29] M. Jiang and G. Wang, "Convergence studies on iterative algorithms for image reconstruction", *IEEE Trans. Med. Imag.*, vol. 22, no. 5, pp. 569–579, 2003.
- [30] J. Wang and Y. Zheng, "On the convergence of generalized simultaneous iterative reconstruction algorithms", *IEEE Trans. Image Proc.*, vol. 16, no. 1, pp. 1-6, 2007.
- [31] Y. Censor and S. A. Zenios, *Parallel Optimization: Theory, Algorithms and Applications*. New York: Oxford, 1997.
- [32] A. K. Katsaggelos, J. Biemond, R. W. Schafer and R. M. Mersereau, "A regularized iterative image restoration algorithm", *IEEE Trans. Acoust., Speech, Signal Proc.*, vol. 39, pp. 914-929, 1991.
- [33] R. W. Schafer, R. M. Mersereau and M. A. Richards, "Constrained iterative restoration algorithm", *Proc. IEEE*, vol. 69, pp. 432-450, 1981.
- [34] R. L. Lagendijk, J. Biemond and D. E. Boeke, "Regularized Iterative Image Restoration with Ringing Reduction", *IEEE Trans. Acoustics, Speech, Signal Proc.*, vol. 36, no. 12, pp. 1874-1888, 1988.
- [35] A. K. Katsaggelos, "Iterative image restoration algorithm", *Optical Engineering*, vol. 28, no. 7, pp. 735-748, 1989.
- [36] R. L. Lagendijk and J. Biemond, "Iterative identification and restoration of images", Boston Kluwer, 1990.

- [37] Stanley J. Reeves, "Optimal Space-Varying Regularization in Iterative Image Restoration", *IEEE Trans. Image Proc.*, vol. 3, no. 3, pp. 319-324, 1994.
- [38] S.O. Memik, A. K. Katsaggelos and M. Sarrafzadeh, "Analysis and FPGA implementation of image restoration under resource constraints", *IEEE Trans. Comput.*, vol. 52, no. 3, pp. 390-399, 2003.
- [39] P. L. Combettes, "The Foundations of Set Theoretic Estimation", *Proceed. IEEE*, vol. 81, no. 2, pp. 182-208, 1993.
- [40] M. I. Sezan and A. M. Tekalp, "Iterative image restoration with ringing suppression using POCS", *Proc. IEEE Int. Conf. Acoustics, Speech, Sig. Proc.*, pp. 1300-1303, 1988.
- [41] M. K. Ozkan, A. M. Tekalp and M. I. Sezan, "POCS-based restoration of space-varying blurred images", *IEEE Trans. Image Proc.*, vol. 3, no. 4, pp. 450-454, 1994.
- [42] Y. Yang, N. P. Galatsanos and A. K. Katsaggelos, "Projection-based spatially adaptive reconstruction of block-transform compressed images", *IEEE Trans. Image Proc.*, vol. 4, pp. 896-908, 1995.
- [43] D. Schonfeld and Y. Qiao, "A new stochastic projection-based image recovery method", *Proc. IEEE Int. Conf. Image Proc.*, Washington DC, vol. 1, pp. 466-469, 1995.
- [44] F. V. Salina and N. D. A. Mascarenhas, "A hybrid estimation theoretic-POCS method for tomographic image reconstruction", *Proc. of the XVIII Brazilian Symposium on Comp. Graph. Image Proc. (SIBGRAPI'05)*, pp. 220-224, Oct. 2005.
- [45] J. Bonnett and A. Khotanzad, "A maximum likelihood estimation method for multispectral autoregressive image models", *Proceed. Int. Conf. Image Proc.*, vol. 2, pp. 839 - 842, 1997.
- [46] V. Pascazzio and G. Schirinzi, "Multifrequency InSAR height reconstruction through maximum likelihood estimation of local planes parameters", *IEEE Trans. Image Proc.*, vol. 11, no. 12, pp. 1478-1489, 2002.
- [47] D. Huang, N. Fujiyama and S. Sugimoto, "A DST-based maximum likelihood parameter identification and restoration method for noisy blurred image", *6th Int. Conf. Sig. Proc.*, vol. 1, pp. 869 – 872, 2002.
- [48] T. Abatzoglou and P. Convery, "Maximum Likelihood Restoration of Missing Samples in Sinusoidal Data", *Conf. Record of the Thirty-Ninth Asilomar Conf. Sig., Syst. Comput.*, pp. 942 – 945, 2005.
- [49] T. C. Aysal and K. E. Barner, "Rayleigh-Maximum-Likelihood Filtering for Speckle Reduction of Ultrasound Images" *IEEE Trans. Medical Imaging*, vol. 26, no. 5, pp. 712-727, 2007.
- [50] T. K. Moon, "The Expectation – Maximization algorithm", *IEEE Sig. Proc. Mag.*, vol. 13, no. 6, pp. 47-60, Nov. 1996.
- [51] R. L. Lagendijk, J. Biemond and D. E. Boekee, "identification and restoration of noisy blurred images using the Expectation-Maximization algorithm", *IEEE Trans. Acoust., Speech, Signal Proc.*, vol. 38, pp. 1180-11191, 1990.
- [52] K. T. Lay and A. K. Katsaggelos, "Image identification and restoration based on the Expectation-Maximization algorithm", *Optical Engineering*, vol. 29, pp. 436-445, 1990.
- [53] P. L. C. Cheong and S . D. Morgera, "Iterative Methods for Restoring Noisy Images", *IEEE Trans. Acoustics, Speech. and Signal Proces.*, vol. 37. no. 4. pp. 580-585, April 1989.
- [54] A. D. Allen and R. T. Chin, "Iterative Wiener Filters for Image Restoration", *IEEE Trans. Signal Proces.*, vol. 39. no. 8, pp. 1892-1899,. Aug. 1991.

- [55] S. J. Reeves, "Optimal Space-Varying Regularization in Iterative Image Restoration", *IEEE Trans. Image Proces.*, vol. 3, no. 3, pp. 319-324, May 1994.
- [56] R. E. Kalman, "A New Approach to Linear Filtering and Prediction Problems", *Transaction of the ASME—Journal of Basic Engineering*, pp. 35-45, 1960.
- [57] J. Woods and C. H. Radewan, "Kalman Filtering in Two Dimensions", *IEEE Trans. Inform. Theory*, vol. IT-23, no. 4, pp. 473-482, 1977.
- [58] M. S Grewal and A. P. Andrews, "Kalman Filtering Theory and Practice", *Upper Saddle River, NJ USA, Prentice Hall*, (1993).
- [59] A.E.Cetin and A.M.Tekalp, "Robust reduced Update Kalman filtering", *IEEE Trans. Circuits and Systems*, vol.37, no. 1, pp. 155-156, 1990.
- [60] J. B. Burl, "A reduced order extended Kalman filter for sequential images containing a moving object", *IEEE Trans. Image Proc.*, vol. 2, no. 3, pp. 285-295, 1993.
- [61] K. D. Rao, M.N.S. Swamy. and E.I. Plotkin. "Adaptive filtering approaches for color image and video restoration", *IEE Proceed. Vision. Image Signal Proc.*, vol. 150, no. 3, pp. 168-177, 2003.
- [62] K.D. Rao and G. Rajashekhar, "Performance analysis of impulsive noisy image restoration filters", *Indian Institute of Technology, Kharagpur 721302*, pp. 151-156, Dec. 20-22, 2004.
- [63] E. Meinel, "Origins of linear and nonlinear recursive restoration algorithms", *Journal Optical Soc. Amer.*, vol. 3, pp. 787-799, 1986.
- [64] G. Anderson and A. Netravali, "Image restoration based on subjective criterion", *IEEE Trans. Syst., Man, Cybern.*, vol. 6, pp. 845-853, 1976.
- [65] A. Tekalp, J. Woods and H. Kaufman, "A multiple model algorithm for the adaptive restoration of images", *IEEE Int. Conf. on Acoust., Speech, Sig. Proc.*, vol. 8, pp. 832 – 835, Apr. 1983.
- [66] S. Kollias, Y. Boutalis and G. Carayannis, "Fast adaptive identification and restoration of images degraded by blur and noise", *IEEE Int. Symp. Circuits and Systems*, vol. 3, pp. 2073-2076, 1988.
- [67] A. M. Tekalp, H. Kaufman and J. W. Woods, "Edge-adaptive Kalman filtering for image restoration with ringing suppression", *IEEE Trans.Acoust., Speech, Sig. Proc.*, vol. 37, no. 6, pp. 892 – 899, 1989.
- [68] S. Koch, H. Kaufman and J. Biemond, "Restoration of spatially varying blurred images using multiple model-based extended Kalman filters", *IEEE Trans. Image Proc.*, vol. 4, no. 4, pp. 520-523, 1995.
- [69] J. M. B. Dias, T. A. M. Silva and J. M. N. Leitao, "Adaptive restoration of speckled SAR images", *Proceedings, IEEE Int. Geosc. Remote Sens. Symp. (IGARSS'98)*, vol.1, pp. 19–23, 1998.
- [70] S.T. Acton and A. C. Bovik, "Piecewise and local image models for regularized image restoration using cross-validation", *IEEE Trans.Image Proc.*, vol. 8, no. 5, pp. 652 – 665, 1999.
- [71] P. Ishwar and P. Moulin, "Multiple-domain image modeling and restoratio", *Proceed. Int. Conf. Image Proc.*, vol. 1, pp. 362 – 366, 1999.
- [72] G.J. Foster and N. M. Namazi, "Edge adaptive restoration of noisy, blurred images", *Proceed. IEEE Int. Conf. Acoust., Speech, Sig. Proc.*, vol. 3, pp. 1829 – 1832, 2001.
- [73] J. Gutierrez, J. Malo and F. Ferri, "Perceptual regularization functionals for natural image restoration", *Proceed. Int. Conf. Image Proc.*, vol. 2., pp. 989-992, 2003.
- [74] G. Chantas, N. Galatsanos and A. Likas, "Maximum a posteriori image restoration based on a new directional continuous edge image prior", *Proceed. Int. Conf. Image Proc.*, vol. 1, pp. 941-944, 2005.

- [75] G. Sun, J. Dong, A. Yang and J. Wu, "Extraction of interference fringe information based on self-adaptive restoration and clustering via distance histogram", *The Sixth World Congress on Intell. Cont. Automa.*,(WCICA), vol. 2, pp. 10342 – 10346, 2006.
- [76] G. K. Chantas, N. P. Galatsanos, and A. C. Likas, "Bayesian Restoration Using a New Nonstationary Edge-Preserving Image Prior", *IEEE Trans. Image Proc.*, vol. 15, no. 10, pp. 2987 – 2997, 2006.
- [77] N. Kaulgud and U. B. Desai, "Restoration of color images subjected to interchannel blurring", *IEEE Int. Symp. Circuits and Syst.*, vol. 4, pp. 72-75, 1999.
- [78] M. Zhonghua, R. W. Hong and Q. Bin, "A window adaptive hybrid vector filter for color image restoration", *IEEE Int. Conf. on Acoust., Speech, Sig. Proc.*, vol. 3, pp. 205 - 208, 2004.
- [79] M. Zhonghua, R. W. Hong Ren and Q. Bin, "A robust structure-adaptive hybrid vector filter for color image restoration", *IEEE Trans. Image Proc.*, vol. 14, no. 12, pp. 1990-2001, 2005.
- [80] M. Q. Phu, N. Faggian, N and P. Tischer, "An Automatic Color Image Restoration Filter", *Int. Symp. Intell. Sig. Proc. Comm.*, pp. 709-712, 2006.
- [81] M. Q. Phu, P. E. Tischer and H. R. Wu, "Statistical Analysis of Impulse Noise Model for Color Image Restoration", *IEEE/ACIS 6<sup>th</sup> Int. Conf. Comp. Inform. Sci.*, pp. 425-431, 2007.
- [82] L. Bar, A. Brook, N. Sochen and N. Kiryati, "Deblurring of Color Images Corrupted by Impulsive Noise", *IEEE Trans. Image Proc.*, vol. 16, pp. 1101-1111, 2007.
- [83] N.P. Galatsanos, A. K. Katsaggelos, R. T. Chin and A. Hillery, "Two methods for least squares multi-channel image restoration", *IEEE Int. Conf. on Acoust., Speech, Sig. Proc.*, vol. 4, pp. 2509 - 2512, 1991.
- [84] H. S. Jeong, K. P. Joon and G. K. Moon, "Comparison between Wiener and CLS image restoration techniques for multichannel images", *IEEE Asia Pacific Conf. Circuits and Syst.*, pp. 532 – 535, 1996.
- [85] M-C. Hong and T. Stathaki, "A regularized least mean mixed norm multichannel image restoration algorithm", *Proceed. Int. Conf. Image Proc.*, vol. 2, pp. 828 – 832, 1998.
- [86] R. Molina, J. Mateos, A. K. Katsaggelos and M. Vega, M, "Bayesian multichannel image restoration using compound Gauss-Markov random fields", *IEEE Trans. Image Proc.*, vol. 12, no.12, pp. 1642 – 1654, 2003.
- [87] M. Kumar and P. Ramuhalli, "Dynamic programming based multichannel image restoration", *IEEE Int. Conf. on Acoust., Speech, Sig. Proc.*, vol. 2, pp. 609 - 612, 2005.
- [88] M. Meguro, A. Taguchi and N. Hamada, "Data-dependent weighted median filtering with robust motion information for image sequence restoration", *Proceed. Int. Conf. Image Proc.*, vol. 2, pp. 424 – 428, 1999.
- [89] A. Rares, M. J. T. Reinders, J. Biemond and R. L. Lagendijk, "A spatiotemporal image sequence restoration algorithm", *Proceed. Int. Conf. Image Proc.*, vol. 2, pp. II-857 – II-860, 2002.
- [90] A. C. Kokaram, A.C, "On missing data treatment for degraded video and film archives: a survey and a new Bayesian approach", *IEEE Trans. Image Proc.*, vol. 13, no. 3, pp. 397 – 415, 2004.
- [91] J. Boulanger, C. Kervrann and P. Bouthemy, "Space-Time Adaptation for Patch-Based Image Sequence Restoration", *IEEE Trans. Patt. Anal. Mach. Intel.*, vol. 29, no. 6, pp. 1096 – 1102, 2007.
- [92] N. Weir, "Applications of maximum entropy techniques to HST data", *Proc. 3<sup>rd</sup> ESO/ST-ECF Data Analys. Workshop*, pp. 115-129, 1991.
- [93] W. H. Richardson, "Bayesian-based iterative method of image restoration", *Journ. Optical Soc. Amer.*, vol. 62, pp. 55-59, 1972.

- [94] L. B. Lucy, "An iterative technique for the rectification of observed distributions", *The Astronomical Journal*, vol. 79, pp. 745-756, 1974. ""
- [95] A. K. Katsaggelos, M. G. Kang and M. R. Banham "Adaptive regularized restoration algorithms applied to HST images", *Proceed. Second Workshop On the Restoration of HST Images and Spectra*, 1993.
- [96] R. Molina, J. Nunez, F. J. Cortijo and J. Mateos, "Image restoration in astronomy: a Bayesian perspective", *IEEE Signal Processing Magazine*, vol.. 18, no. 2, pp. 11 – 29, 2001.
- [97] J. C. Lee, B. J. Sheu and R. Chellappa, "VLSI neuroprocessor for image restoration using analog computing-based systolic architecture", *Journ. VLSI Sig. Proc.*, vol. 5, pp. 185-199, 1993.
- [98] S. Gendy, G. Kothapalli and A. Bouzerdoum, "A fast algorithm for image restoration using a recurrent neural network with bound-constrained quadratic optimization", *7<sup>th</sup> Australian and New Zealand Intel. Info. Syst. Conf*, pp. 111-115, 2001.
- [99] W. Dianhui, T. Dillon and E. Chang, "Pattern learning based image restoration using neural networks", *Proceed. Int. Joint Conf. Neural Net.*, vol. 2, pp. 1481-1486, 2002.
- [100] M. E. Yüksel, "A hybrid neuro-fuzzy filter for edge preserving restoration of images corrupted by impulse noise", *IEEE Trans. Image Proc.*, vol. 15, no. 4, pp. 928-936, 2006.
- [101] W. Yadong and Z. Hongying, "A novel image restoration algorithm using neural network based on variational PDE model", *Proceed. Int. Conf.Comm., Circuits and Syst.*, vol. 1, pp. 433-436, 2006.
- [102] D. L. Donoho and I. M. Johnstone, "Adapting to unknown smoothness via wavelet shrinkage", *J. Amer. Statist. Assoc.*, vol. 90, no. 432, pp. 1200–1224, Dec. 1995.
- [103] M. S. Crouse, R. D. Nowak, and R. G. Baraniuki, "Wavelet-based signal processing using Hidden Markov models," *IEEE Trans. Sig. Process.*, vol. 46, no. 4, pp. 886–902, Apr. 1998.
- [104] M. Belge, M. E. Kilmer, and E. L. Miller, "Wavelet domain image restoration with adaptive edge-peserving regularity," *IEEE Trans. Image Processing*, vol. 9, pp. 597–608, 2000.
- [105] N. G. Kingsbury, "Complex wavelets for shift invariant analysis and filtering of signals," *J. Appl. Comput. Harmon. Anal.*, vol. 10, no. 3, pp. 234–253, May 2001.
- [106] A. Antoniadis and J. Fan, "Regularized wavelet approximations," *J.Amer. Statist. Assoc.*, vol. 96, pp. 939–967, 2001.
- [107] M. A. T. Figueiredo and R. D. Nowak, "An EM algorithm for wavelet-based image restoration", *IEEE Trans. Image Proc.*, vol. 12, no. 8, pp. 906-916, 2003.
- [108] P. L. Combettes and J.-C. Pesquet, "Wavelet-constrained image restoration," *Int. J. Wavelets, Multires. Inf. Process.*, vol. 2, no. 4, pp. 371–389, Dec. 2004.
- [109] A. Benazza-Benyahia and J.-C. Pesquet, "Building robust wavelet estimators for multicomponent images using Stein's principle", *IEEE Trans. Image Process.*, vol. 14, no. 11, pp. 1814–1830, Nov. 2005.
- [110] Y. Zhu, T. Shen and Y. Cui, "Wavelet Domain Image Restoration Algorithm using Classified Hidden Markov Tree Model", *Proceed. 6th World Congress on Intel. Cont. Automat.*, pp. 9570-9573, China, 2006.
- [111] J. Xu and S. Osher, "Iterative Regularization and Nonlinear Inverse Scale Space Applied to Wavelet-Based Denoising", *IEEE Trans. Image Proc.*, vol. 16, no. 2, pp. 534-544, 2007.
- [112] F. Luisier, T. Blu and M. Unser, "A New SURE Approach to Image Denoising: Interscale Orthonormal Wavelet Thresholding", *IEEE Trans. Image Proc.*, vol. 16, no. 3, pp. 593-606, 2007.

- [113] M. M. Chang, A. M. Tekalp, and A. T. Erdem, "Blur identification using the bi-spectrum", *IEEE Trans. Image Process.*, vol. 39, no. 10, pp. 2323–2325, Oct. 1991.
- [114] S. J. Reeves and R. M. Mersereau, "Blur identification by the method of generalized cross-validation," *IEEE Trans. Image Process.*, vol. 1, no. 7, pp. 301–311, Jul. 1992.
- [115] R. L. Lagendijk, J. Biemond, and B. E. Boeke, "Identification and restoration of noisy blurred images using the expectation-maximization algorithm," *IEEE Trans. Acoust., Speech, Signal Process.*, vol. 38, no. 7, pp. 1180–1191, Jul. 1990.
- [116] D. Kundur and D. Hatzinakos, "A novel blind deconvolution scheme for image restoration using recursive filtering," *IEEE Trans. Signal Process.*, vol. 46, no. 2, pp. 375–390, Feb. 1998.
- [117] D. Biggs and M. Andrews, "Acceleration of iterative image restoration algorithms," *Appl. Opt.*, vol. 36, no. 8, pp. 1766–1775, Mar. 1997.
- [118] A. K. Katsaggelos and K. T. Lay, "Maximum likelihood blur identification and image restoration using the EM algorithm," *IEEE Trans. Signal Process.*, vol. 39, no. 3, pp. 729–733, Mar. 1991.
- [119] B. C. McCallum, "Blind deconvolution by simulated annealing," *Opt. Commun.*, vol. 75, pp. 101–105, 1990.
- [120] D. Kundur and D. Hatzinakos, "Blind image deconvolution", *IEEE Sig. Proc. Magazine*, vol. 13, no. 3, pp. 43-64, 1996.
- [121] G. B. Giannakis and R. W. Heath, Jr., "Blind identification of multichannel FIR blurs and perfect image restoration", *IEEE Trans. Image Process.*, vol. 9, no. 11, pp. 1877-1896, 2000.
- [122] R. Nakagaki and A. K. Katsaggelos, "A VQ-based blind image restoration algorithm", *IEEE Trans. Image Process.*, vol. 12, no. 9, pp. 1044-1053, 2003.
- [123] Y. Liao and X. Lin, "Blind image restoration with eigen-face subspace", *IEEE Trans. Image Process.*, vol. 14, no. 11, pp. 1766-1772, 2005.
- [124] O.V. Michailovich, and D. Adam, "A novel approach to the 2-D blind deconvolution problem in medical ultrasound", *IEEE Trans. Medical Imaging*, vol. 24, no. 1, pp. 86-104, 2005.
- [125] R. Molina, J. Mateos and A. K. Katsaggelos, "Blind deconvolution using a variational approach to parameter, image, and blur estimation", *IEEE Trans. Image Process.*, vol. 15, no. 12, pp. 3715-3727, 2006.
- [126] L. Kovacs and T. Sziranyi, "Focus area extraction by blind deconvolution for defining regions of interest", *IEEE Trans. Patt. Anal. Mach. Intell.*, vol. 29, no. 6, pp. 1080-1085, 2007.
- [127] A. Lopez, R. Molina, A. K. Katsaggelos and J. Mateos, "Spect image reconstruction using compound prior models", *Int. Journ. Patt. Recog. Artific. Intell.*, vol. 16, no. 3, pp. 317-330, 2002.
- [128] S. Do, D. Shin, J.-W. Jeong, T.-S. Kim and K. Z. Marmarelis, "Volterra-type nonlinear image restoration of medical imagery using principal dynamic modes", *IEEE Int. Symp. Biomedical Imaging: Macro to Nano*, vol. 1, pp. 760 – 763, 2004.
- [129] Xin Li; "Patch-based nonlocal denoising for mri and ultrasound images", *IEEE Int. Symp. Biomedical Imaging: Macro to Nano*, pp. 948-951, 2007.
- [130] A. O. Aboutalib and L. M. Silverman, "State space image motion restoration", *IEEE Conf. Decision Cont. including the 12th Symp. Adaptive Proces.*, vol. 12, part 1, pp. 731-738, 1973.
- [131] C. Mungi, N. P. Galatsanos and D. Schonfeld, "On the relation of image restoration and template matching: application to block-matching motion estimation", *Proceed. IEEE Int. Conf. Acoust., Speech, Sig. Proc.*, vol. 4, pp. 2112 – 2115, 1996.

- [132] C. L. Huang, E-L. Chen, P-C. Chung and Y-R. Choo, "Optical flow back-projection for genuine motion vector estimation", *IEEE Int. Conf. Multim. Expo.*, vol. 1, pp. 523 – 526, 2004.
- [133] Y. Yang, N. P. Galatsanos and A. K. Katsaggelos, "Regularized image reconstruction from incomplete block discrete cosine transform data", *IEEE Trans. Circ. Syst. Video Tech.*, vol. 3, pp. 421-432, 1993.
- [134] W. Li, D. Zhang, Z. Liu and X. Qiao, "Fast block-based image restoration employing the improved best neighborhood matching approach", *IEEE Trans. Syst. Man, Cyber.—Part A: Syst. and Hum.*, vol. 35, no. 4, pp. 546-555, 2005.
- [135] B. Fisher, "Digital restoration of Snow White: 120,000 famous frames are back", *Advanced Imaging*, pp. 32-36, 1993.
- [136] R. Cristi and R. Shridar, "A parallel algorithm for image segmentation based on the Gibbs model", in *Proc. 1985 Int. Symp. On Circuits and Systems*, pp. 127, 130.
- [137] S. Geman and D. Geman, "Stochastic relaxation, Gibbs distribution and the Bayesian restoration of images", *IEEE Trans. Patt. Anal. Mach. Intell.*, vol PAMI-6, pp. 721-741, Nov. 1984.
- [138] E. Bratsolis and M. Sigelle, "Fast SAR image restoration, segmentation, and detection of high-reflectance regions", *IEEE Trans. Geosci. Remote Sens.*, vol 41, no. 12, Dec. 2003.
- [139] J. Besag, "On the statistical analysis of dirty pictures", *J. R. Stat. Soc., B*, vol. 48, pp. 259-302, 1986.
- [140] J. Woods, "Two - dimensional discrete Markovian fields", *IEEE trans. Inform. Theory*, vol. IT-18, pp. 232-240, 1972.
- [141] R. Chellappa and R. Kashyap, "Texture synthesis using 2-D noncausal autoregressive model", *IEEE Trans. Acoust. Speech Sig. Proc.*, vol. ASSP-33, Feb. 1985.
- [142] P. S. Cohen, "Markov Random Fields for image modeling and analysis", in *Modeling and Applications of Stochastic Processes*, U. B. dessai, ed. Boston: Kluwer, 1986.
- [143] B. R. calder, L. M. Linnett and D. R. Carmichael, "Constrained image restoration with a multinomial prior", in *Proc. 1997 IEEE Int Conf. on Image Proc.*, vol.1, pp. 259 - 262 .
- [144] B. R. Hunt, D. Dekruger, "Bayesian restoration of millimeter wave imagery", in *Proc., IEEE Int Conf. Acoust. Speech Sig. Proc., ICASSP*, vol. 5, pp. 549-552, Apr. 1994.
- [145] E. Isaacson and H. Keller, "Analysis of numerical methods", Wiley, 1958.
- [146] M. Datcu, K. Seidel and M. Walessa, "Spatial retrieval from remote-sensing images \_ Part I: Infromation theoretical perspective", *IEEE Trans. Geosci. Remo. Sens.*, vol. 36, no. 5, Sept. 1998.
- [147] E. Jaynes, "On the rationalof Maximum Entropy methods", *Proceedings of the IEEE*, pp. 936-952, 1982.
- [148] J. Skilling and S. F. gull, "Algorithms and applications", in *C.R Smith and W. T. grandy editors, Maximum Entropy and Bayesian methods in inverse problems*, pp. 83-132, *Kluwer academic publishers*, Boston, 1985.
- [149] A. M. Djafari and G. Demoment, "Maximum entropy and Bayesian approach in tomographic image reconstruction and restoration", in *J. Skilling editors, Maximum Entropy and Bayesian methods in inverse problems*, pp. 195-201, *Kluwer academic publishers*, Boston, 1989.
- [150] M. Willis, B. D. Jeffs and D. G. Long, "A new look at Maximum Entropy image reconstruction", *Record of the thirty-third Asilomar. Conf. on Sign. Syst. And Comput*, vol. 2, pp. 1272-1276, 1999.
- [151] M. lievin, F. Luthon and E. Keeve, "Entropic estimation of noise for medical volume restoration", in *Proc., IEEE 16<sup>th</sup> Int. Conf. on Patt. Recogn.*, vol. 3, pp. 871-874, 2002.

- [152] C. Xi, Z. Hong, W. Chao and W. Tao, "Bayesian restoration of High Resolution SAR imagery with Gauss-Markov Random Fields", in Proc., *IEEE Int. Geosci. Rem. Sens. Symp., IGARSS*, vol. 5, pp. 4648-4650, 2005.
- [153] A. Jalobeanu, L. B. Feraud and J. Zerubia, "An adaptive Gaussian model for satellite image deblurring", *IEEE Trans. Image Proc.*, vol. 13, no. 4, Apr. 2004.
- [154] A. Jalobeanu, L. B. Feraud and J. Zerubia, "Adaptive parameter estimation for satellite image deconvolution", *INRIA Res., Rep. 3956*, [Online] [www.inria.fr/RRRT/RR-3956.html](http://www.inria.fr/RRRT/RR-3956.html), Jun. 2000.
- [155] A. Jalobeanu, L. B. Feraud and J. Zerubia, "Hyperparameter estimation for satellite image restoration using a MCMC maximum likelihood method", *Pattern Recognit.*, vol. 35, no. 2, pp. 341-352, 2002.
- [156] A. Jalobeanu, L. B. Feraud and J. Zerubia, "Satellite image deblurring using complex wavelet packets", *Int. J. Comput., Vis.*, vol. 51., no. 3, pp. 205-217, 2003.
- [157] S. Saquib, C. Bouman and K. Sauer, "A nonhomogeneous MRF model for multiresolution Bayesian estimation", in Proc. *IEEE Int. Conf. Image Proc. (ICIP)*, 1996.
- [158] G. Cowan, "Statistical data analysis", Clarendon Press – Oxford, 1998.
- [159] H. A. Chipman, E. D. Kolaczyk and R. E. McCulloch, "Adaptive Bayes wavelet shrinkage", *J. Amer. Statist., Assoc.*, vol. 92, pp. 1413-1421, 1997.
- [160] P. Moulin and J. Liu, "Analysis of multiresolution image denoising schemes using generalized Gaussian and complexity priors", *IEEE Trans. Inform. Theory*, vol. 45, pp. 909-919, Apr. 1999.
- [161] E. P. Simoncelli and E. H. Adelson, "Noise removal via Bayesian wavelet coring", in Proc. *Third IEEE Int. Conf. Image Proc. (ICIP)*, Lausanne, Switzerland, pp. 379-382, 1996.
- [162] M. Malfait and D. Roose, "Wavelet-based image denoising using a Markov Random Field a priori model", *IEEE Trans. Image Proc.*, vol. 6, no. 4, Apr. 1997.
- [163] A. Pizurica, W. Philips, I. Lemahieu and M. Acheroy, "A joint inter- and intrascale statistical model for Bayesian wavelet based image denoising", *IEEE Trans. Image Proc.*, vol. 11, pp. 545-557, May 2002.
- [164] Y.Q. Cui and K. Wang, "Markov Random Field modelling in the wavelet domain for image denoising", in Proc. *Fourth Int. Conf. Machine Learning Cybernetics*, Guangzhou, Aug. 2005.
- [165] M. Belge and E. Miller, "Wavelet domain image restoration using edge preserving prior models", in Proc. *IEEE Int. Conf. Image Proc. (ICIP)*, vol. 2, pp. 103-107, Oct. 1998.
- [166] C. Bouman and K. Sauer, "A Generalized Gaussian image model for edge preserving MAP estimation", *IEEE Trans. Image Proc.*, vol. 2, no. 3, pp. 296-310, Jul. 1993.
- [167] P. C. Hansen, "Analysis of discrete ill-posed problems by means of the L-curve", *SIAM Review*, vol. 34, pp. 561-580, 1992.
- [168] H. Xie, L. E. Pierce and F. T. Ulaby, "Spatially adaptive radar speckle reduction using wavelet denoising and markov random fields", *IEEE Int. Geosci. Rem. Sens. Symp. (IGARSS)*, vol. 3, pp. 1499-1502, 2001.
- [169] J. Besag, "Statistical analysis of non-lattice data", *The Statistician*, vol. 24, pp. 179-195, 1975.
- [170] F. Forbes and N. Peyrard, "Hidden Markov random Field model selection criteria based on mean field-like approximations", *IEEE Trans. Patt. Recogn. Mach. Intell (PAMI)*, vol. 25, no. 9, pp. 1089-1101, Sep. 2003.

- [171] F. Jeng and J. Woods, "Image estimation by stochastic relaxation in the Compound Gaussian case", in *Proc. IEEE Int. Conf. Acoust, Speech and Sig. Proc.-ICASSP'88*, pp. 1016-1019.
- [172] F. Jeng and J. Woods, "Compound Gauss-Markov Random Fields for image estimation", *IEEE Trans. Sign. Proc.*, vol. 39, pp. 683-697, 1991.
- [173] C. Srinivas and M. D. Srinath, "Compound Gauss Markov Random Field model for image segmentation and restoration", in *Proc. Int. Conf. on Acous. Speech Sign. Proc. (ICASSP)*, vol. 3, pp. 1586-1589, 1989.
- [174] T. Simchony, T. Chellappa and Z. Lichtenstein, "The graduate non convexity algorithm for image estimation using Compound Gauss Markov Field model", in *Proc. IEEE Int. Conf. Acoust, Speech and Sig. Proc.-ICASSP*, pp.1417-1420, 1989.
- [175] T. Simchony and R. Chellappa, "Relaxation algorithms for MAP estimation of grey-level images with multiplicative noise", *IEEE Trans. On Inform. Theory*, vol. 36, no. 3, May 1990.
- [176] D. Geiger and F. Girosi, "Parallel and deterministic algorithms from MRF's: Surface reconstruction", *IEEE Trans. Patt. And Machine Intell.*, vol. 13, pp. 401-412, 1991.
- [177] M. R. Bhatt and U. B. Desai, "Robust image restoration algorithm using Markov Random Field model", in *Proc., IEEE Int. Symposium on Circuits and Syst. (ISCAS)*, vol. 5, pp. 2473-2476.
- [178] V. E. Johnson, W. H. Wong, X. Hu and C. Chen, "Image restoration using Gibbs priors: Boundary modelling, treatment of blurring and selection of hyperparameter", *IEEE Trans. Patt. Recogn. Mach. Intell (PAMI)*., vol. 13, no. 5, May 1991.
- [179] D. Geman and G. Reynolds, "Constrained restoration and recovery of discontinuities", *IEEE Trans. Patt. Recogn. Mach. Intell (PAMI)*., vol 16, no. 3, 1992.
- [180] J. Zerubia and R. Chellappa, "Mean field annealing using Compound Gaussian Markov Random Fields for edge detection and image estimation", *IEEE Trans. Neural Networks*, vol. 4, pp. 703-709, 1993.
- [181] T. J. Herbert and K. Lu, "Expectation-Maximization algorithms, null spaces, and MAP image restoration", *IEEE Trans. Image Proc.*, vol. 4, no. 8, Aug. 1995.
- [182] K. Hara, H. B. Zha and T. Nagata, "Curve and surface reconstruction by using sequential Markov Random Fields", in *Proc., IEEE Int. Conf. on Syst. Man and Cyber., "Intelligent Systems for the 21<sup>st</sup> Century"*, vo. 2, pp. 1097-1102, 1995.
- [183] S. G Nadabar and A. K. Jain, "Parameter estimation in Markov random Field contextual models using geometric models of objects", *IEEE Trans. Patt. Analys. And Mach. Intell.*, vol. 18, no. 3, Mar. 1996.
- [184] M. A. T. Figueiredo and J. M. N. Leitao, "Unsupervised image restoration and edge location using Compound Gauss-Markov Random fields and the MDL principle", *IEEE Trans. Image Proc.*, vol. 6, no. 8, Aug. 1997.
- [185] P. Charbonnier, L. Blanc Feraud, G. Aubert and M. Barlaud, "Deterministic edge-preserving regularization in computed imaging", *IEEE Trans. Image Proc.*, vol. 6, no. 2, pp. 298-311, 1997.
- [186] Z. Zhou, R. M. Leahy and J. Qi, "Approximate maximum likelihood hyperparameter estimation for Gibbs priors", *IEEE Trans. Image Proc.*, vol. 6, no. 6, pp. 844-861, 1997.
- [187] K. Achour, N. Zenati and H. laga, "Contribution to image and contours restoration", *Real-Time Imaging*, vol. 7, pp. 315-326, 2001.
- [188] A. Jalobeanu, L. B. Feraud and J. Zerubia, "Hyperparameter estimation for satellite image restoration using a MCMC maximum-likelihood method", *Pattern Recognition*, vol. 35, pp. 341-352, 2002.

- [189] S. Kirkpatrick, C. D. Gelatt Jr. and M. P. Vecchi, "Optimization by Simulated Annealing", *Science*, 220: pp. 671-680, 1983.
- [190] A. Blake and A. Zisserman, "Visual reconstruction", *Cambridge MA: MIT Press*, 1987.
- [191] G. Winkler, "Image analysis, Random Fields and dynamic Monte Carlo methods", no. 27 in *Applications of Mathematics*, Springer, 1995.
- [192] Z. Kato, J. Zerubia and M. Berthod, "Image classification using Markov Random Fields with two new relaxation methods: Deterministic Pseudo Annealing and Modified Metropolis Dynamics", *Rapport de recherch  de l'INRIA – Sophia Antipolis, Equipe : PASTIS. F v. 1992*.
- [193] A. Waks, O. J. Tretiak and G. K. gregoriou, "Restoration of noisy regions modelled by noncausal Markov Random Fields of unknown parameters", in *Proc., IEEE 10th Int. Conf. on Patt. Recogn.*, vol. 2, pp. 170-175, 1990.
- [194] Luiz W. P. Biscainho, "AR Model Estimation From Quantized Signals", *IEEE Signal Processing Letters*, vol. 11, no. 2, pp. 183-185, Feb. 2004
- [195] R. L. Kashyap and R. Chellappa, "Estimation and choice of neighbours in spatial interaction models of images", *IEEE Trans. On Infor. Theory*, vol. 29, pp. 60-72, Jan. 1983.
- [196] B. D. jeffs, S. Hong and J. Christou, "A Generalized Gauss Markov model for space objects in blind restoration of adaptive optics telescope images", in *Proc., IEEE Int. Conf.. Image Proc. (ICIP)*, vol. 3, pp. 737-741, 1998.
- [197] H. Jinchi, T. Simchony and R. Chellappa, "Stochastic relaxation for map restoration of Gray level images with multiplicative noise", in *Proc. Int. Conf. on Acous. Speech Sign. Proc. (ICASSP)*, vol. 12, pp.1236-1239, 1987.
- [198] Y. Li and F. Santosa, "A computational algorithm for minimizing total variation in image restoration", *IEEE Trans. on Image Processing*, vol. 5, no. 6, June 1996
- [199] R. Chen and T. Li, "Blind restoration of linearly degraded discrete signals by Gibbs sampling", *IEEE Trans. Sign. Proc.*, vol. 43, no. 10, pp. 2410-2413, 1995.
- [200] A. Doucet and X. Wang, "Monte Carlo methods for signal processing: a review in the statistical signal processing context", *IEEE Sign. Process. Mag.*, vol. 22, no. 6, pp. 152-170, Nov. 2005.
- [201] W. Pieczynski, "Pairwise Markov Chains", *IEEE Trans. Patt. Analys. And Mach. Intell.*, vol. 25, no. 5, pp. 634-639, May 2003.
- [202] P. Lanchantin and W. Pieczynski, "Unsupervised restoration of Hidden nonstationary Markov Chains using evidential priors", *IEEE Trans. Sign. Process.*, vol. 53, no. 8, pp. 3091-3098, Aug.. 2005.
- [203] B. Zhang, M. N. Shirazi and H. Noda, "Blind restoration of degraded binary Markov Random Field images", *Graph. Models and Image Process.*, vol. 58, no. 1, pp. 90-98, Jan. 1996.
- [204] J. Zhang,"The mean field theory in EM procedures for blind Markov Random Field image restoration", *IEEE Trans. Image Proc.*, vol. 2, no. 1, pp. 27-40, 1993.
- [205] C. Wu and P. C. Doerschuk, "Computation of Bayesian estimators for Markov Random Field image models using the cluster approximation", in *Proc., IEEE Int. Conf.. Image Proc. (ICIP)*, vol. 3, pp. 172-176, 1994.
- [206] J. Zhang and G. G. Hanuauer, "The application of mean field theory to image motion estimation", *IEEE Trans. Image Proc.*, vol. 4, no. 1, pp. 19-33, 1995.
- [207] J. Wei and Z. Li, "An efficient two-pass MAP-MRF algorithm for motion estimation based on mean field theory", *IEEE Trans. Circ., Syst.for Video tech.*, vol. 9, no. 6, pp. 960-972, 1999.
- [208] Y. Peng and M. Jin, "A mean field approach to MAP in belief networks", in *Proc., IEEE-INNS-ENNS Int. Joint Conf.. Neural Networks (IJCNN)*. vol. 5, pp. 24-27, 2000.

- [209] C. Wu and P. C. Doerschuk, "Application of the cluster approximation for the simultaneous restoration and segmentation of tomographic images", in *Proc., IEEE Int. Conf. Image Proc. (ICIP)*, vol. 2, pp. 449-452, 1995.
- [210] C. Wu and P. C. Doerschuk, "Cluster expansions for the deterministic computation of Bayesian estimators based on Markov random Fields", *IEEE Trans. Patt. Analys. And Mach. Intell.*, vol. 17, no. 3, pp. 275-293, May 2003.
- [211] G. sebastiani and P. Barone, "Truncation artefact reduction in magnetic resonance imaging by Markov Rnandom Field methods", *IEEE Trans. Medical Imaging*, vol. 14, no. 3, pp. 434-441, Sept. 1995.
- [212] N. Vilain, Y. Goussard, S. Brette and J. Idier, "Computed Tomography image restoration using convex-potential 3-D Markov random Fields", in *Proc., 19th Int. Conf.- IEEE/EMBS*, 1997.
- [213] N. Vilain, Y. Goussard, S. Brette and J. Idier, "Three-Dimensional edge preserving image enhancement Computed Tomography ", *IEEE Trans. Medical Imaging*, vol. 22, no. 10, pp. 1275-1287, Oct. 2003.
- [214] J. Idier, "Convex half-quadratic criteria and interacting auxiliary variables for image restoration", *IEEE Trans. Image Proc.*, vol. 10, no. 1, pp. 1001-1009, 2001.
- [215] J. H. Hokland and P. A. Kelly, "Markov model of specular an diffuse scattering in restoration of medical UltraSound images", *IEEE Trans. On Ultrason., Ferroelec., Freq., Cont.*, vol. 43, no. 4, pp. 660-669, Jul. 1996.
- [216] C. Kao, X. Pan and C. Chen, "A Bayesian approach for edge detection in medical UltraSound images", *IEEE Trans. on Nuclear Science*, vol. 45, no. 6, pp. 3089-3096, Dec. 1998.
- [217] C. Chen, V. E. Johnson, W. H. Wong, X. Hu and C. E. Metz, "Bayesian image reconstruction in positron emission tomography", *IEEE Trans. on Nuclear Science*, vol. 37, pp. 636-641, Dec. 1998.
- [218] V. E. Johnson, W. H. Wong, X. Hu and C. T. Chen, "Image restoration using Gibbs priors: Boundary modelling treatment of blurring and selection of hyperparameters", *IEEE Trans. Patt. Analys. And Mach. Intell.*, vol.13, no. 3, pp. 413-425, 1991.
- [219] A. M. Djafari, "Bayesian approach with hierarchical Markov modelling for data fusion in image reconstruction applications", in *Proc., 5<sup>th</sup> IEEE Int. Conf. on Info. Fusion*, vol. 1, pp. 440-447, 2002.
- [220] A. M. Djafari, "Probabilistic methods for data fusion", in *Maximum Entropy and Bayesian methods*, Boise, ID, Aug. 1997.
- [221] S. Gautier, G. Le Besnerais, A. M. Djafari and B. Lavayssiere, "Data fusion in the field of non destructive testing », in *Maximum Entropy and Bayesian methods*, Kluwer Academic Publ., Santa Fe, NM, K. Hanson ed., 1995.
- [222] R. R. Schultz and R. L. Stevenson, "Stochastic modelling and estimation of multispectral image data", *IEEE Trans. Image Proc.*, vol. 4. no. 8, pp. 1109-1119, 1995.
- [223] R. Molina, J. Mateos and A. K. Katsaggelos, "Multichannel image restoration using Compound Gauss-Markov random Fields", in *Proc. Int. Conf. on Acous. Speech Sign. Proc. (ICASSP)*, vol. 1, pp. 141-144, 2000.
- [224] J. Mateos, R. Molina and A. K. Katsaggelos, "Color image restoration using Compound Gauss-Markov random Fields", in *Proc. X Eur. Sign. Proc. Conf. (EUSIPCO'2000)*, vol. III, pp. 1341-1344, 2000.
- [225] R. Molina, J. Mateos and A. K. Katsaggelos, "Bayesian multichannel image restoration using Compound Gauss-Markov random Fields", *IEEE Trans. Image Proc.*, vol. 12, no. 12, pp. 1642-1654, 2003.

- [226] B. C. S. Tom and A. K. Katsaggelos, "Reconstruction of a High Resolution image from multiple-degraded and misregistered Low-Resolution images", in *Proc. SPIE Conf. Visual Comm. And Image Proc.*, vol. 2308, pp. 971-981, 1994.
- [227] B. C. S. Tom and A. K. Katsaggelos, "Reconstruction of a High resolution image by simultaneous registration, restoration and interpolation of Low-Resolution images", in *Proc. IEEE Int. Conf.. Image Proc. (ICIP)*, vol. 2, pp. 539-542, 1995.
- [228] S. C. Park, M. K. Park and M. G. Kang, "Super-Resolution image reconstruction: A technical overview", *IEEE Sign. Proc. Mag.*, vol. 20, no. 3, pp. 21-36, May 2003.
- [229] G.P. Asner, "Cloud cover in Landsat observations in Brazilian Amazon", *International Journal of Remote Sensing*, vol. 22, pp. 3855-3862, 2001.
- [230] D.G. Leckie, "Advances in remote sensing technologies for forest surveys and management", *Can. J. For. Res.*, vol. 20, pp. 464-483, 1990.
- [231] J. D. Tarpley S. R. Schneider and R. L. Money, "Global vegetation indices from NOAA-7 meteorological satellite", *J. Climate Appl. Meteorol.*, vol. 23, pp. 491-494, 1984.
- [232] S. R. Yhann and J. J. Simpson, "Application of neural networks to AVHRR cloud segmentation", *IEEE Trans. Geosc. Remote Sens.*, vol. 33, no. 3, pp. 590-604, 1995.
- [233] X. Song, Y. Zhao and Z. Liu, "Cloud detection and analysis of MODIS image", *Proceed. IEEE Int. Geosc. Remote Sens. Symp., (IGARSS apos;04)*, vol. 4, pp. 2764-2767, 2004.
- [234] J. J. Simpson and J. I. Gobat, "Improved cloud detection in GOES scenes over land", *Remote sensing of environment*, vol. 52, n<sup>o</sup>1, pp. 36-54, 1995.
- [235] J-P. Cocquerez and S. Philipp, "Analyse d'images: filtrage et segmentation", *Masson*, Paris, 1995.
- [236] S. Benabdelkader, M. Boulemden and S. Louifi, "Threshold selection by maximizing the between-class variance of a fuzzy 2-partition", *Proceed. 9<sup>th</sup> Intern. Workshop on Syst., Sig. Image Proces. IWSSIP'02*, pp. 282-288, 2002.
- [237] S. Benabdelkader and M. Boulemden, "Recursive algorithm based on fuzzy 2-partition entropy for 2 – level image thresholding", *Pattern Recog.*, vol. 38, no. 8, pp. 1289-1294, 2005.
- [238] K. Kawano and J-I. Kudoh, "Cloud detection method for NOAA AVHRR images by using local area parameters", *Proceed. IEEE Int. Geosc. Remote Sens. Symp., (IGARSS' 01)*, vol. 5, pp. 2155-2157, 2001.
- [239] T. F. Eck and V. L. Kalb, "Cloud-screening for Africa using a geographically and seasonally variable Infrared threshold", *Int. J. Remote Sens.* vol.12, pp. 1205-1221, 1991.
- [240] E. P. McClain, *et al.*, "Multi-channel improvements to satellite-derived global sea surface temperatures", *Adv. Space Res.*, vol. 2, pp. 4347, 1983.
- [241] R. M. Welch, K. S Kuo, S. K. Sengupta, and D. W. Chen, "Cloud field classification based upon high spatial resolution textural feature, I. Gray -level cooccurrence matrix approach", *J. Geophys. Research*, vol. 93, pp. 12663- 12681, 1988.
- [242] Z. Gu and C. Duncan, "Texture and spectral features as an aid to cloud classification," in *Proc. IGARSS'88 Symp.2.*, pp. 1193 – 1194, 1988.
- [243] M. R. Azimi-Sadjadi, M. A. Sliakh, B. Tian, K. E. Eis and D. Reinke, "Neural network-based cloud detection/ classification using textural and spectral features", *Proceed. IEEE Int. Geosc. Remote Sens. Symp., (IGARSS apos;96)*, vol. 2, pp. 1105 - 1107, 1996.
- [244] F. Melgani, "Contextual reconstruction of cloud-contaminated multitemporal multispectral images", *IEEE Trans. Geosci. Remote Sens.*, vol. 44, no. 2, pp. 442-455, 2006.

- [245] B. Holben, "Characteristics of maximum-value composite images from temporal AVHRR data", *Int. J. Remote Sens.*, vol. 7, pp. 1417-1434, 1986.
- [246] L. Zerbe and S. Liew, "Reevaluating the traditional maximum NDVI compositing methodology: The Normalized Difference Blue Index", *IEEE Int. Geosci. Rem. Sens. Symp. (IGARSS)*, vol. 4, pp. 2401-2404, 2004.
- [247] J. Cihlar, D. Manak and M. Dflorio, "Evaluation of compositing algorithms for AVHRR data over land", *IEEE Trans. Geosci. and Remote Sens.*, vol. 32., no. 2, pp. 427-437, 1994.
- [248] D. Stoms, M. Bueno and F. davis, "Viewing geometry of AVHRR images composites derived using multiple criteria", *Photogrammetric Engineering & Remote Sensing*, vol. 63, no. 6, pp. 681-689, 1997.
- [249] J. Townshend, C. Skole, D. justice, J. maligreau, J. Cihlar, P. Teillet, F. sadowski and S. Ruttenberg, "The 1-Km AVHRR global data set: needs of the International Geosphere Biosphere program", *INT. J. Remote Sensing*, vol. 15, no. 7, pp. 3319-3332, 1992.
- [250] L. Lei and Yokoyama, "An algorithm of extracting optimal pixels for AVHRR 10-day composite image data of Asian region", *IEEE Int. Geosci. Rem. Sens. Symp. (IGARSS)*, vol. 5, pp. 2334-2336, 2001.
- [251] B. Choudhury and C. Tucker, "Satellite observed seasonal and interannual variation of vegetation over the Kalhari, the great Victoria desert, and the great sandy desert: 1979-1984", *Remote Sensing Environment*, vol. 23, pp. 233-241, 1987.
- [252] D. G. long, Q. Remund and D. Daum, "A cloud removal algorithm for SSM/I data", *IEEE Trans. Geosci. and Remote Sens.*, vol. 37., no. 1, pp. 54-62, 1999.
- [253] P. Hardin and M. Jackson, "Testing single band cloud removal algorithms for SSM/I: An equatorial simulation approach", *IEEE Int. Geosci. Rem. Sens. Symp. (IGARSS)*, vol. 5, pp. 2161-2163, 2000
- [254] R. rossi, J. Dungan and L. Beck, "Kringing in the shadows: Geostatistical intepolation for remote sensing", *Remote Sensing Environment*, vol. 49, no. 1, pp. 32-40, 1994..
- [255] Y. Zhang, B. Guindon and J. Cihlar, "An image transform to characterize and compensate for spatial variations in thin cloud contamination of Landsat images", *Remote Sensing Environment*, vol. 82, no. 2, pp. 173-187, 2002.
- [256] B. Gao, P. Yang, W. Han, R. Li and W. J. Wiscombe, "An algorithm using visible and 1.38- $\mu$ m channels to retrieve cirrus cloud reflectances from aircraft and satellite data", *IEEE Trans. Geosci. and Remote Sens.*, vol. 40., no. 8, pp. 1659-1668, 2002.
- [257] C. Feng, J. Ma, Q. Dai and X. Chen, "An improved method for cloud removal in ASTER data change detction", *IEEE Int. Geosci. Rem. Sens. Symp. (IGARSS)*, vol. 5, pp. 3387-3389, 2004.
- [258] Z. Zhongming and Z. Chongguang, "Approach to removing cloud cover from satellite imagery", *Remote Sensing Environment, China*, vol. 11, no. 3, pp. 195-199, 1996.
- [259] E. G. Moody, M. D. King, S. Platnick, C. B. Schaaf and F. Gao, "Spatially complete global spectral surface albedos: Value-added datasets derived from Terra MODIS land products", *IEEE Trans. Geosci. and Remote Sens.*, vol. 43., no. 1, pp. 144-158, 2005.
- [260] E. H. helmer and B. Ruefenacht, "Cloud-free satellite image mosaics with regression trees and histogram matching", *Photogrammetric Engineering & Remote Sensing*, vol. 71, no. 9, pp. 1079-1089, 2005.
- [261] S. G. Narasimhan and S. K. Nayar, "Contrast restoration of weather degraded images", *IEEE Trans. Patt. Analys. And Mach. Intell.*, vol.25, no. 6, pp. 713-724, 2003.
- [262] S. G. Narasimhan and S. K. Nayar, "Vision and the atmosphere", *Intern. Journal of Cmput. Vison*, 48 (3), pp. 233-254, 2002.

- [263] A. Smola and B. Schölkopf, "A tutorial on support vector regression," Roy. Holloway College, Univ. London, London, U.K., NeuroCOLT Tech. Rep. NC-TR-98-030, 1998.
- [264] N. Cristianini and J. Shawe-Taylor, "An introduction to Support Vector Machine and other Kernel-based learning methods", *1 st ed.*, Cambridge, U.K: Cambridge Univ. Press, 2000.
- [265] F. Melgani and S. B. Serpico, "A Markov Random Field approach to spatio-temporal contextual image classification", *IEEE Trans. Geosci. Remote Sens.*, vol. 41, pp. 2478-2487, 2003.
- [266] F. Melgani and Y. Bazi, "Markovian fusion approach to robust unsupervised change detection in remotely sensed imagery", *IEEE Geosci. Remote Sens. Letters*, vol. 3, pp. 457-461, 2006.
- [267] M. Datcu, K. Seidel and M. Walessa, "Spatial retrieval from remote-sensing images \_ Part II: Gibbs-Markov Random Fields", *IEEE Trans. Geosci. Remo. Sens.*, vol. 36, no. 5, pp. 1446-1455, Sept. 1998.
- [268] R. Duda, P. Hart and D. Stork, "Pattern classification", *2<sup>nd</sup> ed.*, N.Y: Wiley, 2001.
- [269] J. Mercer, "Functions of positive and negative type and their connection with the theory of integral equations", *Philosophical Trans. Royal Socie.*, London A 209, pp. 415-446, 1909.
- [270] V. Vapnik, "The nature of statistical learning theory", *Springer*, New York, 1995.
- [271] F. Melgani and L. Bruzzone, "A residual-based technique for the estimation of biophysical parameters from remote-sensing images", *IEEE Int. Geosci. Rem. Sens. Symp. (IGARSS)*, vol. 1, pp. 476 – 478, 2003.
- [272] F. Melgani and L. Bruzzone, "Estimation of biophysical parameters from optical remote-sensing images with high-order residues", *IEEE Int. Geosci. Rem. Sens. Symp. (IGARSS)*, vol. 2, pp. 1479 - 1482, 2004.
- [273] L. Bruzzone, L. Carlin and F. Melgani, "A residual-based approach to classification of remote-sensing images", *IEEE Workshop on Advances in Techn. for Analysis of Rem. Sens. Data*, pp. 417 - 423, Oct. 2003.
- [274] S. Benabdelkader, F. Melgani and M. Boulemden, "Cloud-contaminated image reconstruction with contextual spatio-spectral information", *Proceed. IEEE Int. Geosci. Remote Sens. Sympos., (IGARSS'07)*, pp. 373-376, 2007.
- [275] S. Benabdelkader and F. Melgani, "Contextual spatio-spectral post-reconstruction of cloud- contaminated images", *IEEE Geosc. Rem. Sens. Letters (GRSL)*, vol. 5, no. 2, pp. 204-208, 2008.
- [276] G. R. Cross and A. K. Jain, "Markov Random Field texture models", *IEEE Trans. Pattern Anal. Machine Intell.*, vol. 5, pp. 25-39, 1983.
- [277] L. Yin, R. Yang, M. Gabbouj and Y. Neuvo, "Weighted median filters: a tutorial", *IEEE Trans. Circuits and Syst. II: Analog and Digital Sig. Proc.*, vol. 43, no. 3, pp. 157-192, 1996.
- [278] E. L. Hall, "Computer Image Processing and Recognition", *Academic Press. Inc.*, 1979.
- [279] Traitement d'image – Amélioration d'image. PYC-ENSERG.
- [280] S. D. Chen and R. Ramli, , "Minimum mean brightness error-bi-histogram equalization in contrast enhancement", *IEEE Trans. Consumer Elect.*, vol. 49, no. 4, pp. 1310-1319, 2003.
- [281] M. Eramian and M. Mould, "Histogram equalization using neighbourhood metrics", *Proceed.. 2nd Canadian Conf. Comput. Robot Vision*, pp. 397 – 404. 2005.
- [282] T. K. Kim, J. K. Paik and B. S. Kang, , "Contrast enhancement system using spatially adaptive histogram equalization with temporal filtering", *IEEE Trans. Consumer Elect.*, vol. 44, no. 1, pp. 82-86, 1998.

- [283] J. Y. Kim, L. S. Kim and S. H. Hwang, , “An advanced contrast enhancement using partially overlapped sub-block histogram equalization”, *IEEE Trans. Circ. Syst. For Video Tech.*, vol. 11, no. 4, pp. 475-484, 2001.
- [284] V. Caselles, J. L. Lisani, J. M. Morel and G. Sapiro, "Shape preserving local contrast enhancement", *Proceed. Int. Conf. Image Proc.*, vol. 1, pp. 314-317, 1997.
- [285] Y. T. Kim, “Contrast enhancement using brightness preserving bi-histogram equalization”, *IEEE Trans. Consumer Elect.*, vol. 43, no. 1, pp. 1-8, 1997.
- [286] Y. Wan, Q. Chen and B. M. Zhang, “Image enhancement based on equal area dualistic sub-image histogram equalization method”, *IEEE Trans. Consumer Elect.*, vol. 45, no. 1, pp. 68-75, 1999.
- [287] S. D. Chen and R. Ramli,, “Contrast enhancement using recursive mean separate histogram equalization for scalable brightness preservation”, *IEEE Trans. Consumer Elect.*, vol. 49, no. 4, pp. 1301-1309, 2003.
- [288] C. Wang and Z. Ye, “Brightness preserving histogram equalization with maximum entropy: A variational perspective”, *IEEE Trans. Consumer Elect.*, vol. 51, no. 4, pp. 1326-1334, 2005.
- [289] T. K. Yeong, “Quantized bi-histogram equalization”, *IEEE Int. Conf. Acoust., Speech, Sig. Proc., ICASSP-97.*, vol. 4, pp. 2797-2800, 1997.
- [290] J. Chanussot, B. Vigouroux and J. Chabod, "Lossless compact histogram representation for multi-component images: application to histogram equalization", ", *Proceed. IEEE Int. Geosci. Remote Sens. Sympos., (IGARSS'03)*, vol. 6, pp. 3940-3942, 2003.
- [291] P. A. Misna and J. J. Rodriguez, "A multivariate contrast enhancement technique for multispectral images", *IEEE Trans. Geosc. Rem. Sens.*, vol. 33, no. 1, pp. 212-216, 1995.
- [292] P. A. Misna, Q. Zhang and J. J. Rodriguez, "3-D histogram modification of color images", *Proceed. Int. Conf. Image Proc.*, vol. 3, pp. 1015-1018, 1996.
- [293] I. Pitas and P. Kiniklis, "Multichannel techniques in color image enhancement and modeling", *IEEE Trans. Image Proc.*, vol. 5, no. 1, pp. 168-171, 1996.
- [294] E. Pichon, M. Niethammer and G. Sapiro, "Color histogram equalization through mesh deformation", *Proceed. Int. Conf. Image Proc., ICIP*, vol. 2, pp. II - 117-20, 2003.
- [295] K. Huang, Q. Wang and Z. Wu, "Color image enhancement and evaluation algorithm based on human visual system", *IEEE Int. Conf. Acoust., Speech, Sig. Proc., ICASSP'04*, vol. 3, pp. iii-721-4, 2004.
- [296] T-C. Jen, B. Hsieh and S-J Wang, "Image contrast enhancement based on intensity-pair distribution", *Proceed. Int. Conf. Image Proc., ICIP*, vol. 1, pp. I - 913-16, 2005.
- [297] M. Zhao, "Image Thresholding Technique Based On Fuzzy Partition And Entropy Maximization", Ph. D thesis, School of Electrical And Information Engineering, University of Sydney, Dec., 2004.
- [298] H.-D. Cheng, J.-K. Chen and J. Li, "Threshold selection based on fuzzy c-partition entropy approach", *Pattern Recog.*, (1), pp. 857-870, 1998.
- [299] N. Otsu, "A threshold selection method from grey level histogram", *IEEE Trans. Syst. Man Cyber.*, vol. 9, no. 1, p. 62, 1979.